BUDKER INSTITUTE OF NUCLEAR PHYSICS

Super Charm Tau Factory

PRELIMINARY DESIGN REPORT

Novosibirsk – 2010

Contents

Chapter 1

Physical program for Super $\mathcal{CT}$ factory

1.1 Introduction

A Super $c\tau$ factory is an electron-positron collider operating in the range of center-of-mass (c.m.) energies from 2 to $5 \div 6\,\mathrm{GeV}$ with a high luminosity of about $10^{35}\,\mathrm{cm}^{-2}\mathrm{s}^{-1}$. In this energy range practically all states with charm can be produced including charmonium-mesons, which are bound states of c and $\bar{c}$ quarks, charmed mesons comprising one c ($\bar{c}$) quark, and charmed baryons comprising one c quark. In addition, at the c.m. energy above $2m_\tau \approx 3.6\,\mathrm{GeV}$ τ-lepton pairs can be produced. Because of its extremely high luminosity such a collider will be a copious source of charmed particles and τ leptons. This brings us to the name Super $c\tau$ factory (CTF).

The main goal of experiments at CTF is a study of the processes with c quarks or τ leptons in the final state using data samples that are 3-4 orders of magnitude higher than collected today at CLEOc and BESII detectors. To understand opportunities provided by CTF we show in Table 1.1 a possible distribution of an integrated luminosity of 1 ab^{-1} in different energy ranges. At CTF with a luminosity of $10^{35}\,\mathrm{cm}^{-2}\mathrm{s}^{-1}$ such an integrated luminosity can be collected during half a year producing thereby 10^9 τ leptons, 10^9 D mesons and a fantastic number (10^{12}) of J/ψ mesons. These statistics will allow a systematic study of all states of quarks of the two first generations ($u,\ d,\ s$ and c) as well as searches for states of exotic nature.

A theory of strong interactions, quantum chromodynamics (QCD), in addition to standard mesons and baryons consisting of 2 and 3 quarks, respectively, cannot rule out the existence of four- and five-quark states as well as bound states of gluons, carriers of strong interactions [1]. Such states are possible because gluons, in contrast to a photon, an electrically neutral carrier of electromagnetic interactions, possess a strong or color charge. QCD predicts both hybrid quark-gluon states and states consisting of gluons only, glueballs. Hybrids and glueballs are a completely new form of matter that can be formed by strong interactions only. One of the tasks of CTF is to discover exotic states and study their properties.

Huge data samples of D mesons and τ leptons will allow a study of principally new phenomena, such as CP violation in the D meson system and in τ leptons as well as lepton flavor violation.

Table 1.1: *Possible distribution of an integrated luminosity collected at CTF (1 ab^{-1}) in different energy ranges.*

E, GeV	3.097	3.686	3.770	3.800–5.000
L, fb^{-1}	300	150	350	200

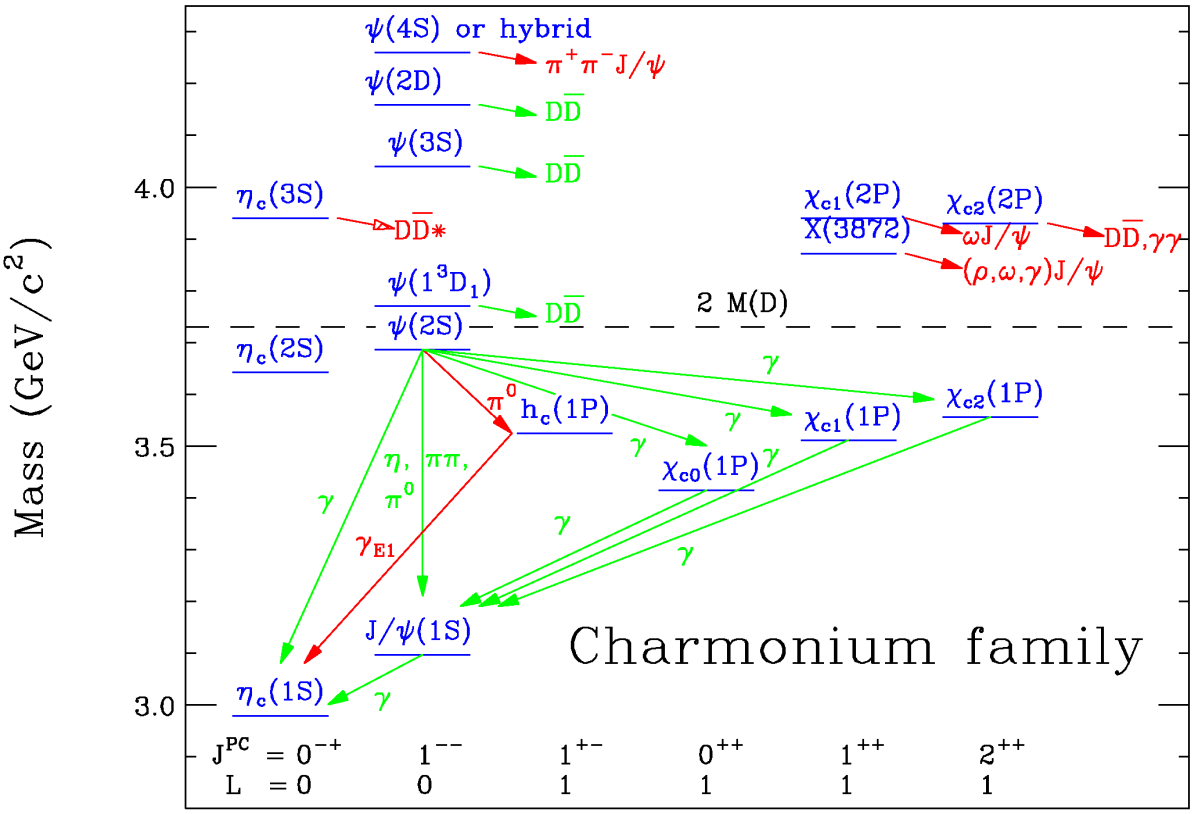

Figure 1.1: *Charmonium system and transitions. Red (dark) arrows indicate recently discovered decays and transitions between the levels. The dashed line shows a production threshold for a pair of charmed mesons.*

A physics program for CTF can be subdivided into the following subsections, which are discussed in more detail below:

1. charmonium,
2. spectroscopy of states of light quarks,
3. physics of D mesons,
4. physics of charmed baryons,
5. τ lepton physics,
6. measurement of the cross section of $e^+e^- \to$ hadrons,
7. two-photon physics.

1.2 Charmonium

A scheme of charmonium levels is shown in Fig. 1.1. All states lying below the threshold of D meson production and therefore decaying into hadrons consisting of the light u, d and s quarks (or into a lower mass charmonium) have been discovered. Vector mesons ($J^{PC} = 1^{--}$), i.e., J/ψ,

Table 1.2: *The number of $c\bar{c}$ mesons that can be produced at CTF with an integrated luminosity of 1 ab^{-1}. Estimates of physical cross sections are based on Refs. [2, 3, 4].*

	J/ψ	$\psi(2S)$	$\psi(3770)$	$\psi(4040)$	$\psi(4160)$	$\psi(4415)$
M, GeV	3.097	3.686	3.773	4.039	4.153	4.421
Γ, MeV	0.093	0.304	27	80	103	62
σ, nb	$\sim$3400	$\sim$640	$\sim$6	$\sim$10	$\sim$6	$\sim$4
L, fb^{-1}	300	150	350	10	20	25
N	10^{12}	10^{11}	2×10^9	10^8	10^8	10^8

$\psi(2S)$, $\psi(3770)$, etc. are directly produced in e^+e^- collisions. In Table 1.2 we list the numbers of 1^{--} mesons that can be produced at CTF with an integrated luminosity of 1 ab^{-1}. Estimates take into account the expected beam energy spread.

In radiative decays of J/ψ and $\psi(2S)$ mesons [2] about 10^{10} χ_{cJ} and η_c mesons each can be obtained. About 10^8 h_c mesons can be produced in the $\psi(2S)\to h_c\pi^0$ decay, which has a branching fraction of about 10^{-3} [5]. For observing $\eta_c(2S)$ one can use a rare, not yet discovered radiative transition $\psi(2S)\to\eta_c(2S)\gamma$ (its branching fraction is expected to be 5×10^{-4} [1]) or two-photon production (see Sec. 1.8). Such a data sample allows a systematic study of $c\bar{c}$-meson properties. The following items should be mentioned:

1. Precision measurement of probabilities for transitions between low-lying levels of charmonium, their masses, total and leptonic or two-photon widths. These parameters are calculated in potential quark models and can also be obtained within lattice QCD. In close future the accuracy of lattice calculations will reach a level of about 1% or better. At CTF one will be able to measure probabilities of rare, not yet discovered electric $\eta_c(2S)\to h_c\gamma$ (2.5×10^{-3}), $\psi(3770)\to\chi_{c0}\gamma$ (2×10^{-4}) and magnetic $\psi(2S)\to\eta_c(2S)\gamma$ (5×10^{-4}), $\eta_c(2S)\to J/\psi\gamma$ (3×10^{-5}), $h_c\to\chi_{c0}\gamma$ ($\sim10^{-6}$) dipole transitions. Shown in parentheses are transition probabilities expected in the quark model [1]. From the analysis of angular distributions of photons in the $\chi_{cJ}\to J/\psi\gamma$ and $\psi(2S)\to\chi_{cJ}\gamma$ decays one can extract the amplitudes of $M2$ and $E3$ transitions interfering with the dominating $E1$ transition and determine an admixture of the D wave state in $\psi(2S)$ (see a review in [6] and references therein).

2. Information about decays of low-lying states of charmonium is very incomplete. For the best-studied J/ψ meson about 40% of hadronic decays only have been measured. For other states the situation is even worse. One of the tasks for CTF is a systematic study of all low-lying charmonium states. This program, in particular, includes a precision measurement of hadronic transitions between charmonium states with emission of one or two π mesons, η meson, $\psi, h_c\to3\gamma$ decays, a photon spectrum in the reaction $\psi\to\gamma X$, where X is a hadronic state of light quarks, and direct measurement of the probabilities of $\eta_c,\chi_{c0},\chi_{c1}\to2\gamma$ decays.

3. During recent years considerable progress has been achieved in studies of states above the threshold of D meson production. New states $X(3872)$, $Z(3930)$, $X(3940)$, $Y(3940)$, $Y(4260)$ have been discovered (see reviews [6, 7] and references therein). There is serious evidence for three more resonances: $Y(4360)$ [8], $Y(4660)$ [9], and $Z^+(4430)$ [10]. Note that a charged charmonium state $Z^+(4430)$ obviously does not fit the two-quark model. Four new states

with mass below 4 GeV have a positive C-parity and can be associated with excited $c\bar{c}$ mesons, $\eta_c(3S)$ and $\chi_{cJ}(2P)$, although some properties of the $X(3872)$ meson can hardly be explained within the two-quark assumption. At CTF, for identification and study of $\chi_{cJ}(2P)$ mesons one can use decays $\psi(4040)$, $\psi(4160)$, $\psi(4415) \to \chi_{cJ}(2P)\gamma$. To this end, considerable statistics should be accumulated at the $\psi(4040)$, $\psi(4160)$ and $\psi(4415)$ resonances (see Table 1.2). Probabilities of electric dipole transitions $\psi \to \chi_{cJ}(2P)\gamma$ are predicted at the 10^{-3} level [11].

The $Y(4260)$, $Y(4360)$, $Y(4660)$ states have quantum numbers 1^{--} and can be directly produced in e^+e^- collisions. Typical cross sections of their production are about 50 pb. For their detailed study a scan of the energy range 3.8 to 5.0 GeV with an integrated luminosity of about 100 fb^{-1} is needed. Such a program can be realized at CTF only.

4. A relatively small width of the J/ψ resonance and a huge data sample provided by CTF allow an observation of weak J/ψ decays. The total probability of weak decays of J/ψ via a $c \to sW^+$ transition is (2–4)$\times 10^{-8}$ [12]. Semileptonic $J/\psi \to D_s^* l\nu$, $D_s l\nu$ and hadronic $J/\psi \to D_s^+\rho^-$, $D_s^{*+}\pi^-$ modes have branching fractions of (3–4)$\cdot 10^{-9}$ [12, 13] and can be measured at CTF. In Standard Model (SM) decays with $\Delta S = 0$ are suppressed. For example, the branching fractions of $J/\psi \to D^0\rho^0$ and $J/\psi \to D^0\pi^0$ decays are predicted at the level of 2×10^{-11} and 0.6×10^{-11} [13], respectively. This makes such decays sensitive to effects of new physics not described by SM, in particular, to the existence of a flavor-changing neutral current (a $c \to u$ transition) [14].

   Another type of weak processes ($c\bar{c} \to s\bar{s}$ with W boson exchange) results in decays violating C parity, such as, e.g., $J/\psi \to \phi\phi$. The expected branching fraction of this decay is sufficiently high ($\sim 10^{-8}$ [15]) for its observation at CTF.

5. A large sample of ψ meson decays allows a search for phenomena not described by SM, such as violation of CP parity and lepton flavor conservation. Lepton flavor violation can be observed in $J/\psi \to l\bar{l}'$ decays, where $l, l' = e, \mu, \tau$. Branching fractions of such decays can be related in a model-independent way to branching fractions of μ and τ decays to three leptons [16]. From the limits $B(\mu \to ee^+e^-) < 10^{-12}$ [2] and $B(\tau \to \mu e^+e^-) < 2.7 \times 10^{-8}$ [17] one obtains $B(J/\psi \to \mu e) < 2 \times 10^{-13}$ and $B(J/\psi \to \tau l) < 6 \times 10^{-9}$. A limit on the decay $\tau \to \mu e^+e^-$ has been set with a data sample of 5×10^8 τ lepton pairs. Thus at CTF J/ψ decays can be more sensitive to lepton flavor violation than those of τ leptons.

One of physical effects beyond SM is the existence of the non-zero electric dipole moment (EDM) of quarks or leptons leading, in particular, to CP violation. J/ψ decays provide the best opportunity to obtain information about the c-quark EDM. To search for CP violation one can use three-body decays, e.g., $J/\psi \to \gamma\phi\phi$. In this case, one can compose a CP odd combination of momenta of final particles and an initial electron and determine a parameter describing CP asymmetry which is proportional to EDM. With 10^{12} J/ψ mesons, using the $J/\psi \to \gamma\phi\phi$ decay one can obtain a sensitivity to the c-quark EDM at the 10^{-15} $e\cdot$cm level [18]. A two-body $J/\psi \to \Lambda\bar{\Lambda}$ decay, in which polarizations of final baryons can be measured from the $\Lambda \to p\pi^-$ decay, can be also used for a search for CP violation. With 10^{12} J/ψ mesons, this decay can be used to set a limit on the Λ-hyperon EDM at the 5×10^{-19} e$\cdot$cm level [19], two orders of magnitude more stringent than the existing limit.

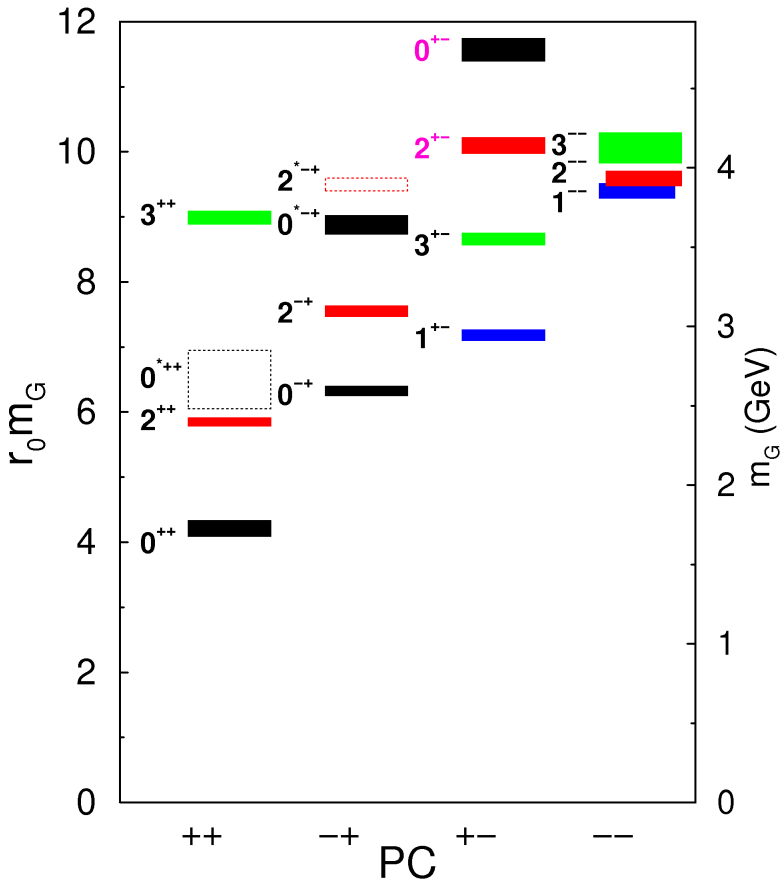

Figure 1.2: *Spectrum of glueball masses [20].*

1.3 Spectroscopy of states of light quarks

Charmonium states with a mass smaller than two D-meson masses decay into hadrons consisting of light u, d and s quarks. Selecting special decay modes of $c\bar{c}$ mesons one can select and study states with practically any quantum numbers. Therefore, CTF is a unique laboratory to study properties of mesons consisting of u, d, and s quarks with mass lighter than 3 GeV.

Of special interest is a search for bound states of two gluons, glueballs, and hybrid states, $q\bar{q}g$. With a $\sim 9\%$ probability the J/ψ meson decays into γgg followed by hadronization of two gluons. Thus, the J/ψ radiative decays are the best sources of glueball production. Lattice QCD calculations [20, 21] predict that the lightest glueballs with the quantum numbers $J^{PC} = 0^{++}$, 2^{++}, and 0^{-+} have masses smaller than 3 GeV. The glueball spectrum obtained in Ref. [20] is shown in Fig. 1.2.

One of the characteristic features allowing to distinguish a glueball from a regular two-quark meson is anomalously small two-photon width. Therefore, a search for glueballs in J/ψ decays should be complemented by a study of two-photon meson production. (see section 1.8). Previous searches for glueballs failed to give an unambiguous result. Most probably, glueballs are mixed with two-quark mesons. To determine a glueball fraction in a meson, one should study in detail meson properties in different processes and decay modes. For example, for a family of scalars (f_0, a_0, K_0^*), one should measure with high precision the processes $J/\psi \to f_0\gamma$, $f_0\phi$, $f_0\omega$, $a_0\rho$, $K^*(892)K_0^*$, and $\gamma\gamma \to f_0$, a_0 in different scalar decay modes $f_0, a_0, K_0^* \to PP$, VP, VV, $V\gamma$, where V and P

Table 1.3: *The maximum values of the $e^+e^- \to D\bar{D}^{(*)}$ and $e^+e^- \to D_s\bar{D}_s^{(*)}$ cross sections [22, 23] and the energies where the cross sections are maximal.*

	D^+D^-	$D^0\bar{D}^0$	$D\bar{D}^*$	$D_s^+D_s^-$	$D_s^+D_s^{*-}$
E, GeV	3.77	3.77	4.02	4.01	4.17
σ, nb	2.9	3.7	$\sim$6.7	$\sim$0.25	$\sim$0.9

are vector and pseudoscalar mesons, respectively. A gluon component will reveal itself as a ratio of decay probabilities unusual for two-quark mesons and appearance of an extra f_0 meson not fitting the scheme of two-quark states. It is worth noting that in addition to gluonic and two-quark states, QCD predicts existence of exotic four-quark mesons and molecular states of two mesons. Existence of such states and their mixing with two-quark states makes even more complicated the pattern of levels of scalar mesons. Detailed systematization of mesons requires very large data samples of J/ψ decays and two-photon events that can be accumulated at CTF only.

A search for hybrid states is facilitated by the fact that such a state with a smallest mass of 1.3–2.2 GeV/c^2 should have exotic quantum numbers $J^{PC} = 1^{-+}$, impossible in the quark model (see review [7] and references therein). At the present time there are two candidates for the light-quark hybrid: $\pi_1(1400)$ and $\pi_1(1600)$. Properties of these states are badly investigated and even their existence should be confirmed. The π_1 states were observed primarily in diffractive experiments $\pi^-N \to \pi_1^-N$. CTF allows a study of completely different production mechanisms: S-wave decay $\chi_{c1} \to \pi\pi_1$ and P-wave decay $J/\psi \to \rho\pi_1$. One should study main decay modes expected for a hybrid: $\rho\pi$, $b_1\pi$, $f_1\pi$, $\eta\pi$, $\eta'\pi$. It is expected that the lightest state of a hybrid with non-exotic quantum numbers 0^{-+} is also in the mass region around 2 GeV. This state can be searched for in the decay $\chi_{c0} \to \pi\pi_1$ as well as in ψ meson decays.

1.4 Physics of D-mesons

In Table 1.3 the values of the D-meson production cross sections are listed. With the luminosity distribution given in Table 1.1, about 10^9 pairs of charged and neutral D mesons, and about 2×10^7 pairs of D_s mesons can be produced at CTF.

These numbers do not exceed the numbers of D mesons produced at existing B-factories at the e^+e^- c.m. energy of 10.58 GeV. There are, however, crucial differences between D-meson events at 10.58 and 3.77 GeV, which make low energy measurements preferable and allow to obtain more precise results with lower statistics:

- The multiplicity of charged and neutral particles is about two times lower at $\psi(3770)$ than at $\Upsilon(4S)$.
- In contrast to $\Upsilon(4S)$, where D meson production is accompanied by many other particles, at the threshold pure $D\bar{D}$ events are produced. This allows to use additional kinematic constraints for the event reconstruction. In particular, in events with leptonic or semileptonic decay of one of the D mesons, the neutrino is reconstructed with the additional constraint of zero missing mass. Use of the double-tag method, when one of the D mesons is fully

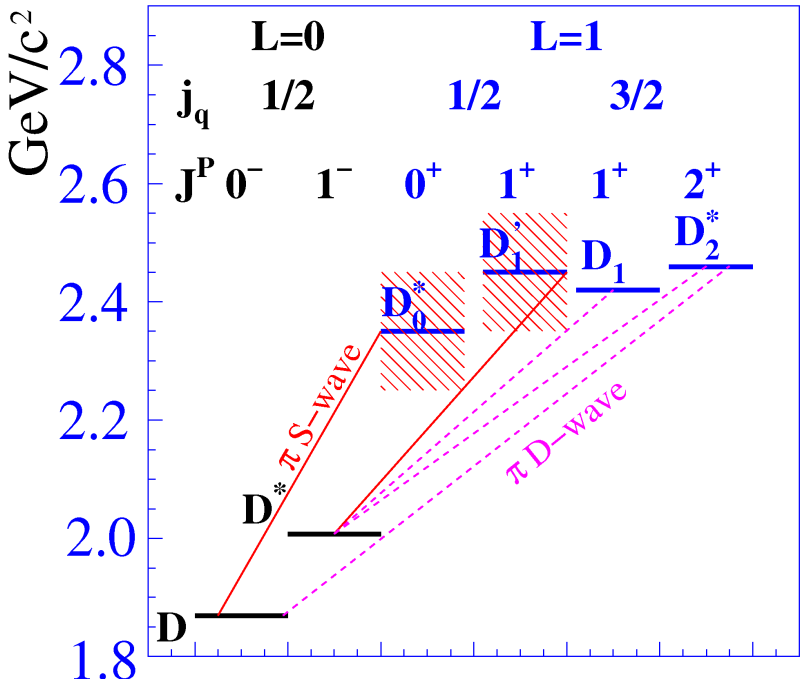

Figure 1.3: *The D-meson states and transitions between them.*

reconstructed, while the other is studied, strongly reduces background and allows to perform precise measurements of absolute decay probabilities.

- D and $\bar{D}$ mesons are produced in a quantum-coherent state, for example, with $J^{PC} = 1^{--}$ in the reaction $e^+e^- \to D\bar{D}$ or $J^{PC} = 0^{++}$ in the reaction $e^+e^- \to D\bar{D}\gamma$. The coherence allows to use simple techniques for a study of $D\bar{D}$ mixing, search for CP violation, measurement of strong phases, and probabilities of decays to CP states.

At CTF a systematic study of D-meson properties will be performed.

1.4.1 Spectroscopy of D mesons

There are three types of charmed mesons: charged $D^{\pm}$ mesons with the quark structure $(c\bar{d})$ or $(\bar{c}d)$, neutral D^0 and $\bar{D}^0$ mesons with the structure $(c\bar{u})$ or $(\bar{c}u)$, and $D_s^{\pm}$ mesons with the structure $(c\bar{s})$ or $(\bar{c}s)$. The classification if D-meson excited states is demonstrated in Fig. 1.3. From the six states shown, the two lowest have $L = 0$, while the four others have $L = 1$. For the heavy-light quark system, in the heavy-quark limit, the total angular momentum (j_q) of the light quark is a conserved quantum number. This leads to decomposition of the P-wave states (D_J) into two multiplets with $j_q = 1/2$ and $j_q = 3/2$. The D_J states transit into the D and D^* states with π-meson emission. Mesons with $j_q = 3/2$ decay in the D-wave and are therefore relatively narrow. Such a classification is applicable to all three types of D mesons. The known low-lying states of D and D_s mesons [2] are listed in Table 1.4. Experimental information about the D_J and D_{sJ} mesons is not complete. The quantum numbers for most of them are not established. Almost no information exists about their decay modes. Moreover, the masses of the D_{sJ} mesons lie well below the predictions of the quark model [24]. To explain this discrepancy, the hypotheses, for example, of six-quark or molecular D_{sJ} structure are suggested. At CTF D_J and D_{sJ} mesons can be produced in the reactions $e^+e^- \to D_0^*\bar{D}^*$, $D_1^{(\prime)}\bar{D}^{(*)}$, $D_2^*\bar{D}^{(*)}$, which have thresholds in the energy range of 4.3–4.7 GeV. The cross sections of these reactions are about 1 nb [25, 26]. So,

Table 1.4: *The parameters of D and D_s mesons. The masses and widths are given in* MeV.

Charge		D	D^*	D_0^*	D_1'	D_1	D_2^*
$\pm$	M	1869.60 ± 0.16	2010.25 ± 0.14	2403 ± 38		2423.4 ± 3.1	$2460.1^{+2.6}_{-3.5}$
	Γ	1040 ± 7 fs	0.096 ± 0.022	283 ± 40		25 ± 6	37 ± 6
0	M	1864.83 ± 0.14	2006.96 ± 0.16	2318 ± 29	2427 ± 36	2422.0 ± 0.6	$2462.8 \pm 1.$
	Γ	410.1 ± 1.5 fs	< 2.1	267 ± 40	384^{+130}_{-105}	20.4 ± 1.7	42.9 ± 3.1
Charge		D_s	D_s^*	D_{s0}^*	D_{s1}'	D_{s1}	D_{s2}^*
$\pm$	M	1968.47 ± 0.33	2112.3 ± 0.5	2317.8 ± 0.6	2459.5 ± 0.6	2535.29 ± 0.20	2572.6 ± 0.9
	Γ	500 ± 7 fs	< 1.9	< 3.8	< 3.5	< 2.3	20 ± 5

the integrated luminosity of about 50 fb^{-1}, collected in the 4.3–5.0 GeV energy range, will be sufficient to perform a careful study of D_J and D_{sJ} properties. Detailed measurement of exclusive charm-production cross sections up to the 5–6 GeV will allow to observe production of the known higher excited states, $D_{sJ}(2632)$ [27], $D_{sJ}(2708)$ [28], and $D_{sJ}(2860)$ [29], and find new states of this family.

1.4.2 Charmed-meson decays

Charmed-meson decays are a unique source for studying the dynamics of strong interactions. CTF allows to perform a detailed study of D and D_s decays including high precision measurements of decay probabilities, Dalitz plot analyses for three-body decays, and analyses of four-body decay distributions. It is expected that in close future many parameters extracted from D and D_s decays, such as the decay constants, f_D and f_{D_s}, and form factors of semileptonic decays, will be calculated with high accuracy in the framework of the lattice QCD (LQCD). Precision measurements of D decays will allow to control these calculations and extrapolate them to the B-meson region. As a result, a significant decrease of the theoretical uncertainties in extracting the CKM matrix elements V_{cd}, V_{cs}, V_{td}, V_{ts}, V_{ub} and V_{cb} from the precision measurements of various B meson decays is expected. For a precise measurement of the angle γ (ϕ_3) of the unitarity triangle at a super-B factory, neutral D-meson data are required, such as $D^0 - \bar{D}^0$ mixing parameters, the ratio of the amplitudes for D^0 and $\bar{D}^0$ decays into $K^+\pi^-$, the strong phase difference between these amplitudes, Dalitz distributions for the three-body hadronic decays, for example, into the $K_S\pi^+\pi^-$ final state [30]. All these data can be obtained at CTF. Below, the current status of leptonic and semileptonic D decays and CTF possibilities for their measurements are discussed in more detail.

In SM the width of a leptonic D decay is given by

$$\Gamma(D^+ \to l^+\nu) = \frac{G_F^2}{8\pi} f_D^2 m_l^2 M_D \left(1 - \frac{m_l^2}{M_D^2}\right)^2 |V_{cd}|^2.$$

A similar formula with the substitution of V_{cs} for V_{cd} is used for a D_s leptonic decay. The data on leptonic decays of the D and D_s mesons obtained by the CLEO Collaboration [31, 32] are listed in Table 1.5. The probabilities of the decays $D^+(D_s^+) \to e^+\nu$ are expected to be about $10^{-8}(10^{-7})$ and can hardly be measured even at CTF. The expected branching fraction for the $D^+ \to \tau^+\nu$ (about 1.2×10^{-3}) is at the level of the CLEO upper limit.

Table 1.5: *The data on leptonic decays of the D and D_s mesons obtained by the CLEO Collaboration.*

	D^+	D_s^+
$e^+\nu_e$	$< 8.8 \times 10^{-6}$ [31]	$< 1.2 \times 10^{-4}$ [32]
$\mu^+\nu_\mu$	$(3.82 \pm 0.32 \pm 0.09) \times 10^{-4}$ [31]	$(5.65 \pm 0.45 \pm 0.17) \times 10^{-3}$ [32]
$\tau^+\nu_\tau$	$< 1.2 \times 10^{-3}$ [31]	$(6.42 \pm 0.81 \pm 0.18) \times 10^{-2}$ [32]

Table 1.6: *The experimental values of the D and D_s decay constants [31, 32] in comparison with the LQCD calculation [34].*

	Experiment	Theory
f_D, MeV	$205.8 \pm 8.5 \pm 2.5$	208 ± 4
f_{D_s}, MeV	$259.5 \pm 6.6 \pm 3.1$	241 ± 3
f_{D_s}/f_D	$1.26 \pm 0.06 \pm 0.02$	1.162 ± 0.009

In SM the unitarity constraints allow to determine the CKM matrix elements V_{cd} and V_{cs} from experimental data with high precision: $|V_{cd}| = 0.2251(8)$, $|V_{cs}| = 0.9735(2)$ [33]. Therefore, the measured leptonic decay branching fractions can be used to extract the decay constants and their ratio. The experimental values of these parameters obtained using CLEO data from Table 1.5 are listed in Table 1.6.

In the second column of Table 1.6 the results of the most accurate-to-date LQCD calculation [34] are listed. It is seen that the claimed accuracy of the theoretical calculations has reached 1–2%. The measured value of f_D agrees with the result of the calculation, whereas the difference between the measurement and the LQCD calculation for f_{D_s} is 2.3 standard deviations. It is obvious that an independent confirmation of the theoretical calculations [34] is required. Since SM relations are used for the extraction of the decay constants, the difference between the experiment and the SM calculation can indicate the presence of contributions beyond the Standard Model (BSM). An additional SM test in this case might be the lepton universality test, i.e., comparison of the D_s decay widths into the $\tau\nu$ and $\mu\nu$ final states. The current experimental value of this ratio 11.4 ± 1.7 [32] is consistent with the theoretical value 9.76.

At CTF the expected statistics of D and D_s mesons are about three orders of magnitude larger than in the CLEO experiment. This will allow to measure the decay constants with an accuracy not worse than 0.5%. The same accuracy will be achieved in the near future in theoretical calculations.

The total branching fractions of the semileptonic D decays measured by CLEO are $B(D^0 \to Xe^+\nu_e) = (6.46 \pm 0.17 \pm 0.13)\%$, $B(D^+ \to Xe^+\nu_e) = (16.13 \pm 0.20 \pm 0.33)\%$ [35]. For D_s the same branching fraction is measured with a poor accuracy and is about 8%. One of the goals of CTF is a high-statistics study of exclusive semileptonic decay modes, including Dalitz plot analyses, and extraction of the form factors describing the hadronization of the primary quarks produced in D decays.

The best studied are semileptonic D decays into π and K mesons. These decays are described

well with a single form factor. For example, the width for the $D \to Ke\nu$ decay is proportional to

$$\frac{d\Gamma(q^2)}{dq^2} \propto |f_+(q^2)|^2 |V_{cs}|^2,$$

where q is the difference of the D and K four-momenta. From measurements, the q^2 dependence of the form factor and the product $f_+(0)|V_{cs}|$ are extracted. The value of the form factor $f_+(0)$ can be calculated theoretically, for example, in the framework of LQCD. The current accuracy of these calculations is about 10%. The theoretical values of the form factors, $f_+^\pi(0) = 0.64(3)(6)$ and $f_+^K(0) = 0.73(3)(7)$ [36], are consistent with experimental values. The most precise measurement of the form factors was performed by the CLEO Collaboration [37]: $f_+^\pi(0) = 0.666(19)(5)$, $f_+^K(0) = 0.739(7)(5)$. To obtain these experimental values, the elements of the CKM matrix satisfying the unitarity condition [2] are used. It is expected that the accuracy of theoretical calculations of the form factors will improve to a 1% level. In this case the semileptonic decays can be used for measurements of V_{cs} and V_{cd} and to test the unitarity relation.

Other semileptonic D and D_s decay modes, excluding $D \to K^*\ell\nu$, are measured with low accuracy. For their detailed study, large statistics are needed which can be collected only at CTF. For example, an integrated luminosity of 100 fb^{-1} is required to measure the $D \to \rho e\nu$ branching fraction with a 0.5% accuracy, and ten times more statistics are needed for the precise measurement of three form factors describing this decay.

1.4.3 D^0–$\bar{D}^0$ Mixing

One of the main goals of the CTF is a study of D^0–$\bar{D}^0$ mixing. The transitions $D^0 \Leftrightarrow \bar{D}^0$ are a result of the interaction which changes the internal quantum number charm by $\Delta C = 2$. Due to these transitions of D mesons, the eigenstates of the mass matrix are the following:

$$|D_1\rangle = \frac{1}{\sqrt{|p|^2 + |q|^2}}(p|D^0\rangle + q|\bar{D}^0\rangle),$$

$$|D_2\rangle = \frac{1}{\sqrt{|p|^2 + |q|^2}}(p|D^0\rangle - q|\bar{D}^0\rangle).$$

In case of the CP-invariant interaction $p = q$ and the eigenstates $|D_1\rangle$ and $|D_2\rangle$ have a definite internal CP-parity. As a rule, two non-dimensional parameters are used for a description of mixing:

$$x \equiv \frac{\Delta m}{\Gamma}, \;\; y \equiv \frac{\Delta\Gamma}{2\Gamma},$$

where Δm and $\Delta\Gamma$ are the differences of masses and widths of the $|D_2\rangle$ and $|D_1\rangle$ states and Γ is the average width of a D^0 meson. In SM the values of these parameters result from long-distance interactions (due to intermediate-meson transitions) and, therefore, predictions for their values have poor precision [38]. It is predicted that x and y can reach the values of ~ 0.01. The most precise data for D-meson mixing were obtained in B-factory experiments. Averaging the current data, which was done by HFAG [39] under the assumption of CP-invariance, gives the following results:

$$x = 0.0100^{+0.0024}_{-0.0026}, \; y = 0.0076^{+0.0017}_{-0.0018}.$$

In CTF experiments, D^0 and $\bar{D}^0$ mesons will be produced in a coherent state with the odd C-parity in the process $e^+e^- \to D^0\bar{D}^0(n\pi^0)$ and the even one in the process $e^+e^- \to D^0\bar{D}^0\gamma(n\pi^0)$. This can be used for a measurement of mixing. In case of a symmetric CTF (the energies of

Table 1.7: *The ratios of decay probabilities of the $D^0\bar{D}^0$ state to various final states. Only leading-order terms in a power series expansion in r_f^2, x and y are given.*

	$C=-1$	$C=+1$
$(1/4)\cdot(\Gamma_{lS_+}\Gamma_{S_-}/\Gamma_{lS_-}\Gamma_{S_+}-\Gamma_{lS_-}\Gamma_{S_+}/\Gamma_{lS_+}\Gamma_{S_-})$	y	$-y$
$(\Gamma_{fl^-}/4\Gamma_f)\cdot(\Gamma_{S_-}/\Gamma_{lS_-}-\Gamma_{S_+}/\Gamma_{lS_+})$	y	$-y$
$(\Gamma_{f\bar{f}}/4\Gamma_f)\cdot(\Gamma_{S_-}/\Gamma_{\bar{f}S_-}-\Gamma_{S_+}/\Gamma_{\bar{f}S_+})$	$y+r_fz_f$	$-(y+r_fz_f)$
$(\Gamma_f\Gamma_{S_+S_-}/4)\cdot(1/\Gamma_{fS_-}\Gamma_{S_+}-1/\Gamma_{fS_+}\Gamma_{S_-})$	$y+r_fz_f$	0
$(\Gamma_{\bar{f}}/2)\cdot(\Gamma_{S_+S_+}/\Gamma_{\bar{f}S_+}\Gamma_{S_+}-\Gamma_{S_-S_-}/\Gamma_{\bar{f}S_-}\Gamma_{S_-})$	0	$y+r_fz_f$
$\Gamma_{ff}/\Gamma_{f\bar{f}}$	R_M	$2r_f^2+r_f(z_fy-w_fx)$
$\Gamma_{fl^+}/\Gamma_{fl^-}$	r_f^2	$r_f^2+r_f(z_fy-w_fx)$
$\Gamma_{l^\pm l^\pm}/\Gamma_{l^+l^-}$	R_M	$3R_M$

colliding electrons and positrons are equal), a study of time evolution of the $D^0\bar{D}^0$ system is not possible due to a small lifetime of the D-mesons. Therefore, time integrated values will be analyzed below. The decays to the following final states will be considered as suggested in Ref. [40]:

- Hadron final states f and $\bar{f}$ which do not have a definite CP-parity, for example, $K^-\pi^+$, which is a Cabibbo-favored (CF) decay of D^0, or doubly Cabibbo suppressed (DCF) decay of $\bar{D}^0$;
- Semileptonic and leptonic final states, l^+ and l^-, which, without mixing, uniquely determine the flavor of a D^0-meson;
- The states which are eigenstates of CP parity, S_+ and S_-.

Under the assumption of CP invariance, the probability of producing two D^0 mesons in various combinations in the final state depends on the following parameters: x, y, the amplitudes $A_f = \langle f|D^0\rangle$, $A_l = \langle l^+|D^0\rangle$, $A_{S_\pm} = \langle S_\pm|D^0\rangle$, the absolute value and phase of the ratio for the DCF and CF amplitudes $r_f e^{-\delta f} = -\langle f|\bar{D}^0\rangle/\langle f|D^0\rangle$. One can also determine the following parameters: $R_M \equiv (x^2+y^2)/2$, $z_f \equiv 2\cos\delta_f$, $w_f \equiv 2\sin\delta_f$. The ratios of decay probabilities of the $D^0\bar{D}^0$ system to various final states are shown in Table 1.7. Γ_{jk} means D^0 decay to the j state and $\bar{D}^0$ to the k state. Γ_j means D^0 decay to the j state and $\bar{D}^0$ to any final state.

As shown in the Table 1.7, evidence of events $D^0\bar{D}^0 \to (K^-\pi^+)(K^-\pi^+)$ and $D^0\bar{D}^0 \to (K^-e^+\nu_e)(K^-e^+\nu_e)$ in $\psi(3770)$ decays is possible via mixing only. For 10^9 $D^0\bar{D}^0$ events and for $R_M = 0.8\times10^{-4}$ obtained using the measured x and y values, it is expected to detect about 150 of these events. Results of Ref. [40] were used for estimation of the detection efficiency which corresponds to CLEO performance. Thus, a statistical sensitivity for a measurement of R_M using these two decays only is about 5×10^{-6}. A systematic uncertainty will mainly depend on the quality of particle identification.

The probabilities of inclusive $D^0\bar{D}^0$ decays to the $S_\pm X$ final states are proportional to $(1\mp y)$ [40]. This allows to measure a y parameter. For double ratios shown in the first and second rows of Table 1.7, the substantial part of systematic errors, which originates from data-MC simulation difference in track reconstruction and particle identification, cancels. A statistical precision of y

determined from the ratio $(1/4)\cdot(\Gamma_{lS_+}\Gamma_{S_-}/\Gamma_{lS_-}\Gamma_{S_+}-\Gamma_{lS_-}\Gamma_{S_+}/\Gamma_{lS_+}\Gamma_{S_-})$ was estimated in [41] to be $26/\sqrt{N_{DD}}$, where N_{DD} is the number of produced $D^0\bar{D}^0$ pairs. For $N_{DD}=10^9$ it equals 0.0008, i.e., 2.5 times better than the current experimental precision.

The value of the strong phase δ_f in the $K^-\pi^+$ final state, which is important, for example, for a measurement of $D^0\bar{D}^0$ mixing at B-factories, can be measured using the relations listed in the third and fourth rows of Table 1.7. The expected statistical precision for a measurement of $\cos\delta_f$ is estimated as $444/\sqrt{N_{DD}}=0.014$ [41], that corresponds to a precision of 0.05 for δ_f. At the present time the average value of this parameter is $0.39^{+0.17}_{-0.18}$.

Measurements, which can be performed with the $D^0\bar{D}^0$ system in the C-even state, have the best sensitivity for y. For a measurement of y with a precision of 0.0008 from the ratio $\Gamma_{fl^+}/\Gamma_{fl^-}$, 3×10^8 $D^0\bar{D}^0$ pairs are required. This number of C-even $D^0\bar{D}^0$ pairs can be produced in the process $e^+e^-\to D^0\bar{D}^{*0}\to D^0\bar{D}^0\gamma$ with an integrated luminosity of 250 fb^{-1} collected at an energy of 4.02 GeV. This measurement is also sensitive to the parameter x. However, as it is shown in Table 1.7, a sensitivity to x is worse than for y due to δ_f infinitesimality. As it was shown in a recent paper [42], this problem can be successfully solved in case of a three-particle decay of D^0, for example, to $K_S\pi^+\pi^-$ or $K^+\pi^-\pi^0$. An important feature of the suggested method is that for the C-odd $D^0\bar{D}^0$ state all effects of mixing, which have impact on the density of events on the Dalitz plot, cancel in the first order of x and y. In the case of the C-even one, the effects of mixing are doubled compared to a non-coherent D^0 decay. Thus, in this experiment there is a possibility to measure x and y by a direct comparison of the distribution of events on the Dalitz plot for the C even and odd $D^0\bar{D}^0$ states. As it was shown in Ref. [42], statistical errors for x and y are approximately equal. It is expected that many systematic errors in this measurement will cancel because the states with opposite charge parity will be produced simultaneously and in similar kinematic states during data taking. Furthermore, unlike other methods described above, this method does not require measuring absolute probabilities of D^0 decays. It can be estimated that for an integrated luminosity of about 1 ab^{-1}, a precision of measuring mixing parameters will be not worse than at the Super B-factory for an integrated luminosity of 10 ab^{-1} [43].

1.4.4 Search for CP violation

A search for CP violation in D decays is one of the most interesting experiments to be performed at CTF. The Standard Model predicts a very small CP asymmetry in reactions with charmed particles. The maximum effect of about 10^{-3} is expected in the Cabibbo-suppressed (CS) D decays [38]. An observation of a CP asymmetry in CF and DCS decays at any level or an asymmetry higher than 10^{-3} in CS decays will clearly indicate the presence of new BSM physics. The exceptions are the decays to the final states containing K_S or K_L, for example, $D\to K_S\pi$, in which the CP asymmetry arises from the fact that a K_S meson is not a CP eigenstate. For the decay $D^\pm\to K_S\pi^\pm$, a CP asymmetry is predicted with a relatively high accuracy, $(3.32\pm0.06)\times10^{-3}$ [38].

We can distinguish three types of CP violation:

- The direct CP violation in $\Delta C=1$ transitions reveals itself as a inequality of the amplitude of D meson decay (A_f) and the corresponding CP-conjugate amplitude ($\bar{A}_{\bar{f}}$). CP violation can be observed when the decay amplitude is a sum of two amplitudes with different weak and strong phases:
$$A_f=|A_1|e^{i(\delta_1+\phi_1)}+|A_2|e^{i(\delta_2+\phi_2)}.$$
The weak phase changes its sign under the CP transformation ($\phi_i\to-\phi_i$), while the strong phase δ_i does not.

Table 1.8: *The current values of the CP asymmetry measured in D decays.*

$D^0 \to K^-\pi^+$	$0.005 \pm 0.004 \pm 0.009$ [44]		
$D^0 \to K_S\pi^0$	$+0.001 \pm 0.013$ [45]	$D^+ \to K_S\pi^+$	$-0.013 \pm 0.007 \pm 0.003$ [44]
$D^0 \to K^+K^-$	-0.0017 ± 0.0031 [2]		
$D^0 \to K_SK_S$	-0.23 ± 0.19 [45]	$D^+ \to K_SK^+$	$-0.002 \pm 0.015 \pm 0.009$ [44]
$D^0 \to \pi^+\pi^-$	0.002 ± 0.004 [2]		
$D^0 \to \pi^0\pi^0$	$+0.001 \pm 0.048$ [45]		
$D^0 \to K^-\pi^+\pi^0$	$+0.002 \pm 0.004 \pm 0.008$ [22]	$D^+ \to K^-\pi^+\pi^+$	$-0.005 \pm 0.004 \pm 0.009$ [22]
$D^0 \to K_S\pi^+\pi^-$	$-0.009 \pm 0.021^{+0.016}_{-0.057}$ [46]	$D^+ \to K_S\pi^+\pi^0$	$+0.003 \pm 0.009 \pm 0.003$ [22]
$D^0 \to K^+K^-\pi^0$	$-0.0100 \pm 0.0167 \pm 0.0025$ [47]	$D^+ \to K^+K^-\pi^+$	$+0.003 \pm 0.006$ [2]
$D^0 \to \pi^+\pi^-\pi^0$	$+0.0031 \pm 0.0041 \pm 0.0017$ [47]	$D^+ \to \pi^+\pi^-\pi^+$	-0.017 ± 0.042 [48]
$D^0 \to K^-\pi^+\pi^+\pi^-$	$+0.007 \pm 0.005 \pm 0.009$ [22]	$D^+ \to K^-\pi^+\pi^+\pi^0$	$+0.010 \pm 0.009 \pm 0.009$ [22]
$D^0 \to K^+\pi^-\pi^+\pi^-$	-0.018 ± 0.044 [49]	$D^+ \to K_S\pi^+\pi^+\pi^-$	$+0.001 \pm 0.011 \pm 0.006$ [22]
$D^0 \to K^+K^-\pi^+\pi^-$	$-0.082 \pm 0.056 \pm 0.047$ [50]	$D^+ \to K_SK^+\pi^+\pi^-$	$+0.001 \pm 0.011 \pm 0.006$ [50]

- CP violation in D^0–$\bar{D}^0$ mixing due to $\Delta C = 2$ transitions reveals itself in a deviation of the ratio $R_m = |p/q|$ from unity.
- In decays of neutral D mesons CP violation can be observed in the interference of decays with mixing ($D^0 \to \bar{D}^0 \to f$) and without it ($D^0 \to f$). This type of CP violation is described by the parameter

$$\varphi = \arg\lambda_f = \arg\left(\frac{q}{p}\frac{\bar{A}_f}{A_f}\right).$$

CP violation in mixing leads to the difference between the widths of semileptonic decays with a wrong sign of the decay lepton $\Gamma(\bar{D}^0 \to l^+X) \neq \Gamma(D^0 \to l^-X)$. For example, in $\psi(3770)$ decays the following asymmetry can be measured

$$A_{SL} = \frac{\Gamma_{l^+l^+} - \Gamma_{l^-l^-}}{\Gamma_{l^+l^+} + \Gamma_{l^-l^-}} = \frac{1 - |q/p|^4}{1 + |q/p|^4}.$$

For 10^9 $D^0\bar{D}^0$ pairs, about 60 $(K^\pm e^\mp\nu)(K^\pm e^\mp\nu)$ events are expected to be produced. With these statistics, the $|q/p|$ ratio will be determined with about 6% accuracy. The current value of the parameter $|q/p|$ is $0.86^{+0.17}_{-0.15}$.

Direct CP violation can be observed as a difference between the decay widths for charged D mesons:

$$A^{CP}_\pm = \frac{\Gamma(D^- \to f^-) - \Gamma(D^+ \to f^+)}{\Gamma(D^- \to f^-) + \Gamma(D^+ \to f^+)}.$$

For neutral D mesons, all three types of CP violation contribute to the same asymmetry parameter. The current values of the CP asymmetry measured in D decays are listed in Table 1.8.

In Ref. [22] the CP asymmetries were measured by the CLEO detector using a data sample of 10^6 D^+D^- pairs. At CTF, for many decays the statistical error of asymmetry can be decreased to a level of 10^{-3}-10^{-4}. The systematic error is dominated by uncertainties in track reconstruction and particle identification. The reconstruction and identification efficiencies are different for pions and kaons of different charges and are usually not reproduced in simulation with sufficient accuracy. At CTF a level of 10^{-3} for the systematic uncertainty seems achievable. For example, in the BABAR and Belle measurements of the asymmetries for the decays $D^0/\bar{D}^0 \to K^+K^-$, $\pi^+\pi^-$ [51, 52], the

systematic uncertainty due to a difference in the detection efficiency for π^+ and π^- mesons used for D tagging was decreased to the 10^{-3} level. The thickness of material before and inside the tracking system of the CTF detector should be minimized to reduce the systematic uncertainty for charge asymmetry measurements.

The CP asymmetry in decays of neutral D mesons can be represented as a sum of three terms. For example, for the decay into the CP eigenstate $\eta_f^{CP} = \pm 1$ [53]

$$A_f^{CP} = a_f^d + a_f^m + a_f^i,$$

$$a_f^m = -\eta_f^{CP}\frac{y}{2}(R_m - R_m^{-1})\cos\varphi,$$

$$a_f^i = \eta_f^{CP}\frac{x}{2}(R_m + R_m^{-1})\sin\varphi,$$

where a_f^d is a CP asymmetry in the decay, φ is a relative weak phase between the amplitudes for the decays $D^0 \to f$ and $D^0 \to \bar{D}^0 \to f$. The magnitude of the second term a_f^m is determined mainly by CP violation in mixing. The third term a_f^i is dominated by CP violation in the interference. The mixing leads to a difference in the time dependencies of the D^0 and $\bar{D}^0$ decay probabilities. This allows to localize and measure the contribution of the second and third terms. In experiments at B-factories [54, 55] the value

$$\delta Y = a_f^m + a_f^i = (-0.12 \pm 0.25) \times 10^{-2}$$

was obtained for the final states K^+K^- and $\pi^+\pi^-$. The formula given above is valid for incoherent production of D^0 and $\bar{D}^0$ mesons. At CTF such an asymmetry will be studied for decays of D^0 mesons produced in the reaction $e^+e^- \to D^{*-}D^+ \to \pi^- D^0 D^+$. For coherent $D^0\bar{D}^0$ production, the formula for A^{CP} is modified and becomes dependent on the decay used for tagging. This makes it possible to separate various contributions to the CP asymmetry without studying their time dependence. For example, the reaction $D^0\bar{D}^0 \to f_1 f_2$, where f_1 and f_2 are the states with the same CP parity, is forbidden at the $\psi(3770)$ resonance if CP is conserved. The probability of the decay is described by the following formula [56]:

$$\Gamma_{f_1 f_2} = \frac{1}{2R_m^2}\left[(2 + x^2 - y^2)|\lambda_{f_1} - \lambda_{f_2}|^2 + (x^2 + y^2)|1 - \lambda_{f_1}\lambda_{f_2}|^2\right]\Gamma_{f_1}\Gamma_{f_2}.$$

Since the terms corresponding to the contribution of mixing are proportional to the squares of x and y, the difference between direct CP violation for decays $D^0 \to f_1$ and $D^0 \to f_2$ is measured in this reaction.

At CTF with 10^9 $D^0\bar{D}^0$ pairs the sensitivity level of 10^{-3} can be reached for the asymmetry difference between, for example, the K^+K^- and $\pi^+\pi^-$ final states. A similar measurement can be performed using the reaction $e^+e^- \to D^{*0}\bar{D}^0 \to \gamma D^0\bar{D}^0$. In this case the difference between CP asymmetries for states with opposite CP parities is measured.

Another example is a measurement of the asymmetry

$$A_{fl}^{CP} = \frac{\Gamma(l^-X, f) - \Gamma(l^+X, f)}{\Gamma(l^-X, f) + \Gamma(l^+X, f)}.$$

Here one D meson decays semileptonically, while the other to a CP eigenstate. Neglecting direct CP violation [57]

$$A_{fl}^{CP} = (1 + \eta)(a_f^m + a_f^i),$$

where η is the C parity of the $D^0\bar{D}^0$ pair. It is seen that at $\eta = -1$, i.e., in $\psi(3770)$ decays, mixing does not contribute to the measured asymmetry, while for $\eta = 1$, i.e., in the reaction $e^+e^- \to D^{*0}\bar{D}^o \to \gamma D^0\bar{D}^0$ the mixing contribution to the asymmetry is two times larger than that for D^0 mesons produced incoherently. Measurements performed in these two reactions allow to separate the contributions of direct and indirect mixing.

There are other powerful methods to search for CP violation. In Ref. [58] it is proposed to use the difference between the probabilities of decays of untagged D^0 mesons to the charge-conjugate states, for example, $K^-\pi^+$ and $K^+\pi^-$, to extract the parameter $\sin\varphi$. The Dalitz analysis of three-body decays allows to measure CP asymmetries for different resonant intermediate states (see, for example, the results of Ref. [59]). An interference between the CP-conserving and CP violating amplitudes in the Dalitz-plot distributions can increase the sensitivity of a search for CP violation. In the four-body decays, a search for CP violation can use T-odd moments [60] or triple products of momenta [61]. Using these methods at CTF, one can measure the CP asymmetry in D decays with an accuracy of about 10^{-3} for both direct and indirect mechanisms of CP violation.

1.4.5 D-meson rare decays

Rare decays of D mesons are a tool for a search for new physics beyond the Standard Model [62]. The rare D decays most suitable for this purpose are:

1. flavor-changing neutral current (FCNC) decays via the weak neutral current, providing the transition between c and u quarks,
2. lepton-flavor-violating (LFV) decays,
3. lepton-number-violating (LV) decays.

Two latter types of decays are forbidden in the Standard Model. In SM decays via a $c \to u$ transition are described by loop diagrams and are strongly suppressed. For example, the probabilities for the $c \to ul^+l^-$ and $c \to u\gamma$ transitions are estimated to be of the order 10^{-8}. For specific exclusive D decays, however, the contributions of large-distance dynamics should be taken into account. For example, the dominant contribution to the decay $D^+ \to \pi^+l^+l^-$ comes from the transition via the intermediate $\pi^+\phi$ state followed by the decay $\phi \to l^+l^-$. As a result, the $D \to X\gamma$ and $D \to Xl^+l^-$ branching fractions, where X is a hadronic state, increase up to 10^{-5}–10^{-6}. Two of such decays have been measured and have the values of the branching fractions consistent with SM: $B(D^0 \to \phi\gamma) = (2.4^{+0.7}_{-0.6}) \times 10^{-5}$ [63] and $B(D^+ \to \pi^+\phi \to \pi^+\mu^+\mu^-) = (1.8 \pm 0.5 \pm 0.6) \times 10^{-6}$ [64].

Due to the large-distance contributions, which are difficult to calculate accurately in the framework of SM, decays like $D \to X\gamma$ become weakly sensitive to new physics effects. But even for these decays, observables having some "new physics" sensitivity can be found. For example, in Ref. [65] it is proposed to measure the difference $R = B(D^0 \to \rho^0\gamma)/B(D^0 \to \omega\gamma) - 1$, which is estimated to be $(6 \pm 15)\%$ in SM. In the Minimal Supersymmetric Standard Model (MSSM), with some choice of model parameters the probability of the transition $c \to u\gamma$ can reach 6×10^{-6} and the value of R can be of the order 1 [65].

In decays $D \to Xl^+l^-$ one can analyze the spectrum of the lepton-pair invariant mass and select mass regions sensitive to the small-distance contributions. In Fig.1.4 taken from Ref. [66] the lepton invariant mass spectra are shown for the decays $D^+ \to \pi^+e^+e^-$ and $D^0 \to \rho^0e^+e^-$ in SM and MSSM. Restrictions on the MSSM parameters can be obtained with a sensitivity to the decay at the level of 10^{-6}. The predictions for decays $D \to Xl^+l^-$ obtained in different SM extensions can be found in Refs. [62, 66, 67].

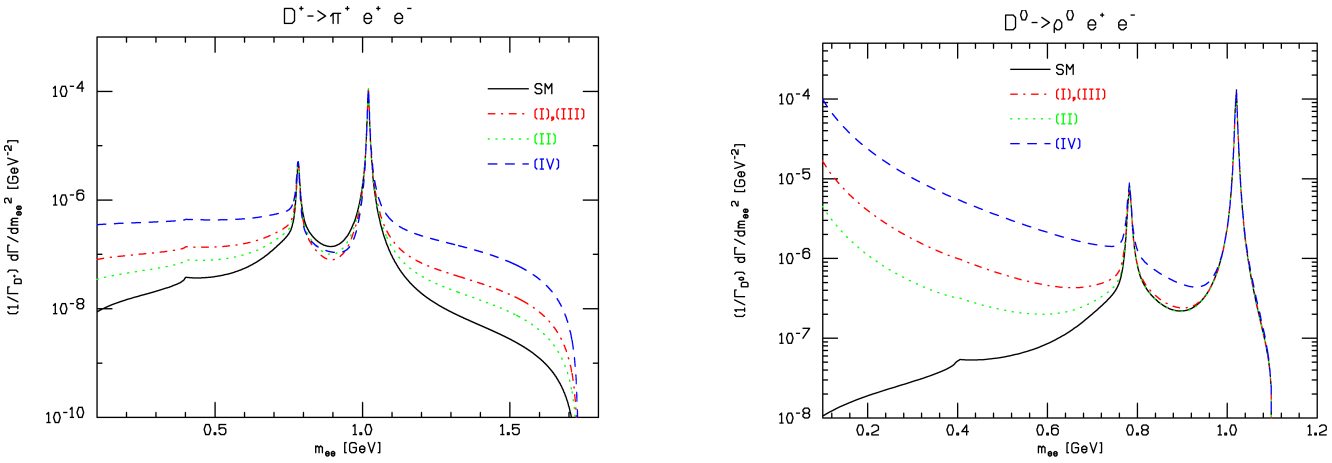

Figure 1.4: *The spectra of the lepton-pair invariant mass for the decays $D^+ \to \pi^+ e^+ e^-$ (left) and $D^0 \to \rho^0 e^+ e^-$ (right). The solid curve represents the SM prediction, while the dashed curves indicate the MSSM predictions for different sets of model parameters.*

Table 1.9: *The experimental upper limits on the rare D and D_s decays in units of 10^{-6}.*

$D^0 \to \gamma\gamma$	26 [68]	$D^+ \to \pi^+ e^+ e^-$	7.4 [71]
$D^0 \to e^+ e^-$	1.2 [69]	$D^+ \to \pi^+ \mu^+ \mu^-$	3.9 [64]
$D^0 \to \mu^+ \mu^-$	1.3 [69]	$D^+ \to \pi^+ e^+ \mu^-$	10.8 [72]
$D^0 \to \mu^+ e^-$	0.81 [69]	$D^+ \to \rho^+ \mu^+ \mu^-$	560 [73]
$D^0 \to \pi^0 e^+ e^-$	45 [70]		
$D^0 \to \rho^0 e^+ e^-$	100 [70]	$D_s^+ \to K^+ e^+ e^-$	6.6 [72]
$D^0 \to \pi^0 e^+ \mu^-$	86 [70]	$D_s^+ \to K^+ \mu^+ \mu^-$	25.4 [72]
$D^0 \to \rho^0 e^+ \mu^-$	49 [70]	$D_s^+ \to K^+ e^+ \mu^-$	3.6 [72]

Another class of decays with the $c \to u$ transition includes decays of a neutral D meson into the lepton or photon pair. SM predicts $B(D^0 \to \gamma\gamma) \simeq 3.5 \times 10^{-8}$ and $B(D^0 \to \mu^+ \mu^-) \sim 10^{-12}$ [66]. The $D^0 \to \mu^+ \mu^-$ branching fraction can reach 3.5×10^{-6} in supersymmetric models with R-parity violation. These models give also large values for the branching fractions of the following LFV decays: $B(D^0 \to \mu^+ e^-) < 10^{-6}$, $B(D^+ \to \pi^+ \mu^+ e^-) < 3 \times 10^{-5}$, $B(D^0 \to \rho^0 \mu^+ e^-) < 1.4 \times 10^{-5}$.

In Table 1.9 the current upper limits on the rare D and D_s decays are listed. At CTF a sensitivity of 10^{-8} to rare D decays can be reached.

1.5 Charmed baryons

Charmed baryons, which can be produced at CTF in the reaction $e^+ e^- \to B_c \bar{B}_c$, consist of two light quarks (u, d, s) and a heavy c quark. A pair of light quarks forms two SU(3) multiplets: the antisymmetric antitriplet and the symmetric sextet. In S-wave low-lying baryons, the flavor

Table 1.10: *Parameters of the S-wave charmed baryons [2]*

	Structure	J^P	Mass, MeV	Width,MeV	Decay
Λ_c^+	udc	$(1/2)^+$	2286.46 ± 0.14	(200 ± 6) fs	weak
Ξ_c^+	usc	$(1/2)^+$	$2467.8^{+0.4}_{-0.6}$	(442 ± 26) fs	weak
Ξ_c^0	dsc	$(1/2)^+$	$2470.88^{+0.34}_{-0.8}$	112^{+13}_{-10} fs	weak
Σ_c^{++}	uuc	$(1/2)^+$	2454.02 ± 0.18	2.23 ± 0.30	$\Lambda_c^+\pi^+$
Σ_c^+	udc	$(1/2)^+$	2452.9 ± 0.4	< 4.6	$\Lambda_c^+\pi^0$
Σ_c^0	ddc	$(1/2)^+$	2453.76 ± 0.18	2.2 ± 0.4	$\Lambda_c^+\pi^-$
$\Xi_c'^+$	usc	$(1/2)^+$	2575.6 ± 3.1	—	$\Xi_c^+\gamma$
$\Xi_c'^0$	dsc	$(1/2)^+$	2577.9 ± 2.9	—	$\Xi_c^0\gamma$
Ω_c^0	ssc	$(1/2)^+$	2695.2 ± 1.7	(69 ± 12) fs	weak
Σ_c^{*++}	uuc	$(3/2)^+$	2518.4 ± 0.6	14.9 ± 1.9	$\Lambda_c^+\pi^+$
Σ_c^{*+}	udc	$(3/2)^+$	2517.5 ± 2.3	< 17	$\Lambda_c^+\pi^0$
Σ_c^{*0}	ddc	$(3/2)^+$	2518.0 ± 0.5	16.1 ± 2.1	$\Lambda_c^+\pi^-$
Ξ_c^{*+}	usc	$(3/2)^+$	$2645.9^{+0.5}_{-0.6}$	< 3.1	$\Xi_c\pi$
Ξ_c^{*0}	dsc	$(3/2)^+$	2645.9 ± 0.5	< 5.5	$\Xi_c\pi$
Ω_c^{*0}	ssc	$(3/2)^+$	2765.9 ± 2.0	—	$\Omega_c^0\gamma$

symmetry and spin are related to each other: the total spin of light quarks is equal to 0 for the antitriplet and 1 for the sextet. In combination with the c quark, the antitriplet produces three states with spin 1/2 (Λ_c^+, Ξ_c^+, Ξ_c^0), while the sextet gives six states with spin 1/2 ($\Sigma_c^{++,+,0}$, $\Xi_c'^+$, $\Xi_c'^0$, Ω_c^0) and six states with spin 3/2 ($\Sigma_c^{*++,+,0}$, Ξ_c^{*+}, Ξ_c^{*0}, Ω_c^{*0}). All 15 S-wave charmed baryons have been observed. Their parameters are listed in Table 1.10.

Many excited charmed baryons are expected. In particular, the quark model predicts 63 P-wave states [74]. Sixteen of the excited states with masses in the range from 2.6 to 3.1 GeV have been observed [2, 75].

In recent years physics of charmed baryons has been studied mainly at B-factories. In spite of the large number of produced charmed baryons (B factories produced about 10^7 Λ_c), their properties are rather badly known. There is practically no experimental information about the quantum numbers of baryons and absolute branching fractions of their decays. The potential of CTF in a study of charmed baryons depends strongly on the cross sections for the reactions $e^+e^- \to B_c\bar{B}_c$. For the reaction $e^+e^- \to \Lambda_c\bar{\Lambda}_c$ the cross section was measured by Belle [76]. The cross section is maximal at the energy about 4.65 GeV. The maximal value is about 0.5 nb. Such a large cross section value can be explained by a possible presence of a $c\bar{c}$ resonance near the $\Lambda_c\bar{\Lambda}_c$ threshold. With an integrated luminosity of 200 fb^{-1} CTF will produce 10^8 $\Lambda_c\bar{\Lambda}_c$ pairs. This will allow to perform a detailed study of Λ_c properties with the use of the double-tag method. For other charmed baryons the experimental data on the reactions $e^+e^- \to B_c\bar{B}_c$ are absent. Without a resonance enhancement the expected cross section does not exceed 10 pb. The physics

program for baryons depends on the maximum energy of CTF. The most interesting physics task is a detailed study of weak decays of the charmed baryons $\Lambda_c^+(2286)$, $\Xi_c^+(2468)$, $\Xi_c^0(2471)$, and $\Omega_c^0(2698)$. The required maximum energies of the factory are 4.7, 5.1 and 5.5 GeV.

1.6 τ lepton physics

At CTF τ leptons are produced in the process $e^+e^- \to \tau^+\tau^-$. Its cross section grows fast from 0.1 nb near threshold of $\tau^+\tau^-$ production ($2E = 3.55$ GeV) to 2.5 nb near threshold of D meson production ($2E \approx 3.7$ GeV) and reaches its maximum of 3.5 nb at $2E = 4.25$ GeV. During the CTF operation about 10^{10} pairs of τ leptons will be produced, an order of magnitude larger than at B factories, but smaller than statistics expected at Super B factories (about 5×10^{10}).

One should note that the existing accuracy of many τ lepton parameters, e.g., its decay widths, is currently limited by systematic effects. For precise measurements of decay probabilities and hadronic spectral functions, a dedicated near-threshold run is planned. At threshold τ leptons are produced at rest allowing to suppress background by applying an additional condition on kinematics of hadronic decays: $2m_\tau E_{had} = m_\tau^2 + m_{had}^2$, where E_{had} and m_{had} are energy and invariant mass of the hadronic system. Use of this condition allows to select τ events with the tagging method. The remaining background can be measured running below threshold of τ lepton production. With an integrated luminosity of 1 ab^{-1} collected near the $\tau + \tau-$ threshold about 10^8 τ lepton pairs will be produced.

Spectral functions measured in hadronic decays of the τ can be used to determine the strong interaction constant α_s [77] (see also Ref. [78]). Data from hadronic decays with $\Delta S = 1$ are used to determine the mass of the s-quark m_s and the CKM matrix element V_{us} [79]. Potentially τ lepton decays provide a source for the most precise measurements of α_s, m_s and V_{us}.

A high precision measurement of the probabilities of leptonic decays as well as decays $\tau^+ \to \pi^+\nu_\tau$ and $\tau^+ \to K^+\nu_\tau$ will result in a significant improvement of lepton universality tests in the charged lepton sector.

For precision tests of SM and lepton universality, knowledge of the τ lepton mass is mandatory. The most precise method of τ lepton mass determination is a measurement of the energy dependence of the cross section for the process $e^+e^- \to \tau^+\tau^-$ near threshold. Such measurements require high-precision energy calibration of the collider using resonance depolarization or back Compton scattering.

An important test of SM is a study of the Lorentz structure of the amplitude for the $\tau \to l\nu_l\nu_\tau$ decay. A near-threshold measurement will allow a determination of the lepton energy spectrum in this decay without background. The spectrum is parametrized using four Michel parameters [80], two of which require knowledge of τ lepton polarization. The polarization degree can be measured via the decay of the second τ, e.g., via the decay $\tau \to \rho\nu$. A longitudinal polarization of initial beams would allow a more efficient usage of the collected data samples and minimize a systematic uncertainty of polarization-dependent parameters.

LFV decays of τ lepton, such as $\tau \to l\gamma$, $\tau \to lll^{(\prime)}$ or $\tau \to lh$, where l, $l^\prime$ — electron or muon, and h is a hadronic system, are sensitive to effects of New Physics. Different models beyond SM predict probabilities of these decays at the level of 10^{-7}–10^{-10} (see, for example, Ref. [81]). Experimental upper limits on the probabilities of LFV decays achieved at the B factories are in the range 10^{-7} to 2×10^{-8} [2] and already constrain the space of parameters of some models. For most of the decays, a much higher sensitivity is expected in future experiments at super-B factories. However, for some decays in which an upper limit on the decay probability is determined by background, the CTF sensitivity can be higher than at super-B factories. This is, in particular,

true for $\tau \to \mu\gamma$ decay, very important in a search for New Physics. At B factories an upper limit for the probability of this decay is determined by the background from the process $e^+e^- \to \tau^+\tau^-\gamma$, not significant at CTF.

CP violation in the quark sector does not explain the observed baryon asymmetry of the universe. Therefore, it is reasonable to search for it in the lepton sector, in particular, in τ lepton decays. CP violation can be observed in hadronic τ decays, provided that there are two interfering amplitudes with different strong and weak phases. Under CP transformation, $e^{i\delta_w+i\delta_s}$ is transformed into $e^{-i\delta_w+i\delta_s}$, where δ_w and δ_s are relative strong and weak phases of two amplitudes. This results, for example, in the non-equality of the widths of CP conjugate decays. The asymmetry $A_{CP} = (\Gamma(\tau^+ \to f+) - \Gamma(\tau^- \to f-))/(\Gamma(\tau^+ \to f+) + \Gamma(\tau^- \to f-))$ is proportional to $\sin\delta_s \sin\delta_w$. In SM τ lepton decays are described by a single amplitude with a W boson exchange. Therefore, observation of CP asymmetry would be an explicit indication of physics beyond SM. An only exception is $\tau \to \pi K_{S(L)}\nu_\tau$ decay, in which the CP asymmetry at the level of 3×10^{-3} [82] arises in SM because of CP violation in kaons. Suggestions for using various decays for CP violation are considered in Refs. [83, 84, 85, 86, 87, 88]. The most promising decays are $\tau \to K\pi^0\nu_\tau$, $\tau \to \rho\pi\nu_\tau$, $\tau \to \omega\pi\nu_\tau$, $\tau \to a_1\pi\nu_\tau$. In addition to measuring the asymmetry in the decay width, A_{CP} defined above, it is also suggested to use a so called modified asymmetry, when experimental differential distributions of the final hadrons are integrated with a specially selected kernel over a limited range of phase space, and an asymmetry in the triple product $\boldsymbol{\sigma} \cdot (\boldsymbol{p_1} \times \boldsymbol{p_2})$, where $\boldsymbol{\sigma}$, $\boldsymbol{p_1}$, $\boldsymbol{p_2}$ are a τ polarization vector and momenta of two final hadrons, respectively. It is worth noting that the asymmetry in the triple product is proportional to $\cos\delta_s \sin\delta_w$, i.e., a non-zero difference of the strong phases is not needed for its observation.

A search for CP violation was performed in the CLEO experiment using 10^7 τ-lepton pairs for $\tau^\pm \to \pi^\pm\pi^0\nu$ [89] and $\tau^\pm \to K_S\pi^\pm\nu$ [90] decays. One can expect an increase of sensitivity after analysis of the data samples accumulated at the B factories and later at super-B factories and CTF. Longitudinal polarization of the initial beams will significantly increase sensitivity in searches for CP violation in τ lepton decays.

1.7 Measurement of $e^+e^- \to$ hadrons

The c.m. energy range from 3 to 6 GeV is almost asymptotic for u-, d-, and s quarks. There are no resonances made of light quarks here, but for the c quark the resonance region starts just in this energy range. Only after 5 GeV the cross section of the process $e^+e^- \to c\bar{c}$ starts reaching asymptotics. To reach a 1% accuracy in the cross section we need a detailed scan with a step of a few MeV and an integrated luminosity of 10 pb^{-1} per point or about 10 fb^{-1} in total in the whole energy range.

Below 3 GeV such an accuracy for the total cross section can be reached using ISR. Since in this energy range the number of possible final states in the process $e^+e^- \to$ hadrons is relatively small, the total cross section can be determined as a sum of cross sections for different exclusive channels. This method has been tried in the BABAR experiment [91].

In addition, CTF will be able to provide high luminosity also below 3 GeV, in the c.m. energy range from 2 to 3 GeV. Among physical tasks is a measurement of various exclusive cross sections and intermediate mechanisms for final states of light quarks and spectrometry of the ρ, ω and ϕ excitations. Besides that running at the threshold of a baryon-antibaryon pair production in a polarized mode of CTF will allow a study of the baryon form factors near threshold including a unique chance of doing that for polarized baryons. Particular important is an opportunity to obtain polarized antineutrons and antiprotons, and measure a polarization part of the cross section

of their annihilation.

For spectrometry of charm, an important task for CTF is to measure exclusive cross sections for production of charmed mesons and baryons.

1.8 Two-photon physics

Today two-photon physics is an important sector of particle physics. In principle, it is physics for photon colliders extensively discussed now. However, e^+e^- colliders as a source of two-photon collisions have one important advantage, one or two of the virtual colliding photons can be strongly off-shell. This provides additional possibilities compared to the collisions of real photons.

Physical tasks first of all include a study of C-even resonances consisting of both light and charm quarks with quantum numbers $J^{PC} = 0^{++}$, 0^{-+}, 2^{-+}, 2^{++}. When one of the photons is strongly off shell, particles with $J = 1$ can also be produced, including those with exotic quantum numbers $J^{PC} = 1^{-+}$. High luminosity of CTF will allow not only a determination of the two-photon widths of the resonances, but also a study of their rare decay modes. A separate problem also requiring high luminosity is a measurement of transition form factors in the processes $\gamma^* \to \gamma M$ and $\gamma^* \to \gamma^* M$, where M is a C-even resonance.

Note also the importance of measuring the total cross sections of $\gamma\gamma \to$ hadrons as well as the cross sections of separate channels like $\gamma\gamma \to \rho\rho$, $p\bar{p}$, $\phi\phi$, $f_0 f_0$ etc. CTF gives a chance for measuring cross sections with accuracy of about 1%.

In such studies, to suppress a background from e^+e^- annihilation into hadrons, one needs a high hermeticity of the detector as well as a low-angle tagger to detect scattered electrons.

1.9 Conclusions

An important difference of CTF compared to the existing B factories at SLAC and KEK and the ϕ factory at Frascati is its ability to run in the broad energy range whereas the colliders mentioned above run basically at a single c.m. energy. This complicates the experimental facilities, both a collider and a detector, but of course makes much broader a physical program.

And one more rather general conclusion. In the discussed energy range a predictive power of the existing theory is rather limited. Our recent experience shows that some particles, e.g., $Y(4260)$ or $X(2150)$, were discovered accidentally and their interpretation is still unclear. Therefore, an experimental study is still most important and one can hope that CTF will help to solve many of the existing problems.

Chapter 2

Conceptual design of the detector for the Super $\mathcal{CT}$ factory

2.1 General concept of the detector

The physics program of experiments at the Super $c\tau$ factory with a peak luminosity of $10^{35}\,\mathrm{cm}^{-2}\mathrm{s}^{-1}$ in the region $2E = 2 \div 5\,\mathrm{GeV}$ is dedicated to studies of rare decays of the D mesons, τ lepton, $D^0\bar{D}^0$ oscillations and searches for yet unobserved lepton-flavor-violating decays of the τ, in particular, $\tau \to \mu\gamma$. This program requires a construction of a universal magnetic detector with the field of about 1 T. The detector should feature:

- an extremely high momentum resolution for charged particles and a good energy resolution for photons;
- a particle identification system with nearly record parameters among existing detectors or those under construction. For selection of the rare D decays, K/π separation higher than 3σ is needed. In addition, for selection of $\tau \to \mu\gamma$ decay at a high background from π mesons robust μ/π separation up to $1.2\,\mathrm{GeV}/c$ momentum is required;
- a digitizing hardware and data acquisition system, which is able to read events at a rate of 300–400 kHz with an average event length of about 30 kB;
- a unique trigger, which is able to select physics events and suppress background under a very high detector load.

To achieve a high efficiency of data taking and to decrease time to repair detector subsystems and hardware, the detector design should satisfy the following requirements:

- digitizing hardware should reside inside the detector, 10 Gbit optical links will be used to transmit the data;
- the detector design should provide fast access to detector subsystems for repair and hardware replacement, a typical disassembling–repair–assembling time should not exceed 12 – 24 hours;
- the duration time for input (output) of the magnetic field in the main solenoid should not exceed two–three hours;

- fast access to detector subsystems using a movable radiation shield enabling personnel to work in the region and on the technological entresoles of the detector while beams are in the collider.

The design of the universal magnetic detector for CTF is based on the experience of the Budker Institute as well as that coming from the BABAR and Belle experiments.

The detector (see Fig. 2.1) contains a standard set of subsystems:

- a vacuum chamber,
- a vertex chamber,
- a drift chamber,
- a particle identification system based on a Cherenkov detector with a multilayer aerogel radiator (*Focusing Aerogel RICH — FARICH*),
- an electromagnetic calorimeter based on pure CsI crystals,
- a superconducting coil produced by traditional technology,
- an iron yoke with a muon system inside.

2.2 Vacuum chamber

The beams collide in the center of a beryllium vacuum chamber with the radius of 20 mm and the length of 600 mm. The wall thickness is 1 mm. To suppress the background from synchrotron radiation, the chamber is covered inside with a copper layer 0.05 mm thick. Such a design provides a small amount of material, about 0.6% of the radiation length, on the particle path.

2.3 Vertex chamber

The vertex chamber (VCH) is placed between the vacuum chamber of the collider and the drift chamber and increases a solid angle of the detector up to 98 %. The VCH represents a cylinder with the length of 60 cm and the inner and outer diameters equal 50 mm and 400 mm, respectively. Its task is to detect secondary vertices from the decays of short-lived particles such as K_S^0 or Λ. Furthermore, the VCH complements the drift chamber in measuring momenta of charged particles. Since the VCH is placed in the vicinity of the beam pipe, it should handle a high particle flux when the collider operates at its maximum luminosity of $10^{35}\text{cm}^{-2}\text{s}^{-1}$.

During the operation information from the VCH can be processed either together with the drift chamber to improve the momentum resolution or alone, to reconstruct secondary vertices.

Two options of the VCH are foreseen at the moment — a time projection chamber (TPC) or a stack of silicon strip layers.

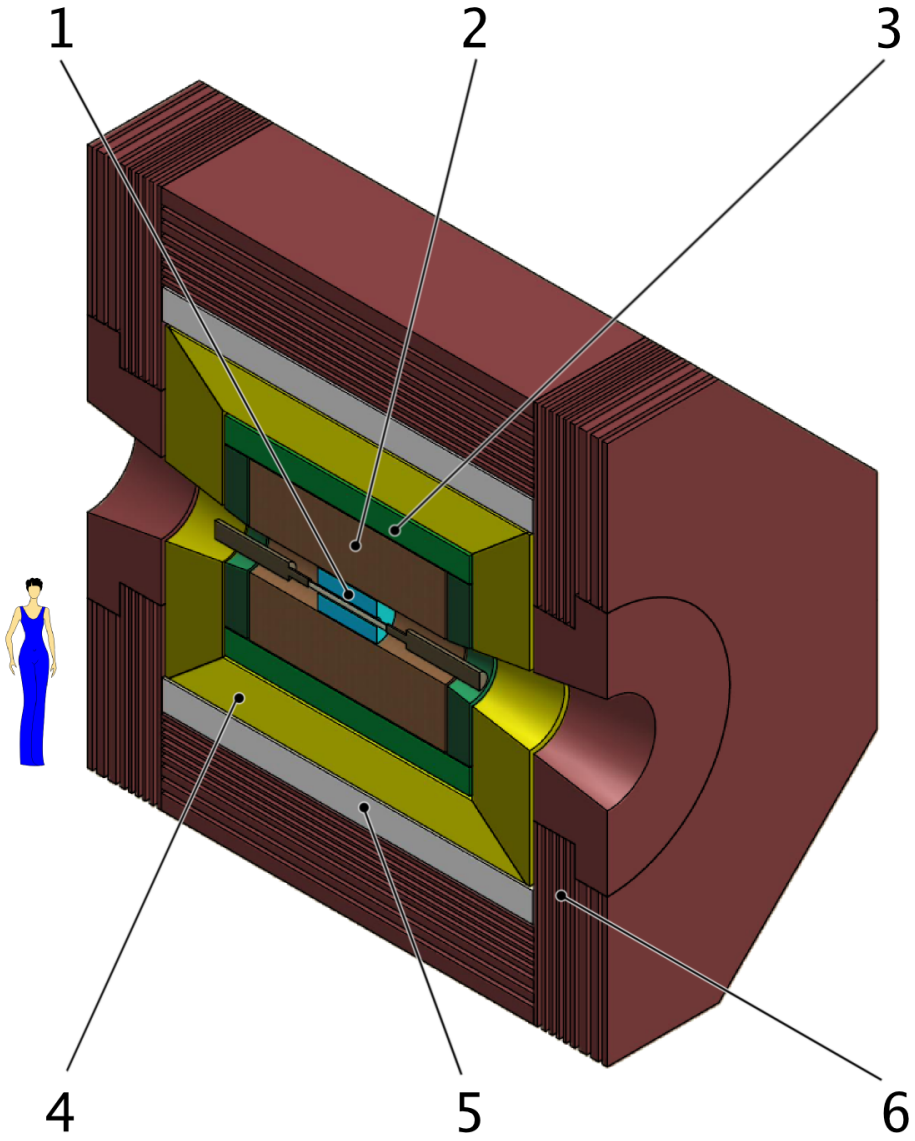

Figure 2.1: *Universal magnetic detector: 1 – vertex chamber; 2 – drift chamber; 3 – identification system based on FARICH; 4 – calorimeter; 5 – superconducting coil; 6 – yoke with a muon system.*

2.3.1 Time projection chamber

A time projection chamber [92] is a combination of the drift and proportional chamber (see Fig. 2.2). An axial electric field in the drift volume filled with a gas mixture, e.g., Ar/CO_2 80/20, is created by two endcap anode planes and a mesh cathode in the middle of the chamber. The field uniformity is preserved using a special field cage.

A charged particle traversing the sensitive volume leaves a track as a chain of clusters of the ionized gas. The linear cluster density depends on the gas. For example, for argon at normal conditions it is about 30 clusters per cm. Electrons drift with a constant velocity towards the anode planes and create avalanches detected by a sensitive pad plane providing information about two coordinates. The third coordinate of the track is a product of the drift time of each primary electron cluster and the drift velocity. Despite the relatively large drift distance of about 30 cm, a transverse diffusion is relatively small due to the longitudinal magnetic field of 1 T (see Fig. 2.3). Because of that the transverse spatial resolution can achieve 50–100 μm depending on the drift path. In the longitudinal direction the resolution is somewhat worse — about 300 μm because of larger diffusion.

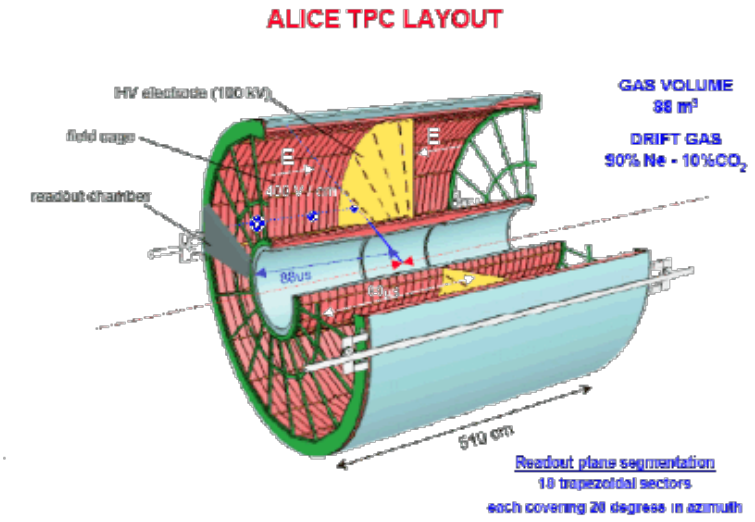

Figure 2.2: *ALICE time projection chamber (CERN).*

At the present time the multiwire proportional chamber (MWPC) is used in TPCs for detection of ionization clusters. Such chambers cannot work in the continuous mode because of a backflow of ions resulting in a space charge accumulation which leads to an electric field distortion. In its turn it deteriorates the spatial resolution. Therefore, a special protection mesh is used to prevent such an effect. This mesh opens access to the MPWC in accordance with the external trigger signal. This inavoidably leads to a large dead time after each event which leads to a loss of physics events.

A new generation of colliders including the CTF will have a very small time between consequent events, thus a standard TPC cannot be used. To overcome this problem, several new readout schemes based on the novel micropattern gas technologies were suggested. For example, the $\overline{P}ANDA$ Collaboration is developing a TPC [93] with the continuous readout using gas electron multipliers (GEM) [94]. A similar chamber is being designed for a detector for the international linear collider by the LC TPC Collaboration [95]. Besides the GEM option, the LC TPC Collaboration also studies a possibility of using the Micromegas for signal amplification (see

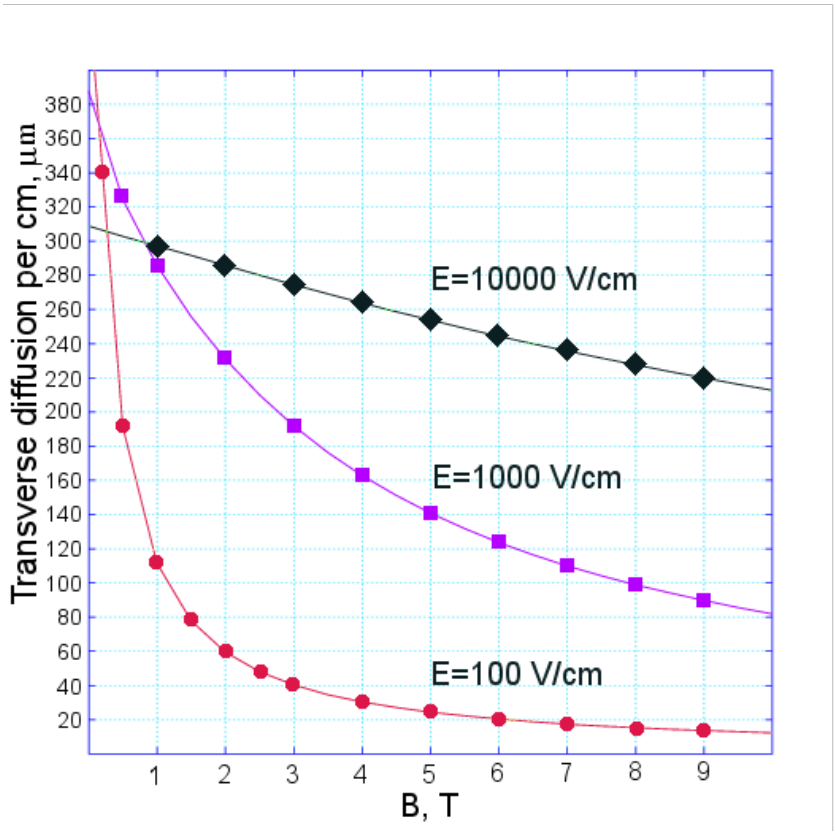

Figure 2.3: *Diffusion variation as a function of a magnetic field intensity for the gas mixture Ar/C_2H_4 80/20 for different electric field values.*

Fig. 2.4). It should be noted that both amplification principles reduce the backflow of ions by more than three orders of magnitude. Therefore, a TPC equipped with such a device can work in the continuous mode.

A very good spatial resolution, close to the theoretical limit, has been achieved during tests of the prototypes with different readout schemes. The tests have been done with the "hot" gas mixture — $Ar/CF_4/C_4H_{10}$ in the proportion 95/3/2. The spatial resolution of the prototypes with GEM and Micromegas in the 1 T magnetic field parallel to electric field lines at 5 cm from the readout plane was equal to 52 μm and 55 μm, respectively (see Figs. 2.5 and 2.6).

Further improvement of the spatial resolution is possible due to a decrease of a sensitive pad size. In the examples above pad sizes were $1.2 \times 5.4\,\mathrm{mm}^2$ for the GEM version and $3.2 \times 7\,\mathrm{mm}^2$ for the Micromegas one. It should be noted that in the latter case (Micromegas) sensitive pads were covered by a special resistive layer to spread a charge over a larger area and improve the spatial resolution. At the present time an experiment is in progress to directly detect a signal in the silicon pixel detector with a pixel size of $50 \times 50\,\mu\mathrm{m}^2$. It is anticipated that the spatial resolution in this case will be about 40 μm in the vicinity of the detection plane.

Apart from a position information, the TPC can be used for particle identification based on the energy loss in the gas medium. Indeed, at the typical pad size of 2 mm each particle crossing the chamber along the radius will produce about 70 fired pads. That should provide the $\mathrm{d}E/\mathrm{d}x$ resolution at the level of a few per cent.

Another important problem is a minimization of the chamber wall thickness, which should keep an electric potential difference at the level of a few tens of kilovolts. Such a high potential

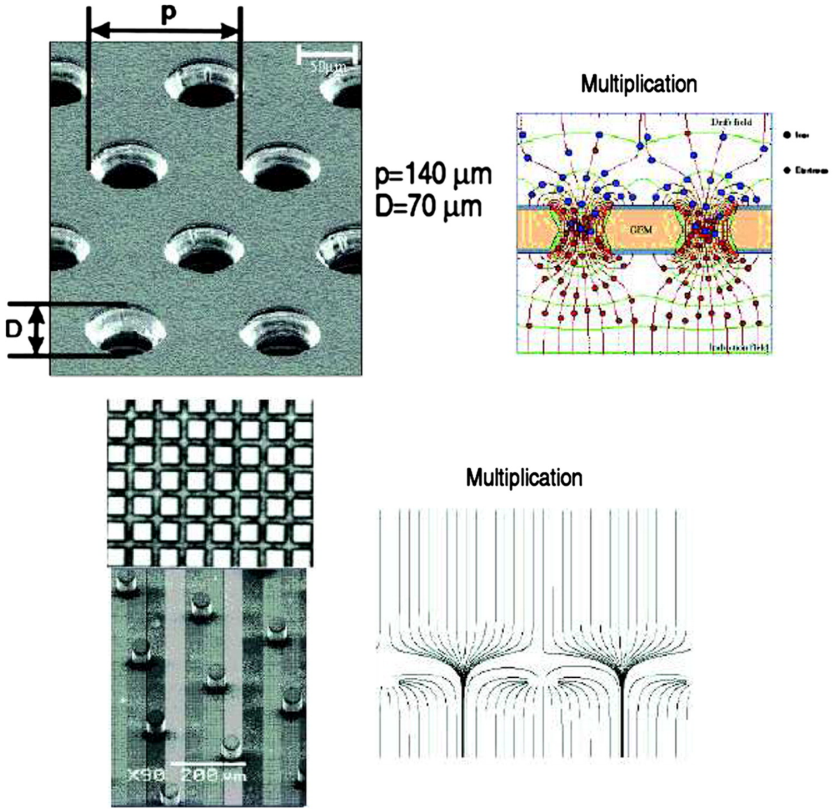

Figure 2.4: *Layout and principle of operation of GEM (upper row) and Micromegas (lower row). The figure is taken from [96].*

is required to provide the electric field tension of the order 200 – 300 V/cm, allowing an electron drift velocity of about 5 cm/μs.

At the present time a design of the detector is studied using a dedicated computer simulation.

2.4 Drift chamber

2.4.1 Introduction

The drift chamber (DCH) is the main tracking and momentum-measuring system. It provides precision momentum measurements as well as a good particle identification for low momentum tracks. The DCH design is based on the BABAR drift chamber described in detail in [102].

2.4.2 Drift chamber design

The drift chamber has conventional cylindrical design, is 2.0 m long and 1.8 m in diameter. The endplates, which carry an axial load of about 32,000 N, are made of 24 mm thick aluminum to hold plastic and metal feedthroughs for the wires. The maximum total deflection of the endplates under loading is small, about 2 mm or 28% of the 7 mm wire elongation under tension. The inner cylinder is made of 1.5 mm carbon fiber. The outer cylinder is 5 mm thick fiber glass. The inner cylindrical wall of DCH carries 40% of the wire load, while the outer wall bears 60%. To simplify its installation, this external wall was constructed of two half-cylinders with longitudinal and circumferential joints. The main structural element consists of 5 mm fiber glass. The outer shell

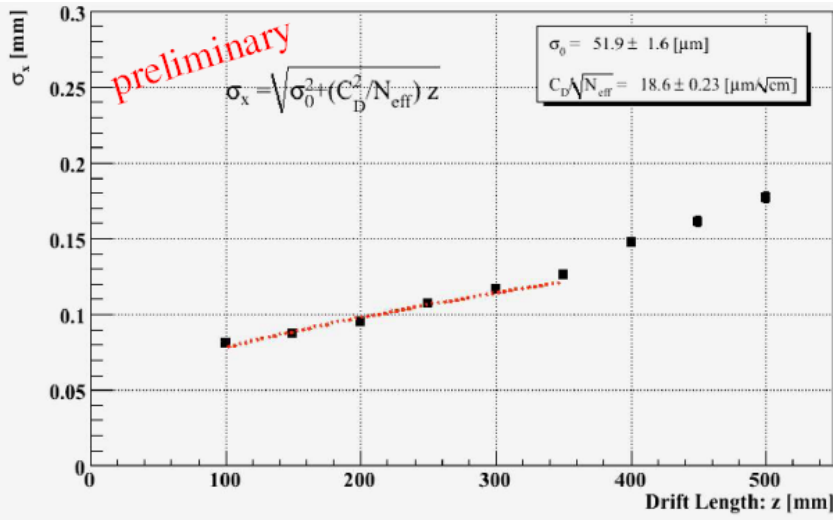

Figure 2.5: *Spatial resolution of the TPC prototype with the GEM readout.*

is capable of withstanding a differential pressure of 30 mbar and temperature variations as large as $\pm 20^o$C, conditions that could be encountered during shipping or installation. The aluminum foil, 25 μm thick on the internal surface and 100 μm on the external one, is in good electric contact with the endplates, thereby completing an RF shield for the chamber. The total thickness of DCH at normal incidence is $1.08\%X_0$, of which the wires and gas mixture contribute $0.2\%X_0$, and the inner wall — $0.28\%X_0$.

The drift system of the chamber consists of 40 layers of close-packed 7,104 small hexagonal cells, each with a single sense wire surrounded by field-shaping wires. Each hexagonal cell is approximately 1 cm in radius.

2.4.3 Drift cells

2.4.3.1 Layer arrangement

The layers are grouped by four into ten superlayers with the same wire orientation and equal numbers of cells in each layer of a superlayer. Sequential layers are staggered by half a cell. This arrangement enables local segment finding and left-right ambiguity resolution within a superlayer, even if one out of four signals is missing. The stereo angles of the superlayers alternate between axial (A) and stereo (U,V) pairs, in the order AUVAUVAUVA, as shown in Fig. 2.7.

To provide three-dimensional track reconstruction, the superlayers alternate between axial (wires parallel to the z axis) and small-angle stereo (wire endpoints offset by 7 to 12 cells, in alternate directions). The stereo angles vary between ± 32 mrad and ± 56 mrad; they have been chosen so that the drilling patterns are identical for the two endplates. The hole pattern has a 16-fold azimuthal symmetry, which is well suited to the modularity of the electronic readout and trigger system.

2.4.3.2 Cell Design and Wires

The drift cells are hexagonal in shape, 11.9 mm by approximately 19.0 mm along the radial and azimuthal directions, respectively. The hexagonal cell configuration is desirable because approximate circular symmetry can be achieved over a large portion of the cell. The choice of aspect ratio

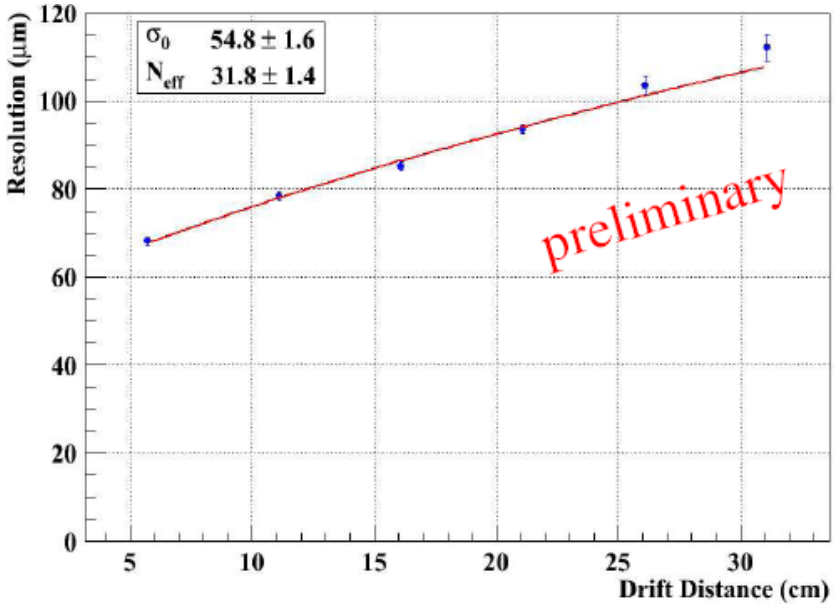

Figure 2.6: *Spatial resolution of the TPC prototype with the Micromegas readout.*

has a benefit of decreasing the number of wires and electronic channels, while allowing a 40-layer chamber in a confined radial space. Each cell consists of one sense wire surrounded by six field wires.

The sense wires are made of tungsten-rhenium alloy, 20 μm in diameter and tensioned with a weight of 30 g. The deflection due to gravity is 200 μm at midlength. Tungsten-rhenium has a substantially higher linear resistivity (290 Ω/m) compared to pure tungsten (160 Ω/m), but is considerably stronger and has better surface quality.

While the field wires are at ground potential, a positive high voltage is applied to the sense wires. An avalanche gain of approximately $5 \cdot 10^4$ is obtained at a typical operating voltage of 1960 V and a 80/20 helium/isobutane gas mixture.

The relatively low tension on the approximately 2 m-long sense wires was chosen so that the aluminum field wires have a matching gravitational sag and are tensioned well below the elastic limit. A simulation of the electrostatic forces shows that the cell configuration has no instability problems. At the nominal operating voltage of 1960 V, the wires deflect by less than 60 μm.

The tension of the field wires is 155 g to match the gravitational sag of the sense wires to within 20 μm. This tension is less than half the tensile yield strength of the aluminum wire. For cells at the inner or outer boundary of a superlayer, two guard wires are added to improve the electrostatic performance of the cell and to match the gain of the boundary cells to those of the cells in the inner layers. At the innermost boundary of layer 1 and the outermost boundary of layer 40, two clearing wires have been added per cell to collect charges created through photon conversions in the material of the walls.

A total of three different types of feed-throughs were required for the chamber to accommodate the sense, field, and clearing field wires. The three types are illustrated in Fig. 2.8. They incorporate crimp pins of a simple design which fasten and precisely locate the wires. The choice of pin material (gold-plated copper for the signal wires and gold-plated aluminum for the field wires) and wall thickness in the crimp region was optimized to provide an allowable range of almost 150 μm in crimp size as a primary means to avoid wire breakage.

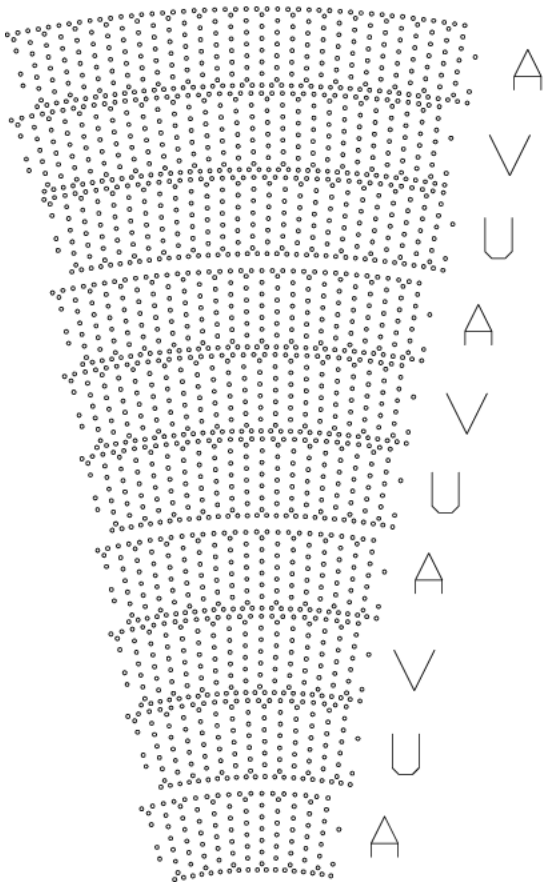

Figure 2.7: *Arrangement of drift chamber wires. One sixteenth sector of the full chamber is shown, with axial (A) and small-angle stereo (U and V) superlayers indicated.*

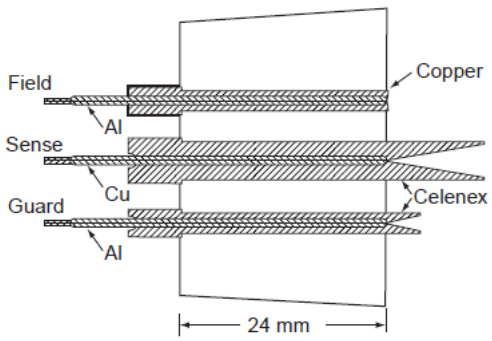

Figure 2.8: *Design of three DCH wire feedthroughs for the 24 mm-thick endplates. The copper jacketed feedthrough is for grounded field wires, the other four are for sense wires (4.5 mm diameter), and guard and clearing field wires (2.5 mm diameter), all made of a Celenex insulator surrounding the crimp pins.*

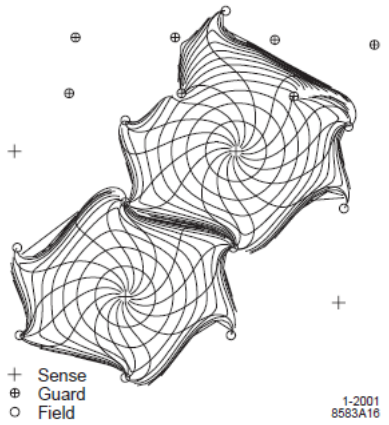

Figure 2.9: *Drift cell isochrones, i.e., contours of equal drift times of ions in cells of layers 3 and 4 of an axial superlayer. The isochrones are spaced by 100 ns. They are circular near the sense wires, but become irregular near the field wires, and extend into the gap between the superlayers.*

2.4.3.3 Drift Isochrones

The calculated isochrones and drift paths for ions in adjacent cells of layer 3 and 4 of an axial superlayer are presented in Fig. 2.9. The isochrones are circular near the sense wires, but deviate strongly from circles near the field wires. Ions originating in the gap between superlayers are collected by cells in the edge layers after a delay of several μs. These lagging ions do not affect the drift times measurements, but they contribute to the $\mathrm{d}E/\mathrm{d}x$ measurement.

2.4.3.4 Cross Talk

A signal on one sense wire produces oppositely charged signals on neighboring wires due to capacitive coupling. The cross talk is largest between adjacent cells of adjacent layers, ranging from -0.5% at a superlayer boundary to -2.7% for internal layers within the superlayers. For adjacent cells in the same layer, the cross talk ranges from -0.8 to -1.8%, while for cells separated by two layers it is less than 0.5%.

2.4.3.5 Gas system

The drift chamber is operated with a gas mixture of 80% helium and 20% isobutane, passed through a bubbler to introduce 3500 ppm of water vapor. The bubbler also introduces approximately 100 ppm of oxygen into the gas mixture, which has a small effect on the avalanche gain. The chamber is maintained at 4 mbar over atmospheric pressure with a recirculating pump; freshly mixed gas is introduced when necessary to compensate for losses.

2.4.3.6 Drift chamber performance

The performance of the BABAR drift chamber during six years of operation has been excellent. The momentum resolution is determined by reconstructing through-going cosmic ray events as two separate "tracks" and taking the difference in the fitted transverse momentum (inverse curvature in the XY plane) at the center of the chamber as a resolution. The result is

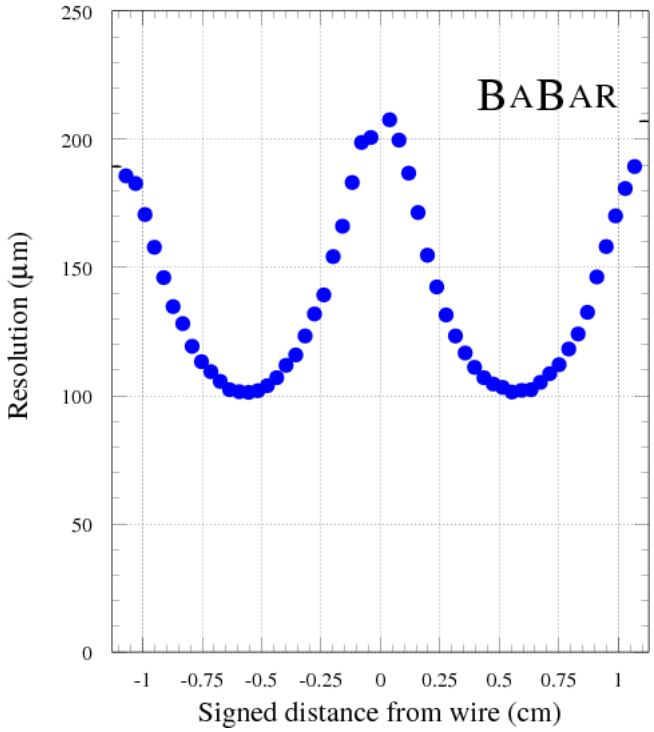

Figure 2.10: *BABAR single-hit resolution vs. distance from the sense wire. Resolution is computed from the residual of the hit position compared with the fitted track excluding that hit. The sign of the distance is positive (negative) for tracks passing to the right (left) of the radial vector to the sense wire.*

$$\frac{\sigma(p_T)}{p_T} = (0.13 \pm 0.01)\% \cdot p_T + (0.45 \pm 0.03)\%$$

The single-hit position resolution is determined for all tracks by comparing the fitted trajectory excluding each measured hit with the position of the hit determined from the readout timing and the calibration time-to-distance relation for that cell. The result (Fig. 2.10) is a weighted-average resolution of 125 μm over all cells; in the region of each cell with the most uniform electric field, the resolution is 100 μm.

The drift chamber readout system includes both timing, with 1 ns precision and integrated charge information. The detector is calibrated for the electronics gain of each channel, normalized to the charge deposition and avalanche gain as a function of the track trajectory in each layer of the chamber. With these calibrations, the integrated charge from each hit can be used to compute a relative energy loss; the $\mathrm{d}E/\mathrm{d}x$ for each track is computed from an 80% truncated mean of the hits assigned to a track, as shown in Fig. 2.11. For electrons from radiative Bhabha events $\sigma(dE/dx)/(dE/dx) \leq 7.5\%$ is obtained.

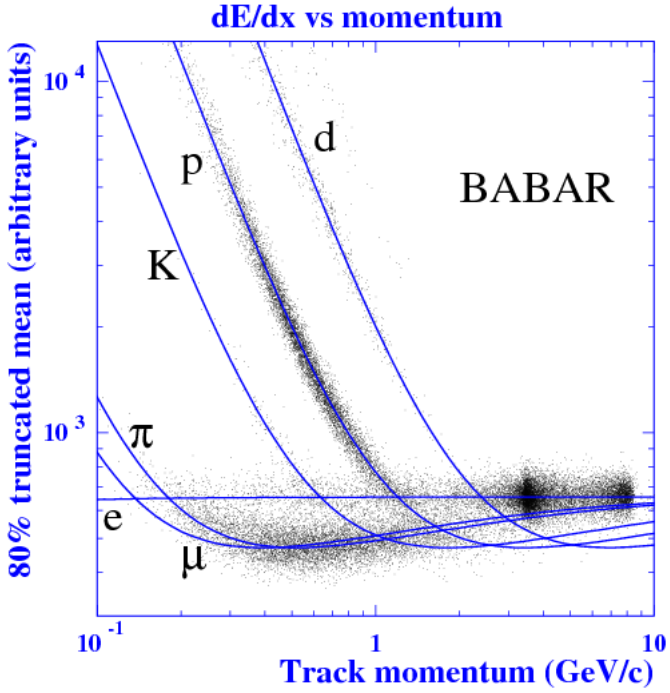

Figure 2.11: *dE/dx distribution vs momentum for particle samples.*

2.5 FARICH system

2.5.1 Introduction

An excellent particle identification (PID) for hadrons and leptons over the full momentum range for particles coming from charm and τ decay is essential to achieve the physics objectives of the experiment. In particular, a search for lepton flavor violation in the decay channel $\tau \to \mu\gamma$ with a sensitivity to the branching fraction of 10^{-9} requires a good μ/π separation around 1 GeV/c momentum. Another example is a search for CP violation in D decays that needs full particle identification to reconstruct exclusive final states and tag the flavor of the other D meson in the event.

Identification of leptons is performed by the electromagnetic calorimeter and the muon system, while energy losses in the drift chamber (dE/dx) can be used to identify charged hadrons. However, the latter technique cannot discriminate between pions and kaons with momenta above 0.7 GeV/c. Identification of muons with momenta below 1 GeV/c is a hard task for existing muon range detectors. For example, the efficiency of the BaBar detector for muons of 1 GeV/c momentum was 64% while pion misidentification rate was 2% (2.4σ separation) [103]. The KLM system of the Belle detector has a somewhat better performance with a 78% muon efficiency and 2% pion misidentification rate (2.8σ separation) at 1 GeV/c momentum [104].

For particle identification in the experiments at CTF a novel Ring Imaging Cherenkov counter with a *focusing* aerogel radiator (FARICH) is proposed. It is able to provide a high μ/π separation below and about 1 GeV/c, as well as excellent $\pi/K/p$ separation for high momenta not covered by dE/dx measurements. Section 2.5.4 reports the results of MC simulation of FARICH performance.

Silica aerogel is a porous silicon dioxide with a variable index of refraction ($1.006 \div 1.2$) that is applicable in Cherenkov detectors for particles with a few GeV/c momentum.

A first RICH detector using silica aerogel as a Cherenkov radiator was successfully employed

in the HERMES experiment [105]. It was followed by RICH1 of the LHC*b* detector [106]. Both RICH detectors use gas as a second radiator and focusing mirrors to form Cherenkov ring images on a photon detection plane.

A RICH with proximity focusing uses a gap between a layer of radiator medium and photon detector to make a ring image. This allows one to construct more compact RICH detectors as compared to RICH with focusing mirrors. Such a design was implemented in the RICH with the dual aerogel-NaF radiator for the upcoming ISS-born experiment AMS-02 [107].

2.5.2 FARICH concept

In a proximity focusing RICH, one of the main factors limiting Cherenkov angle resolution is a finite thickness of a radiator. In [108, 100, 109] it was proposed to use a radiator consisting of several layers of aerogel with different refractive indices to overcome this limitation. An index of refraction and a thickness of each layer are chosen so that rings from all layers coincide on the photon detection plane. Another possibility is to have several separate rings (Fig. 2.12). Both options allow one to diminish the photon emission point uncertainty. We call a detector employing this technique the Focusing Aerogel RICH (FARICH).

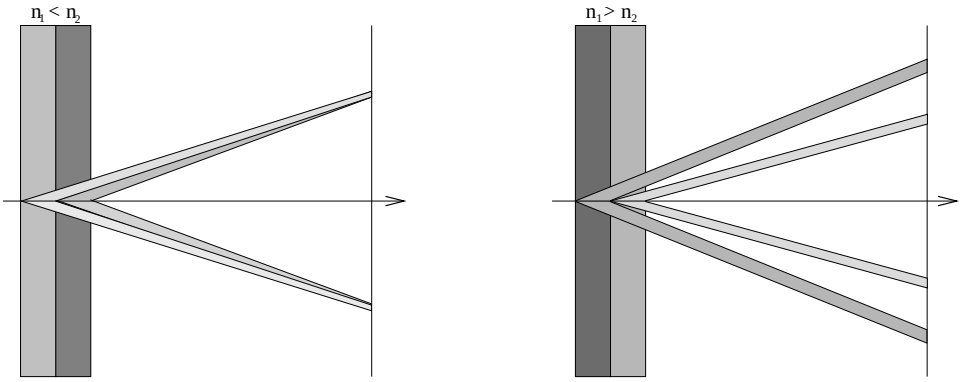

Figure 2.12: *FARICH in single-ring (left) and multi-ring (right) alternatives.*

In 2004 in Novosibirsk the first multilayer aerogel sample was obtained [100]. Four layers of that aerogel had indices of refraction and thicknesses that match designed ones with a good precision. At present, we have several aerogel tiles in a single-ring option with 2–4 layers with dimensions up to $115 \times 115 \times 40$ mm^3.

2.5.3 Design

The FARICH for CTF should cover almost a 4π solid angle and identify muons and hadrons with momenta up to approximately 2 GeV/c. The FARICH will work in the magnetic field of 1 T that imposes a serious limitation on the photon detector choice. Presently, the only existing single photon detector sensitive to visible spectrum that is able to work in a strong magnetic field of arbitrary direction is a multipixel Geiger-mode avalanche photodiode (MPGM-APD or SiPM) [110]. SiPM is almost insensitive to magnetic field, has a gain of the order 10^6, a high photon detection efficiency (PDE) in the visible region, a low voltage bias and a size of a few mm. A main disadvantage of SiPMs is a high dark counting rate at the room temperature ($\sim$ 1 MHz/mm^2). These devices are readily available from a number of Russian and foreign

producers: CPTA (Moscow), MEPhi/Pulsar (Moscow), Hamamatsu Photonics (Japan), Zecotek (Canada-Singapore), FBK-irst (Italy) etc.

The suggested FARICH layout is shown in Fig. 2.13. It consists of the barrel and endcap parts. A solid angle of the system is 98% of 4π. The radiator has the area of 17 m^2, photon detectors — 21 m^2. The number of SiPMs and electronics channels is about one million.

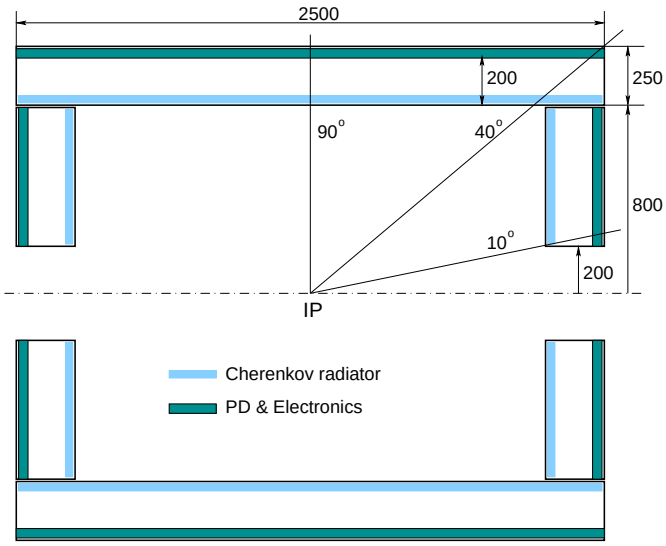

Figure 2.13: *FARICH PID system for the Super $c\tau$ factory.*

The very large number of channels and their high density will require a development of dedicated front-end electronics based on ASICs. The digitizing part (TDC) should be located right in the detector.

2.5.4 MC performance

The following configuration of the FARICH is considered and studied using a Geant4-based Monte Carlo simulation program:

- a distance between the radiator and photon detector — 200 mm,
- a single-ring four-layer aerogel radiator with a total thickness of 35 mm and $n_{\max} = 1.07$,
- a photon detector — MPPC (Hamamatsu Photonics) with a 3×3 mm^2 active area, PDE(500nm)=30%, packing density — 53%.

Simulation takes into account the processes of radiation, absorption and scattering of the Cherenkov light. Interactions of charged particles with matter were proved to be negligible (except for multiple scattering at momenta below 0.5 GeV/c) and not simulated. A magnetic field of 1 T is included in simulation. Effects of the SiPM dark noise and detector background are currently not taken into account.

Simulation shows that the number of photoelectrons for a relativistic particle is about 25 (Fig. 2.14a) that is enough for a robust ring reconstruction. The velocity resolution reaches $5 \cdot 10^{-4}$ (Fig. 2.14b). Figures 2.14c,d demonstrate π/K and μ/π separation levels derived from the velocity resolution. π/K separation is very good beginning from the kaon Cherenkov threshold in aerogel (1.3 GeV/c) and up to a few GeV/c momenta. In real situation the π/K separation

will be determined by other processes such as kaon decays, noises of photon detectors, detector backgrounds etc. μ/π separation is possible at the level $\geq 3\sigma$ from 0.4 to 1.7 GeV/c and is 5.5 to 8 σ at 1 GeV/c momentum.

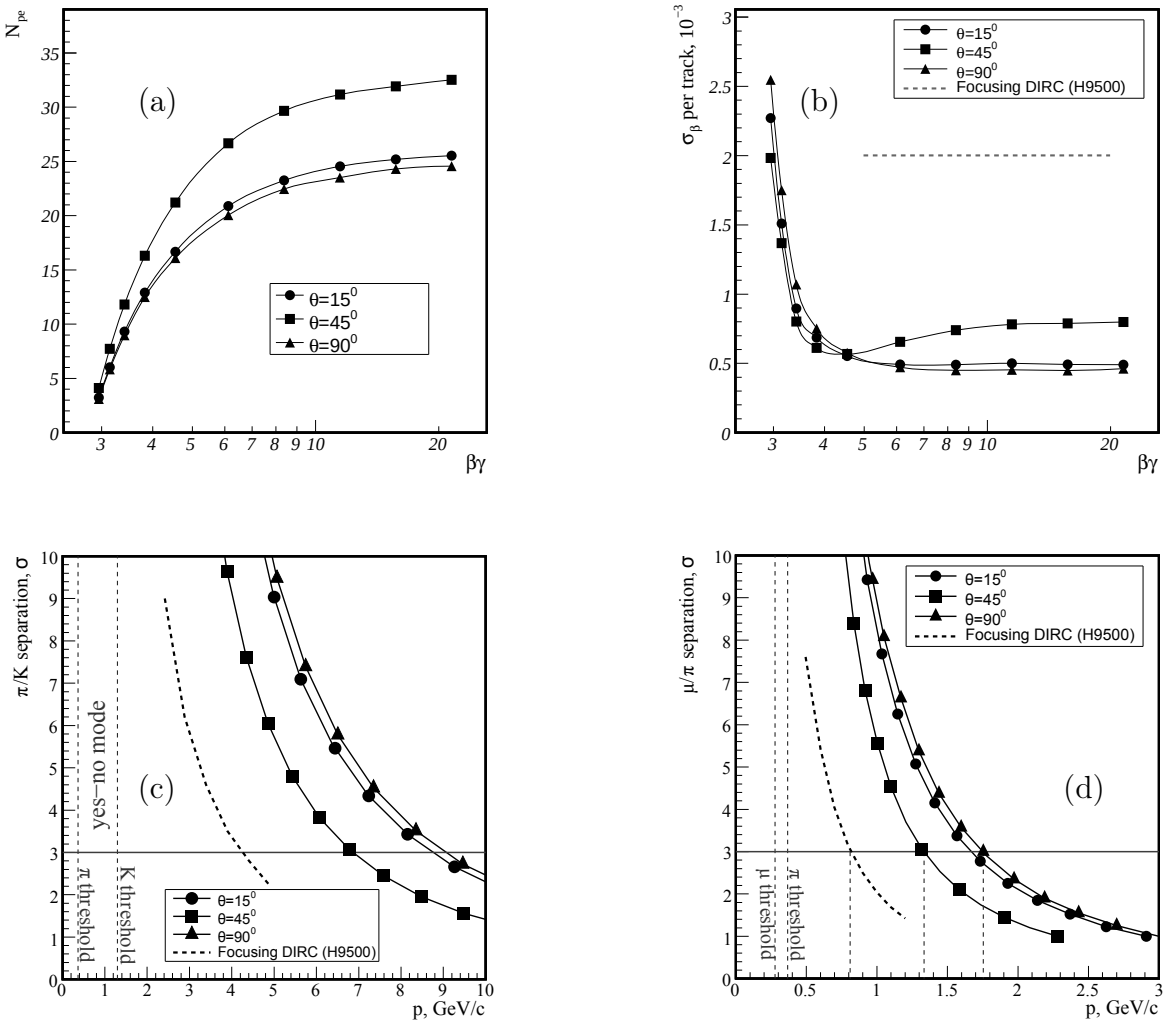

Figure 2.14: *FARICH simulation results for three polar angles: the number of photoelectrons (a), velocity resolution (b), π/K (c) and μ/π (d) separations. Focusing DIRC performance is shown for comparison.*

The development of DIRC upgrade with a focusing mirror and chromaticity correction is ongoing at SLAC [111]. π/K separation of the Focusing DIRC is shown along with the FARICH performance in Fig. 2.14c. We calculated from these data the corresponding velocity resolution that is $\sim 2 \cdot 10^{-3}$ (Fig. 2.14b) and μ/π separation (Fig. 2.14d) that amounts to 2σ at 1 GeV/c momentum.

Methods of coverage of lower momenta is currently discussed and can be either a threshold mode of operation ("yes-no mode") or an employment of an additional radiator of higher index of refraction such as crystal NaF ($n = 1.33$). Both approaches demand reducing the effect of the SiPM dark noise. It is possible with a high timing resolution of the order 100 ps, but would require an application of rather complicated and expensive electronics with a high power consumption.

Another possibility is to cool down photon detectors to the temperatures that decrease the dark counting rate below 1 MHz/channel. A development of an efficient cooling system with low material budget is needed in this case.

2.5.5 Status of prototype development

Presently, the prototype of the FARICH is being constructed. It will be tested at the electron beam with energy $\sim$ 1 GeV at the ROKK-1M facility at the VEPP-4M collider. It is planned to measure single-photon Cherenkov angle resolution and number of photoelectrons for several focusing aerogel tiles and compare the results with simulation. Also a possibility to read out and reject the high SiPM noise rate will be tested.

In the prototype 32 MRS APDs 2.1×2.1 mm^2 from CPTA company, custom made 16-channel discriminator boards with built-in preamplifiers and multi-hit 64-channel TDC from CAEN with 100 ps discrete are used. The first run of the beam test is scheduled for November 2010–February 2011.

2.6 Electromagnetic calorimeter

An electromagnetic calorimeter of the CTF detector has the following functions:

- detection of γ–quanta and measurement of their energy in the broad energy range from 1 MeV to 2 GeV;
- determination of photon coordinates;
- separation of electrons and hadrons;
- formation of a signal for a neutral trigger.

In these experiments the main fraction of photons arising in hadron decays has energy of a few hundred MeV. Therefore, an important characteristic of a calorimeter is energy resolution in this energy region. At the present time the best energy resolution for photons with energy up to 1 GeV is obtained at calorimeters based on scintillation crystals CsI(Tl) [112, 102], $\sigma_E/E \approx 1.8\%$ at 1 GeV and about 3% at 100 MeV. Space resolution of such calorimeters is about $6\,\mathrm{mm}/\sqrt{E(\mathrm{GeV})}$. It is also worth noting that Budker Institute has big a experience of working with calorimeters based on scintillation alkali-halide crystals.

One more advantage of scintillation calorimeters is their high stability and low maintenance costs. CsI(Tl) crystals have a high light output (up to 50,000 photons/MeV) and emission spectrum with a maximum at about 550 nm well matching the region of high sensitivity of silicon photodetectors.

Maintenance of CsI(Tl) crystals in the B factory experiments showed that their radiation hardness is sufficiently high for conditions of e^+e^- colliders. For example, at the Belle detector the total absorbed dose for crystals closest to the beampipe is about 300 rad during 7 years of operation. At CTF with luminosity of $10^{35}\,\mathrm{cm}^{-2}\mathrm{s}^{-1}$, the absorption dose can reach about 1 krad after 5 years of experiments that results in about 20% loss of the light output only.

However, the emission time for such crystals is about 1 μs that can lead to a high probability of the pile-up of a background and useful signals at high background counting rates (about 100 kHz or more per crystal). A natural solution of this problem is to use faster crystals of non-activated (pure) CsI with the emission time of about 30 ns. Note, however, that the light output of these

crystals is one order of magnitude lower than that of CsI(Tl) crystals necessitating use of vacuum photodetectors with gain, capable of operating in magnetic field. Thus, taking into account a higher cost of pure CsI crystals, a calorimeter based on such crystals is more expensive and have a more complicated structure. A reasonable trade-off is to use pure CsI in the calorimeter endcaps, where the background counting rate is high, and Cs(Tl) crystals in the barrel part where the background is one order of magnitude lower.

A length of the crystals and, correspondingly, a thickness of the active material is selected in such a way that about 95% of photon energy is absorbed in the calorimeter. A length necessary to reach good energy resolution is 16–18 radiation lengths or 26–34 cm. A transverse size of the crystals is determined by a transverse size of an EM shower and is usually chosen between 4 and 7 cm. A lower transverse size improves position resolution, but increases the number of electronics channels and the total number of gaps between the crystals. The total number of crystals in the calorimeter and its total mass depend on the specific detector design, but as experience of operation of existing calorimeters shows, the total mass of crystals should be 42 tons at the total number of calorimeter channels of about 10 thousand.

Note that in recent years new crystal scintillators with high light output and short emission time have been actively developed, e.g., lutecium ortosilicate (LSO) and lantane bromide ($LaBr_3$) activated by cerium. Despite their high promise, the cost of such crystals is rather high (5–10 times more expensive than CsI(Tl)) making the mass use of these crystals problematic. At the same time, active R&D studies of new crystals and their use in high energy physics in close cooperation with crystal producers can improve technology of their growth and make it cheaper as it happened in the past with NaI and CsI crystals.

2.7 Muon system

The muon system consists of nine layers of coordinate detectors in the barrel and eight layers at the endcap. The barrel part covers a solid angle of $63\% \times 4\pi$ ($50^\circ < \Theta < 130^\circ$), while the endcap — $27\% \times 4\pi (20^\circ < \Theta < 50^\circ$ and $130^\circ < \Theta < 160^\circ$). Coordinate detectors are alternated with layers of a steel absorber, which also serves as the yoke of the magnet.

The main task of the muon system is to separate muons from a large number of hadrons produced in events of e^+e^- annihilation. Muons are identified by measuring their penetration depth (range) in the absorber. The ranges of muons and hadrons in matter are determined by two main processes: energy loss of a charged particle through ionization and nuclear interactions of hadrons with atoms of the absorber. At the same momentum muons have larger kinetic energy compared to pions and kaons, so they could lose more energy on ionization and their path is longer. Nuclear interactions of hadrons with the medium lead to additional absorption and further decrease of their range.

Due to bending of the particle track in the magnetic field of the detector, the detection threshold of the muon system is at the momentum of 0.4–0.5 GeV/c. In reality, it is difficult to obtain reliable identification of muons at the momenta below 0.8 GeV/c. A pion can imitate a muon due to range fluctuations and as a result of the decay into muon and neutrino, particularly when a decay muon is emitted in the direction of the initial pion. Above 0.8 GeV/c the muon detection efficiency reaches 95–98 % and the level of pion misidentification is $\sim$5%, this corresponds to a pion suppression factor of $\sim$20. To achieve the main goals of the research program of CTF the pion suppression at the level of 100 or better is desirable. To attain it, the muon system will work in combination with the FARICH identification system. The information from the FARICH can be also used to calibrate the muon system.

In modern experiments, coordinate detectors of different types are used in muon systems: counters with the localized discharge [113], streamer mode gas detectors [114], scintillation counters [115]. The choice of the detection technology of coordinate chambers requires a study of their long-term stability and resistance to the backgrounds under the experimental conditions of CTF. One should also take into account the cost of the production of detectors. The total area of the coordinate detectors is more than 1000 m^2.

Currently, as a "working" option of the coordinate detectors for the muon system it is proposed to use coordinate detectors similar to the streamer tubes used in the KEDR detector [116]. Streamer tubes in a single block are arranged in two layers and are shifted relative to each other by half of the diameter. With this arrangement, a particle track always crosses one or more tubes at any incidence angle. Tubes of one electronic channel are connected sequentially in a row and alternated by the other channel tubes to reduce a probability of simultaneous triggering of several tubes in one channel or several channels by a single particle.

The basis of the block are two flanges made of duraluminum holding thin-wall stainless steel tubes. At the ends of the tubes kapronit made plugs with two holes are pressed. One hole in the center is for pin fixation, the second — for a gas inlet or outlet. In the center of the tube an anode wire is stretched with a force of 300 g and fixed in pins. The wire material is gold-plated molybdenum with a diameter of 100 μm.

The scheme of the readout electronics of one channel is shown in Fig. 2.15. A measurement of the longitudinal coordinate is based on the difference between the arrival times of signals on the opposite ends of the tube row. Two amplifiers with variable threshold discriminators are connected to both ends of the row. To prevent reflections at the ends of the row, the load resistors are used. The "start" and "stop" signals from both discriminators are transmitted to the expander. The "stop" signal is delayed in such a way that it always comes later than "start" regardless of the particle coordinate in a row. The expander gives a paraphase signal with the duration equal to the difference of arrival times of "start" and "stop" signals multiplied by a coefficient of expansion about 40. Signals from the outputs of expanders are transmitted via a shielded twisted-pair cable to the inputs of TDCs.

The duration of the output pulse from the expander depends on a particle hit location. Reconstruction of the hit longitudinal coordinate is done using a linear approximation taking into account the length of the wires connecting the tubes. The transverse coordinate is determined from the number of the tube. A more accurate measurement of the transverse coordinate using a drift time of ionization is possible but not necessary because of the strong multiple scattering in the absorber.

To operate in the streamer mode, a gas mixture should contain a component with strong photon absorption in the UV spectrum. The working gas in the muon system is a nonexplosive mixture of 70%Ar : 23%CO_2 : 7%n-pentane.

The average resolution of the longitudinal coordinate is about 4 cm which is sufficient for the tasks of detection.

2.8 Superconducting solenoid

2.8.1 Main demands

The superconducting solenoid is intended to produce axial magnetic field in the volume of the detector. It will be placed outside the CsI calorimeter. Outside the solenoid the muon system will be placed. The solenoid placement does not demand that the thickness of the solenoid should be

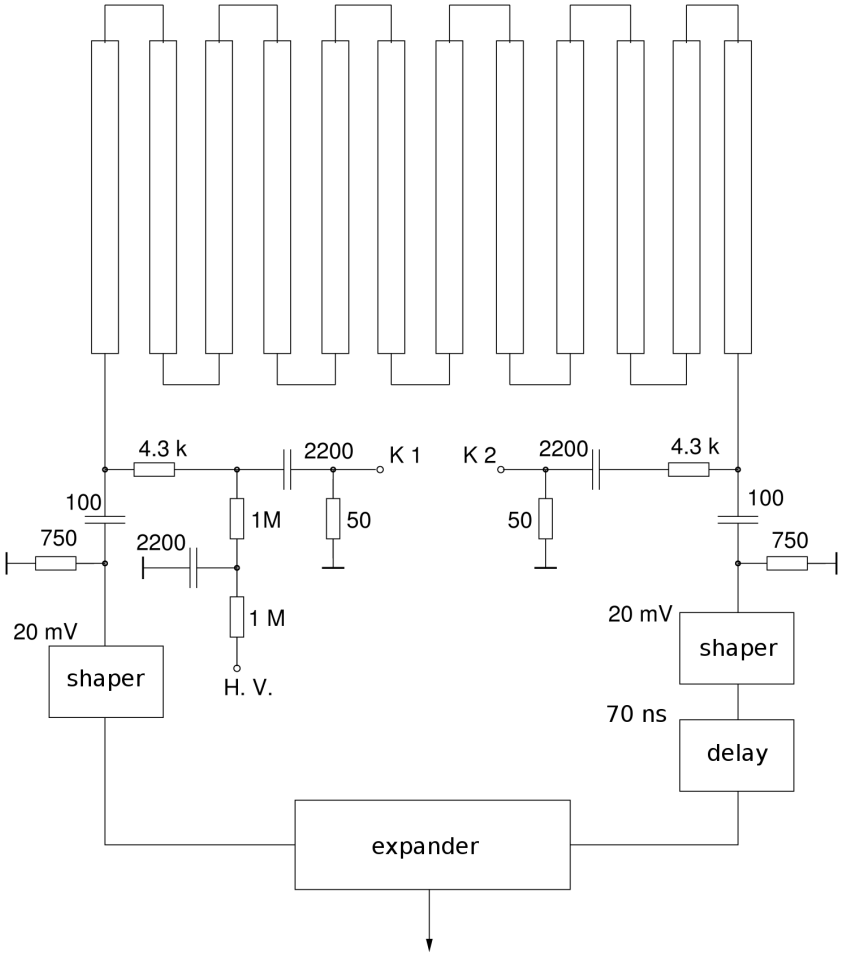

Figure 2.15: *Readout electronics of the muon system.*

Table 2.1: *Main established parameters of the solenoid.*

Length, m	4
Internal diameter, m	3.2
Magnetic field, T	1
Stored energy, MJ	12.9
Charging time, h	< 4

as thin as possible like in other detector solenoids.

The main parameters of the solenoid are listed in the Tab. 2.1.

The cost of a detector solenoid is estimated at 3.3 M$.

2.8.2 Original approach

The similar superconducting solenoids were produced in the last decade by Japanese and European companies. For their production a technology based on superconducting cable with aluminum stabilizer was developed.

The stabilizer made of 99.999% Al is very expensive material. It costs $1000 per kg, so most percentage of the solenoid cost relies on this stabilizer. The main purpose of the stabilizer in the solenoid design is a quench protection. The stabilizer does drastically minimize a heat generation inside the solenoid, i.e. ρJ^2, where J — current density, ρ — electrical resistivity of the stabilizer. This circumstance was considered from three following points of view:

1. the electrical and thermal properties of 99.999% Al and 99.99% Al differ by factors from 2 to 5, while the cost of the second Al is by a factor of > 100 less;

2. the heat generation can be also minimized by increasing the amount of the stabilizer;

3. active quench protection is used in the modern solenoids of the LHC projects.

So, the solenoid design for the Super $c\tau$ factory is considered to use the superconducting cable with aluminum stabilizer based on 99.99% Al. Active quench protection using heaters will be used for quench propagation. The proposed approach allows to save about $1–2 millions for the solenoid production.

Preliminary calculations show that the size of superconducting cable can be the same as for the ATLAS central solenoid, as shown on the Fig. 2.16. This cable was produced by Hitachi Co, Japan.

2.8.3 Cryogenics

The cryogenics of the detector should provide the operation of the detector solenoid and the final focus quadrupoles of the collider at the temperature of 4.5 K. The cryogenics will be based on a refrigerator of 100 W of cooling performance at 4.5 K.

The capital cost of the refrigerator is estimated at 0.5 M$.

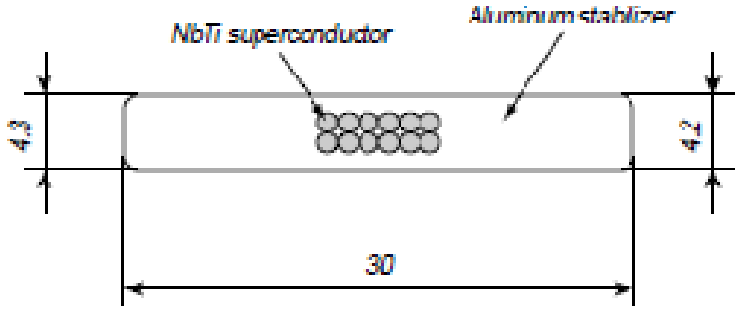

Figure 2.16: *SC cable used in the ATLAS central solenoid. Its sizes satisfy the sizes of the cable for the CTD solenoid.*

Table 2.2: *The luminosity, physical cross section, rates of useful events, Bhabha events at different energies, rates from cosmic events.*

	J/ψ	$\psi(2S)$	$\tau\bar{\tau}$	$\psi(3770)$	$\tau\bar{\tau}$	$\Lambda_c\bar{\Lambda}_c$
$E_{\rm cm}$, MeV	3097	3686	3700	3770	4250	4650
L, $10^{34}{\rm cm}^{-2}{\rm s}^{-1}$	7.7	9.2	9.2	9.4	10	10
σ, nb	$\sim$3400	$\sim$640	2.5	$\sim$6	3.5	0.5
f, kHz	260	60	2.3	5.6	3.5	0.5
Bhabha, kHz	$\sim$90	$\sim$80	$\sim$80	$\sim$80	$\sim$60	$\sim$50
Cosmics, kHz	$\sim$2					

2.9 Trigger

Trigger of the CTF detector will be based on the concept of the "open-trigger", which can select and save up to 100% of useful events. This concept implies that event selection is based on the universal criteria such as: the presence and the topology of the tracks in the coordinate system, the total energy deposition in the calorimeter, the topology of the energy deposition and the number of clusters in the calorimeter, the response of the muon system. "Open trigger" is not specially tuned for the selection of the particular predefined processes. This approach is conditioned by a very wide and diverse physics program of CTF and the task of finding "new physics" that is impossible to predict in advance. A disadvantage of this approach is that it is impossible to separate useful events from the events of nonresonant hadron production based on the trigger.

Useful event rates and rates of Bhabha events at different energies as well as rates from cosmic events are presented in Table 2.2. The cross section of the nonresonant hadron production at these energies is $\sim$20 nb, which corresponds to the counting rate of 20 kHz at the luminosity of $10^{35}{\rm cm}^{-2}{\rm c}^{-1}$. At present it is difficult to estimate the trigger counting rate from the background events associated with the beam loss and beam interaction with the residual gas. Working conditions at the B factories at KEK and SLAC and current development of the Super$B$ factory in Italy indicate that this counting rate will be at the level of several tens of kHz.

As follows from the data above, the maximum readout rate of useful events will reach 300–400 kHz. The average size of a single event is estimated at 30 kB.

To achieve so high event readout, it is expected to use the methods and approaches developed

at the BABAR detector and for the Super$B$ project.

- All signals from the detector systems are continuously digitized in the electronics located directly on the detectors. The data are stored in digital pipelines for a few microseconds. The storage time is determined by the decision making time of the first level trigger.

- The electronics of the drift chamber, calorimeter and muon system give an additional "fast" signals, which are transmitted directly to the first level trigger.

- After receiving the signal from the first level trigger, data from the onboard electronics are transmitted over the high-speed optical links (10 Gbps) into the readout processors (ROP), which are located outside the detector. The preprocessing is performed in the ROPs (actual signal amplitudes and times are computed) in order to reduce the amount of data. An additional filtering based on the topology and timing information is also performed at this stage.

- Data from the ROPs of each system come into the "event builder" computer farm where they are synchronized and then processed by the high level trigger.

- The first level trigger for a search of "useful" events uses "fast" signals from the detector systems. It is based on a specialized pipelined processor with the programmed logic of the event search. This logic uses the topology of tracks in the coordinate system, the total energy deposition, the topology of energy deposition and the number of clusters in the calorimeter as well as data from the muon system. The maximum frequency of the decision making is 500 kHz, the effective "dead time" of the primary trigger should not exceed 100 ns. The decision making time of the first level trigger is a few microseconds.

- The high level trigger is software based. The fast preliminary reconstruction of the events to get information about the coordinate, momentum and energy of all secondary particles is performed. At this stage, the effective rejection of the background events from the beam interactions and cosmics is done. To reduce the amount of the recorded information, prescaling of the Bhabha scattering events could be implemented. The high level trigger will be organized on the basis of a specialized computer "farm", consisting of several hundred processors.

2.10 Electronics

Electronics together with computers and telecommunication equipment of the detector is one of the key elements of the CTF detector.

Collider parameters, which are important for the electronics, are below.

- The RF frequency is about 508 MHz.

- The period of bunch circulation is 2.557 μs.

- The quantity of separatrixes is 1300.

- Each third separatrix is filled, so the time gap between bunches is around 6 ns.

- The mode with filling each fourth separatrix is under discussions.

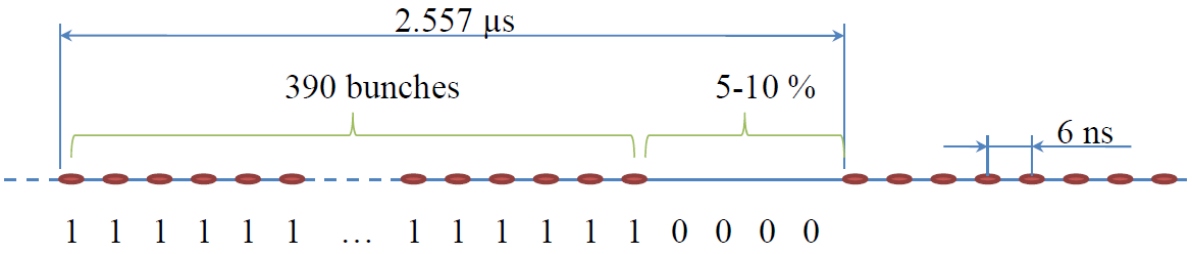

Figure 2.17: *The bunch distribution and binary map.*

Table 2.3: *Limitations and demands of the susbsystems' electronics.*

Detector	Channel quantity	Channel size	Power consumption	Trigger participation	Information
VD–GEM	56 K	$2 \times 2\,\mathrm{mm}^2$	1 kW	Possible	A, T, P
VD–Pixel	10 M	$150 \times 150\,\mu\mathrm{m}^2$			
DC	7.1 K	$12 \times 20\,\mathrm{mm}^2$	2 kW	Yes	A, T, P
FARICH	1 M	$4.5 \times 4.5 \times 50\,\mathrm{mm}^3$	100 kW (21 m^2)	No	T, P
Calorimeter	7.5 K	$(40-70)^2\,\mathrm{mm}^2$	2 kW	Yes	A, T, P
Mu	4–44 K	diameter 20 mm	1–9 kW	Yes	T, P

- The maximum quantity of bunches is 390.
- The gap of 5–10% (130 separatrixes) in a bunch train is necessary for suppression of the ion instability.

For a precise time measurement of several detector subsystems it will be necessary to know the bunch distribution in a train. Therefore, the binary map of the bunches will be used (Fig. 2.17). The synchronizing pulse "phase" for the bunch circulation will be also necessary.

All analog-to-digit conversions will be performed inside the detector in front–end (FE) electronics. The information from a large group of channels will be sent through 10 Gbps optical links. Wide usage of ASICs is mandatory to reach a needed channel compactness and power consumption. The water cooling system with a negative pressure for the front-end electronics will be applied. The electronics should employ a maximum unification.

Table 2.3 lists the quantity of electronics channels for different subsystems of the detector, the geometrical size of channels, an estimate of the power consumption, participation of subsystems in the trigger and a type of required information (A — amplitude, T — time, P — position).

Table 2.4 shows the maximal channel load, the time characteristics of the pulses, the required rates of digitization, the bit quantity of ADC and TDC and the necessary precision of time measurements.

Figure 2.18 shows the common block diagram of readout electronics. The FE electronics contains amplifiers, ADC and TDC, an obligatory pipeline for the working time of the L1 trigger, controller, which manages a board and optical transmitters, 10 Gbps optical links connecting the FE electronics and readout processors (ROP), which are located near the detector. ROPs get raw data and perform calculations of the amplitude and time of pulse. Additional selection of

Table 2.4: *Parameters of subsystems' electronics.*

Detector	Channel load	Duration of signals	Rate of digitization	Bit quantity of ADC (TDC)	Time meas. precision
VD	33 kHz	Rising edge 25 ns	from 20 MHz to 80 MHz	10–12 bit ADC	1 ns
DC	50 kHz	Rising edge	50 MHz (ordinary mode)	10 bit ADC	1 ns
		100–200 ns, Follow	200–300 MHz (cluster	10 bit ADC	1 ns
		edge 300 ns	mode)		
FARICH	10 MHz	5–10 ns	TDC	6 bits (for 8 ns) TDC	200 ps
Calorimeter	15 kHz	30 ns for clear CsI	40–50 MHz	18 bit ADC	1 ns
Mu	100 kHz	30–200 ns	TDC	11–12 bit ADC	60 ps

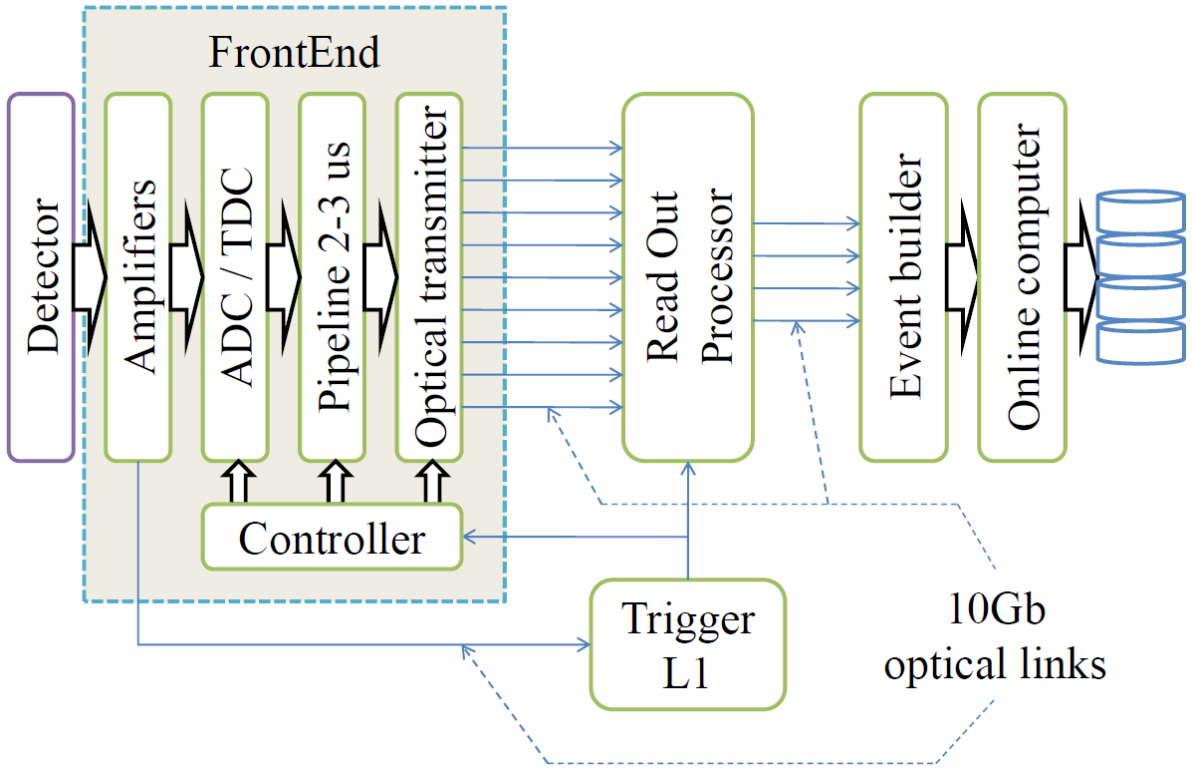

Figure 2.18: *A block diagram of electronics.*

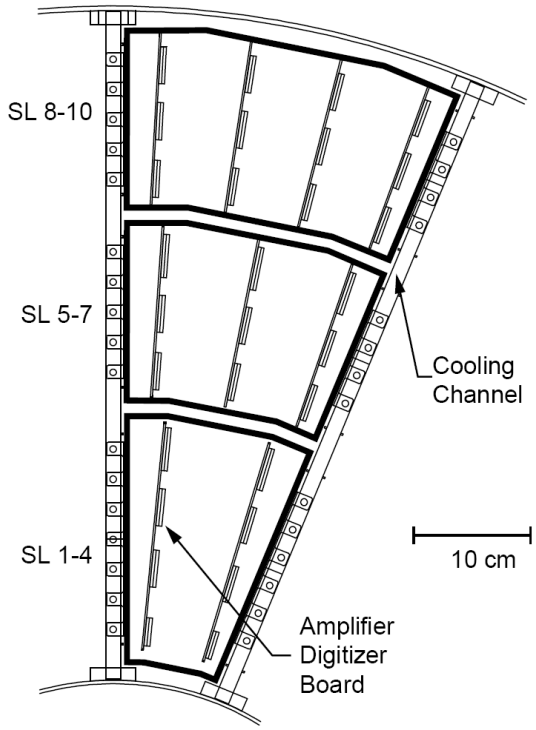

Figure 2.19: *FrontEnd Assembly of the drift chamber of BABAR.*

information based on L1 trigger data is possible in ROPs. Results are sent to EventBuilders and on-line computers located in the data storage hall.

The L1 trigger is located near the detector. It gets fast information from FE electronics by 10 Gbps optical links.

It is planned to make a modular FE electronics in order to enable fast replacement of a broken element. This approach has been successfully working in the drift chamber of BABAR (Fig. 2.19 and Fig. 2.20). All electronics is divided into 16 sectors in φ and 3 rings in radius. Therefore there are 48 assemblies of the FE electronics. All boards of an assembly are placed into aluminum frame, which serves not only as a shield but also as a heat sink. All microchips have thermal contact with a frame. The assemblies are firmly screwed to the radial bars that carry water cooling. The total power of about 1.5 kW is removed from the detector.

The drift chamber FE electronics (Fig. 2.21) will have 48 modules of 3 types. Each module will have from 128 to 192 channels, from 2 to 4 FE boards and one readout board. The FE board will contain from 48 to 64 channels of amplifiers and ADCs. The readout board will hold a common pipeline and controller in FPGA which will send information to a ROP upon a signal arrival from the L1 trigger.

Table 2.5 was created after estimating the data flows from the detector subsystems and convenience of mounting. It shows the supposed quantity of optical links for data and trigger information. The quantity of 10 Gbps links is redundant for all subsystems except FARICH. In total, there are 1168 data links and 168 trigger links.

The ROP gets data via 8 optical links (Fig. 2.22). Therefore 146 ROPs will be necessary for 1168 data links. This unit calculates the amplitude and time of pulses from raw data of the FE electronics. It uses L1 trigger information to process so called "field of interests" — the places of the detector where the channels are triggered. This approach reduces the processing time and

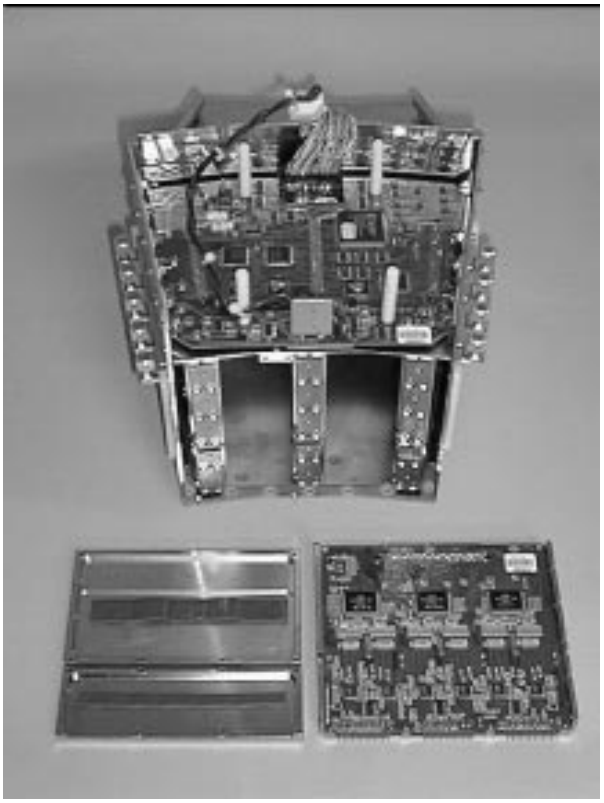

Figure 2.20: *Photo of FrontEnd Assembly of the BABAR drift chamber.*

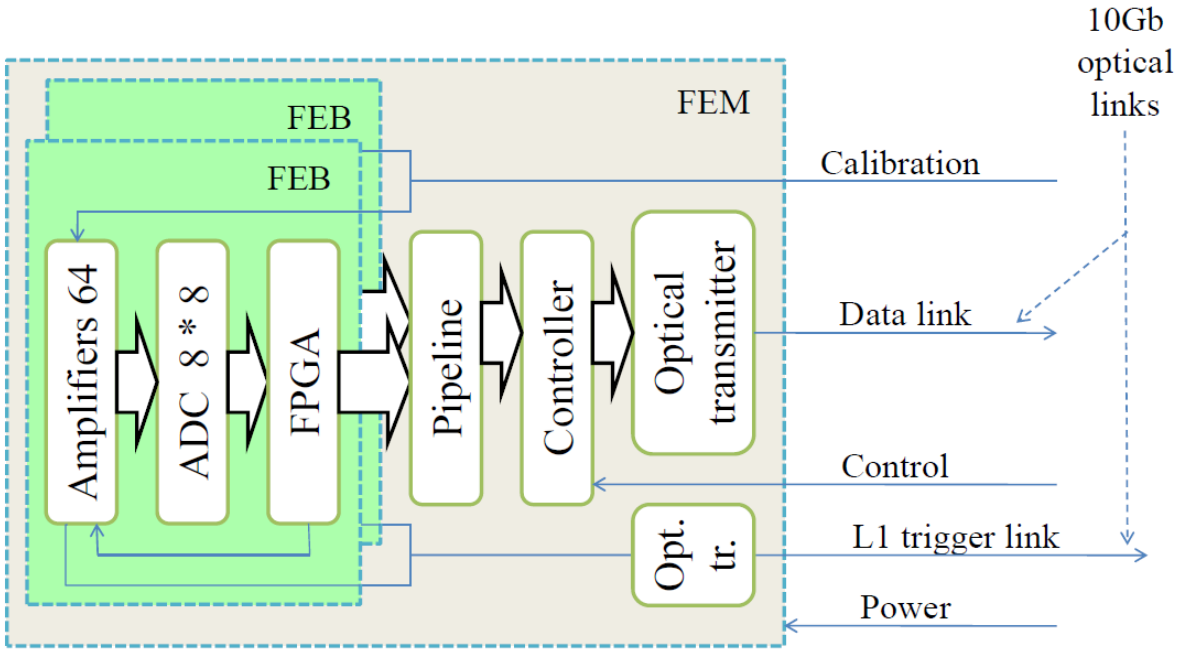

Figure 2.21: *A block diagram of the drift chamber FE module.*

Table 2.5: *Number of electronics channels, data and trigger links.*

Detector	Number of channels	Number of data links	Number of trigger links
VD–GEM	56 K	56	56
VD–Pixel	10 M		
DC	7.1 K	48	48
FARICH	1 M	1000	0
Calorimeter	7.5 K	32	32
Mu	4 – 44 K	32	32

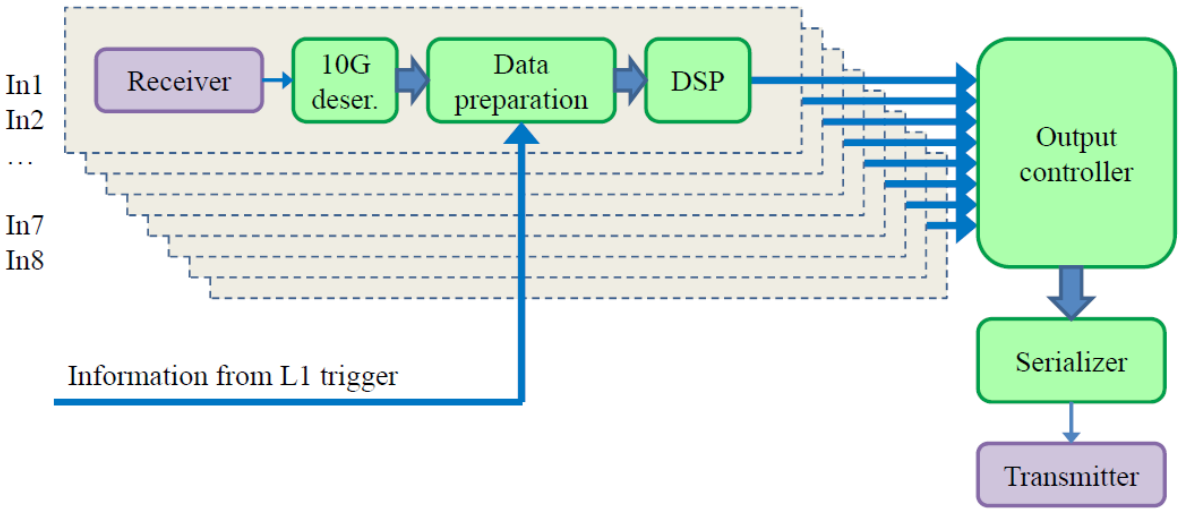

Figure 2.22: *A block diagram of the ReadOut processor.*

amount of the output data.

146 ROPs will occupy 10 VME crates, which will be located in 5 racks. The preliminary power consumption of one crate is about 900 W, so one rack will consume 1.8–2.7 kW. The racks with ROPs will be located near the detector (Fig. 2.23).

The L1 trigger has a pipelined structure. It gets information from the drift chamber, CsI calorimeter, muon system and possibly from the vertex detector (Fig. 2.24). Preprocessors of the tracking systems calculate the number of tracks and their topology. Preprocessors of the calorimeter determine the topology and number of clusters and energy level. Also the information of triggering the muon system is present. Preprocessors transfer the information to the central trigger processor which makes a decision.

The L1 trigger decision pulse goes to the FE electronics. The fields of interests are transferred to ROPs. And the intermediate information about the trigger is transmitted to the Data Acquisition system. The L1 trigger will occupy two racks that will be located near the detector together with ROP racks.

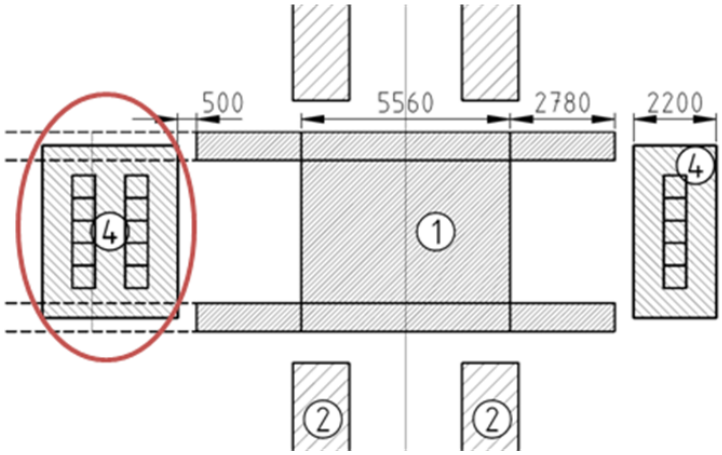

Figure 2.23: *The location of racks with ROPs near the detector.*

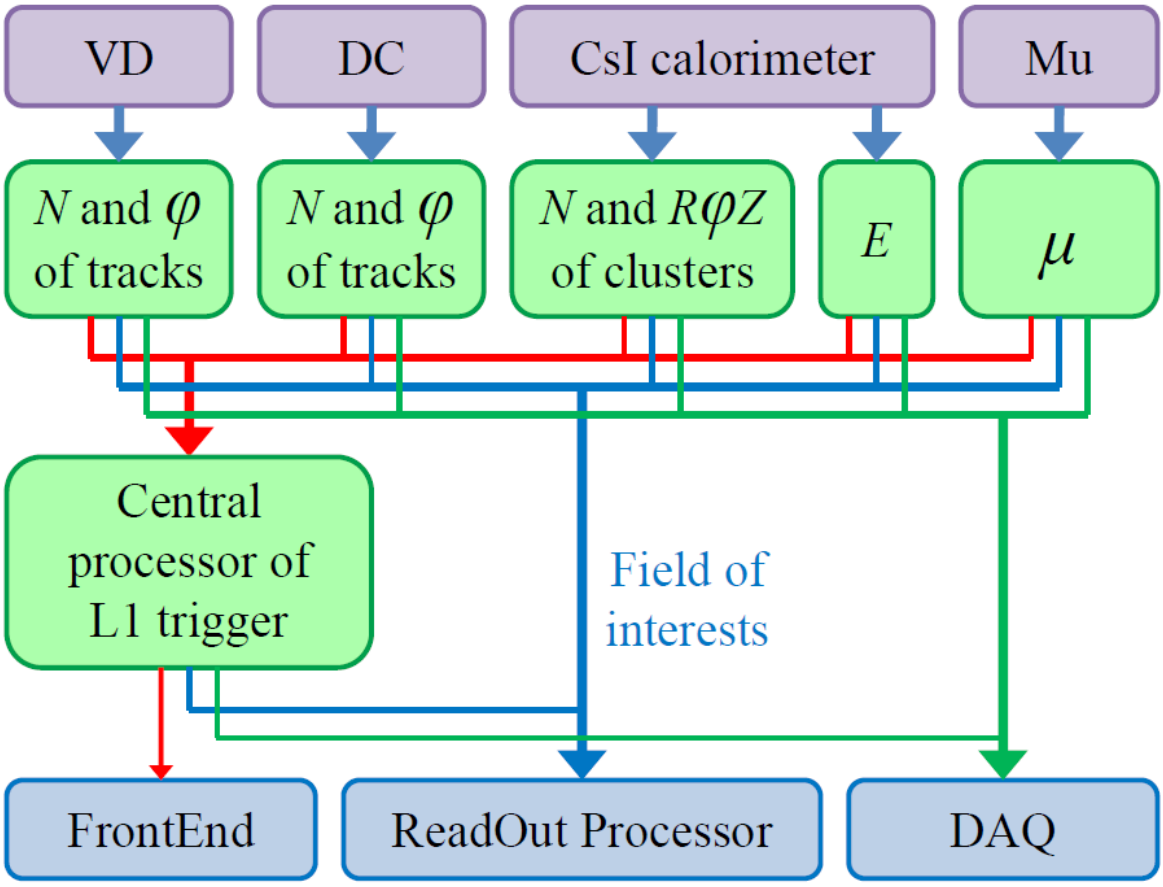

Figure 2.24: *A block diagram of the Level 1 trigger.*

2.11 Networking and computing systems

2.11.1 Introduction

Networking and computing infrastructure is going to play one of the key roles in operating the experiment at the CTF detector. Below we give a thorough overview of designing, building and operating the computing infrastructure for this experiment.

Section 2.11.2 contains a brief introduction to the prospected organization of trigger and DAQ, offline data processing, and data storage systems of the detector. It also gives an insight into the architecture and hardware requirements for the systems involved.

More details related to the data processing and storage systems of the experiment are given in Section 2.11.3. Some specific technical questions such as choosing the architecture of software execution environment for the experiment and ways of distributing the data processing activities of the detector experiment across local and remote computing facilities are also discussed here.

Section 2.11.4 is devoted to hardware and financial resource estimation for the proposed computing and networking solutions for the experiment. In addition, it contains plans for prototyping the key components of the detector computing systems and hardware deployment plans for the computing facilities supporting the experiment during the period of 2014–2025.

2.11.2 Brief Overview of TDAQ and Offline Data Processing Systems

The following three functional groups of components are forming the computing environment of the CTF experiment:

1. Trigger and DAQ systems:
   (a) a two-level hardware and software trigger system with a maximum trigger rate of 0.5 MHz for the average event size of approximately 30 KB, thus capable of generating the stream of output data with the rate up to 120 Gbps,
   (b) an event building system,
   (c) a storage buffer used for exporting data to the offline data processing systems.
2. Detector monitoring and control systems:
   (a) detector information system,
   (b) detector slow control system,
   (c) detector safety and access control systems,
   (d) engineering infrastructure and environment conditions monitoring systems,
   (e) dedicated control rooms for the continuous operation of the detector, its TDAQ systems and their computing infrastructure.
3. Detector offline data processing farm and its multilevel heterogeneous data storage system.

Data flow diagram between these functional groups is shown in Fig. 2.25.

The detailed diagram of the data flow originating from the detector and going through its TDAQ, offline data processing and storage system is shown in Fig. 2.26, which also displays the proposed capacities of the storage systems involved and the throughput values of network links interconnecting them. These values were derived by minimizing the price/performance ratio

for the whole detector computing system with respect to the financial estimations discussed in Section 2.11.4.1.

It is essential that the proposed configuration of TDAQ and offline farm make it possible to capture the full flux of data generated by the first level trigger and store it for the long term analysis if needed. For more detail about the architecture of the computing systems discussed here we refer to Section 2.11.3.1.

2.11.3 Architecture of the Data Processing and Storage Systems

2.11.3.1 Main Components

The following parts of networking and computing environment of the CTF experiment, which are listed below, do play an important role in the processes of accumulating experimental data, storing and processing. A short summary for each of them describes its functionality and interaction with other components in the list below and in addition provides with unique ID for future references.

1. **[FrontEnd1,2]** Modules of the front-end electronics installed within the volume of the detector located 17 m below the ground level in the dedicated detector building.

2. **[ReadOut1,2]** The following electronics equipment, which is installed in the dedicated racks in the vicinity of the detector and mechanically attached to it:

   (a) front-end electronics' power supplies,

   (b) detector subsystems' readout equipment,

   (c) Low Level Trigger (LLT) of the detector,

   (d) aggregation systems for experimental event fragments and output buffers for transferring the data aggregated to the Event Builder installed in the **[DataCenter1]** facility for further processing.

3. **[FiberTray1(a,b)]** Optical-fibers communication line connecting passive optical crossing **[FiberCross1(a,b)]**, placed on the ground level near the detector cavern with the **[ReadOut1,2]** modules, consisting of three parts:

   (a) fixed vertical section going down to the detector cavern within the dedicated cable trays (providing mechanical protection and tension control for fibers) attached to one of the walls of the cavern;

   (b) horizontal movable and retractable section which is capable of automatically adjusting itself to the position of the detector in the experimental cavern, supporting the fibers on their path from the wall of detector cavern to **[ReadOut1,2]** modules;

   (c) fixed section provided with radiation resistant fibers (discussed below in Section 2.11.3.2) going over the multiple paths from **[ReadOut1,2]** to **[FrontEnd1,2]** modules installed within the detector volume.

   The optical line consists of sixteen 24-core multichamber optical fiber cables (192 cores of SMF 9/125 optical fiber in total) subdivided into two equal sets of cables running over the physically independent paths within the detector cavern (at least 10 m separation along the path is required).

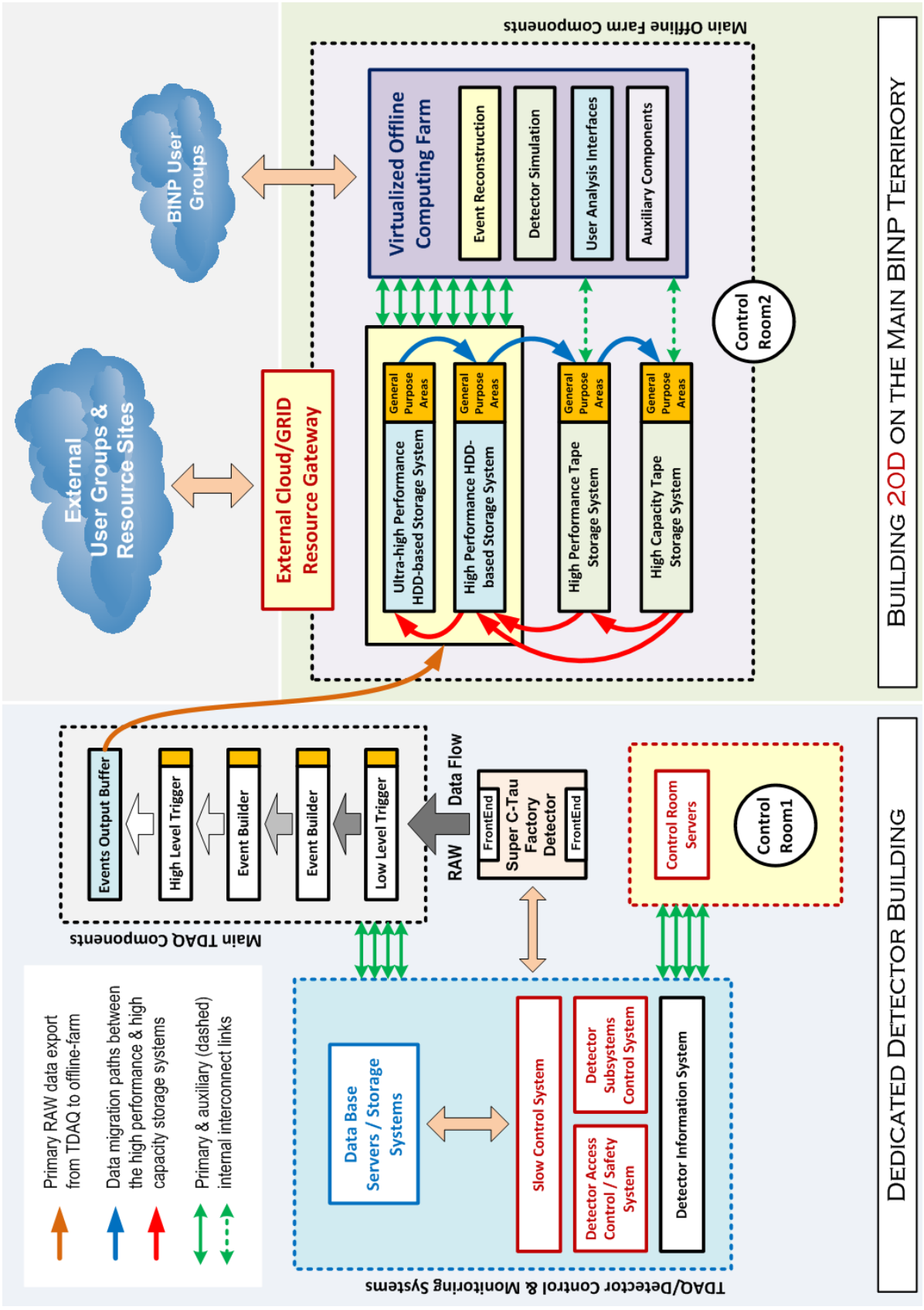

Figure 2.25: *Generic data flow diagram for TDAQ and offline data processing systems of the detector.*

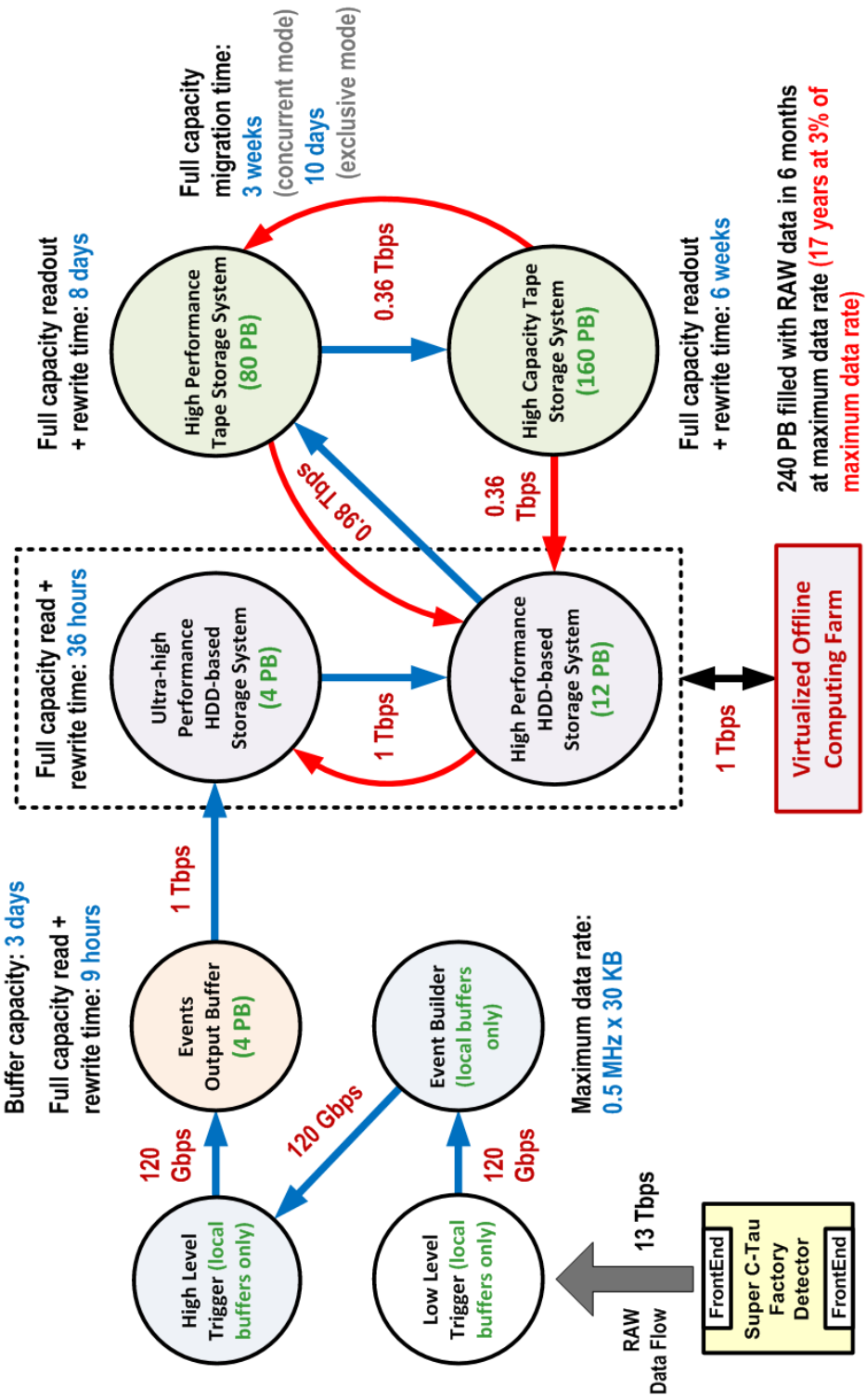

Figure 2.26: *Detailed diagram of the data flow originating from the detector and going through its TDAQ, offline data processing and storage systems. Capacities of the storage systems involved and the expected data rates between them in a simultaneous read/write mode are displayed as well.*

4. **[FiberTray2(a,b)]** Optical-fibers communication line connecting passive optical crossings **[FiberCross1(a,b)]** and **[FiberCross2]**, respectively (the total length is approximately 200 m over the fiber).

   The optical crossing consists of 8 optical patch panels supporting 24 pairs of fibers each distributed among four racks within the **[DataCenter1]** facility.

5. **[DataCenter1]** Computing facility located in the area number 114 of the dedicated detector building and hosting the following components:

   (a) passive optical crossing **[FiberCross2]**,

   (b) Event Fragment Input (EFI) and Event Builder (EB) subsystems,

   (c) High Level Trigger (HLT) of the detector experiment,

   (d) buffer storage systems used for exporting data between **[DataCenter1,2]** facilities,

   (e) passive optical crossing **[FiberCross3]** of the **[FiberTray3]** optical communication line linking **[DataCenter1,2]** facilities,

   (f) servers supporting detector control systems,

   (g) servers supporting environmental monitoring and detector safety systems,

   (h) servers supporting the main control room **[ControlRoom1]**,

   (i) terminal servers providing external access to the **[DataCenter1]** facility.

   Location of the **[DataCenter1]** facility and its engineering infrastructure within the dedicated detector building is shown in Fig. 2.28. The detailed equipment installation plan for the **[DataCenter1]** facility is given by Fig. 2.29. A list of basic specifications for the **[DataCenter1]** facility is given in Tab. 2.6.

6. **[DataCenter1Inf]** Engineering infrastructure of the **[DataCenter1]** computing facility deployed in the areas number 113, 113a, 115, 115a, and 116 of the dedicated detector building and its vicinity:

   (a) 10 kV power cables inlets,

   (b) dedicated transformed plant,

   (c) group of chiller modules serving the external cooling circuit of the **[DataCenter1]** facility,

   (d) external cargo bays for the areas number 113 and 115 of the detector building.

7. **[ControlRoom1]** Main detector control room constructed in the area number 112 of the detector building which holds control over the

   (a) detector subsystems and their engineering infrastructure,

   (b) entire **[DataCenter1]** computing facility including its safety and access control systems.

8. **[FiberTray3]** Optical-fibers communication line with the length not exceeding 2 km over the fiber linking the **[DataCenter1,2]** computing facilities. The optical line consists of four 48-core multichamber shielded optical fiber cables (192 cores of SMF 9/125 optical fiber in total).

9. **[DataCenter2]** Computing facility built within the existing BINP centralized IT facility hosting the following components:

   (a) passive optical crossing **[FiberCross4]** of the **[FiberTray3]** optical communication line linking **[DataCenter1,2]** facilities,

   (b) BINP general purpose internal networking core,

   (c) offline data processing farm of the experiment,

   (d) long term robotic tape storage system (several groups of tape robots),

   (e) central database servers of the experiment,

   (f) central backup system serving both **[DataCenter1,2]** facilities,

   (g) terminal servers providing external access to the **[DataCenter1]** facility.

   The prospected layout of the **[DataCenter2]** facility by 2020, assuming the major upgrade of its engineering infrastructure and deployment of all the equipment related the detector experiment is shown in Fig. 2.30.

10. List of basic specifications for the **[DataCenter2]** facility is given in Tab. 2.6.

11. **[DataCenter2Inf]** Engineering infrastructure of the **[DataCenter2]** computing facility deployed in the vicinity of its main IT area.

12. **[ControlRoom2]** Dedicated control room of the **[DataCenter2]** computing facility holding control of the IT equipment deployed within the **[DataCenter2]** facility and its engineering infrastructure, including safety and access control systems.

The generic layout of the key components of TDAQ, data processing and storage systems of the detector experiment listed above is shown in Fig. 2.27.

Possible extensions of the basic organizational scheme of the network and computing infrastructure of the experiment summarized here are discussed in Section 2.11.3.3.

2.11.3.2 Fiber-optics Communication Lines Deployed in the Vicinity of the Detector

As it was mentioned earlier in Section 2.11.3.1, the fiber-optics communication lines deployed in the vicinity of the detector, especially some subsections of **[FiberTray1]** must be provided with means of radiation protection in order to keep the lifetime of fibers at a reasonable level and minimize the rate of permanent fiber failures encountered over the detector lifetime.

The radiation protection of the fiber-optics communication lines is proposed to be achieved in one of the following ways:

1. identifying the spots with high radiation loads within the volume of detector by using the full detector simulation, which are to be avoided while tracing the paths of optical cables,

2. shielding the bunches of optical cables by using the custom design cable trays (for the cables deployed outside the detector volume),

3. using the radiation resistant optical fibers shielded with the special covers such as described in [132]–[136] to be deployed in the places where two previous solutions cannot be applied.

The optimal solution for the radiation resistant fiber-optics lines deployed within the detector is expected to be found while building and evaluating prototypes of the **[FiberTray1]** communication line which are proposed in Section 2.11.4.2.

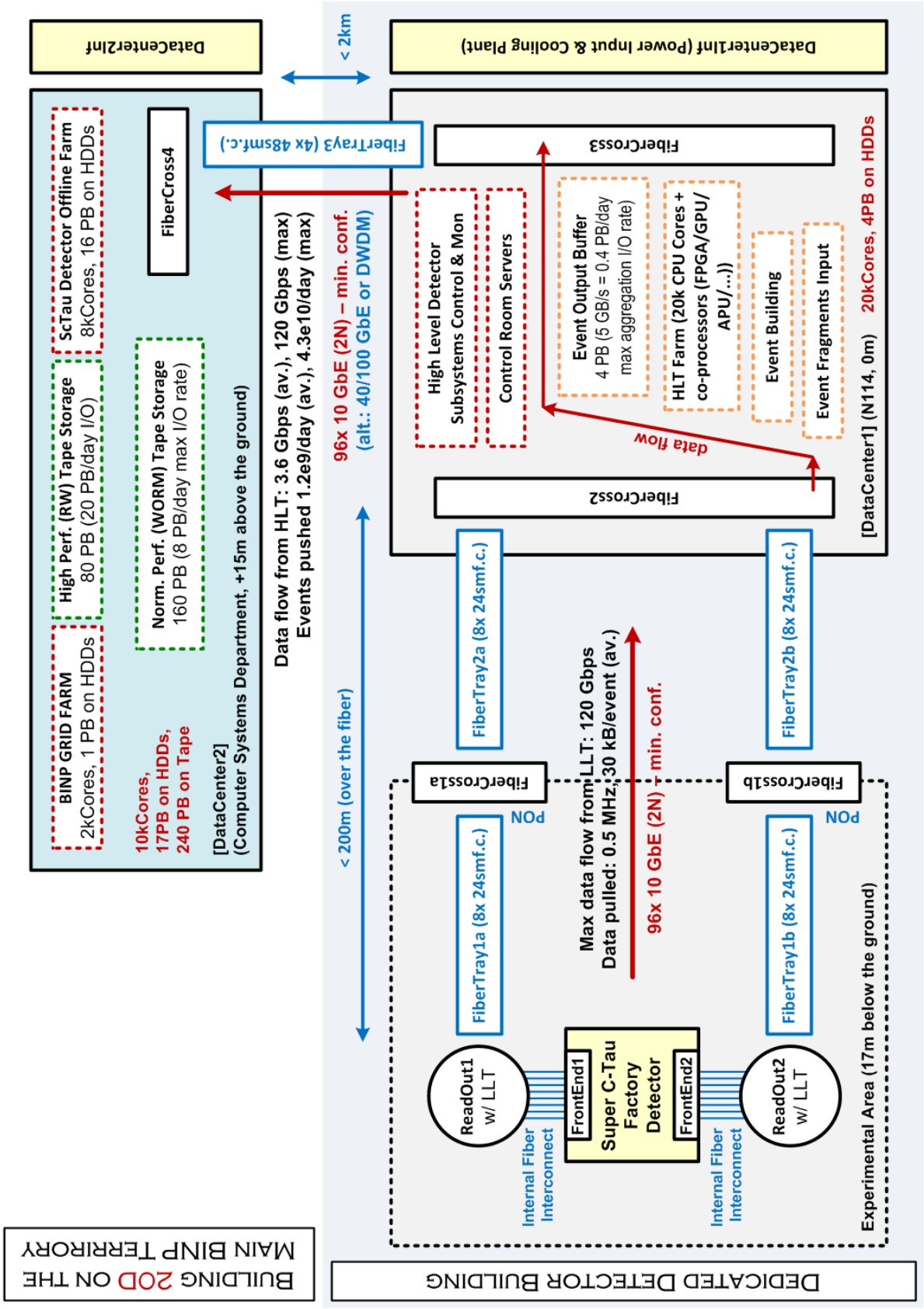

Figure 2.27: *Generic layout of the key components of TDAQ, data processing and storage systems of the experiment located both in the dedicated detector building and the existing computing facility on the main BINP territory.*

2.11.3.3 External Connectivity of [DataCenter1,2] Facilities and Discussion of the Possible Involvement of the Remote Computing Centers

All the network equipment providing the external connectivity for BINP and the detector in particular will be hosted at the **[DataCenter2]** computing facility, thus it will be playing a role of an external network gateway for the entire computing infrastructure of the experiment.

The prospected internal and external networking layout for all the HEP experiments carried out at BINP at early stages of building the networking and computing infrastructure for the detector is shown in Fig. 2.31.

So, even at the early stages of commissioning of the experiment and its networking and computing infrastructure, it will be provided with connectivity to Supercomputer Network of Novosibirsk Scientific Center (NSC/SCN) [137] via the dedicated 10 Gbps optical network which is in production since 2009. In a more distant future BINP may be getting direct access to the remote scientific networks such as Geant3 (GN3) [138] and international GRID systems such as WLCG [139] by means of the dedicated 1 Gbps optical links which would significantly enrich the list of data processing scenarios available for the CTF experiment and increase the peak amount of computing power available for BINP significantly.

If the capacity of external network links available to BINP is sufficient, the following extensions of the detector experiment network and computing design described earlier in Section 2.11.3.1 might be taken into consideration:

1. building an additional tape storage system on the geographically remote site in order to store a full copy of RAW data aggregated while doing experiments with the detector thus reducing the risks of data loss due to a catastrophic event on one of the sites;

2. building a geographically distributed group of computing sites merged into a single data processing entity by means of GRID technology or using the capacity of the existing regional and worldwide GRID infrastructure.

Use of the resources provided by the commercial Cloud computing systems such as Amazon EC2 [140] for the purposes of the data processing and experimental events simulation for the CTF experiment is not considered as an option, at least at the present moment, as the prices for the resources offered by the commercial Cloud systems remain at the level which makes the ownership of the dedicated computing farm a more preferable solution in our case.

2.11.3.4 Prospected Architecture of the Software Execution Environment

The standard execution environment designed to support all types of software related to events reconstruction, detector simulation, monitoring and control of the detector subsystems and other tasks is proposed to be virtualized, in order to gain the following advantages which hardware virtualization technology provides:

1. high reliability and rapid recovery of the virtualized services,

2. low level isolation of different types of services from each other,

3. ability to reproduce freezing the configuration execution environment over the periods of time such as the entire lifetime of detector experiment,

4. natural way of supporting heterogeneous computing systems, including Cloud computing enabled environments.

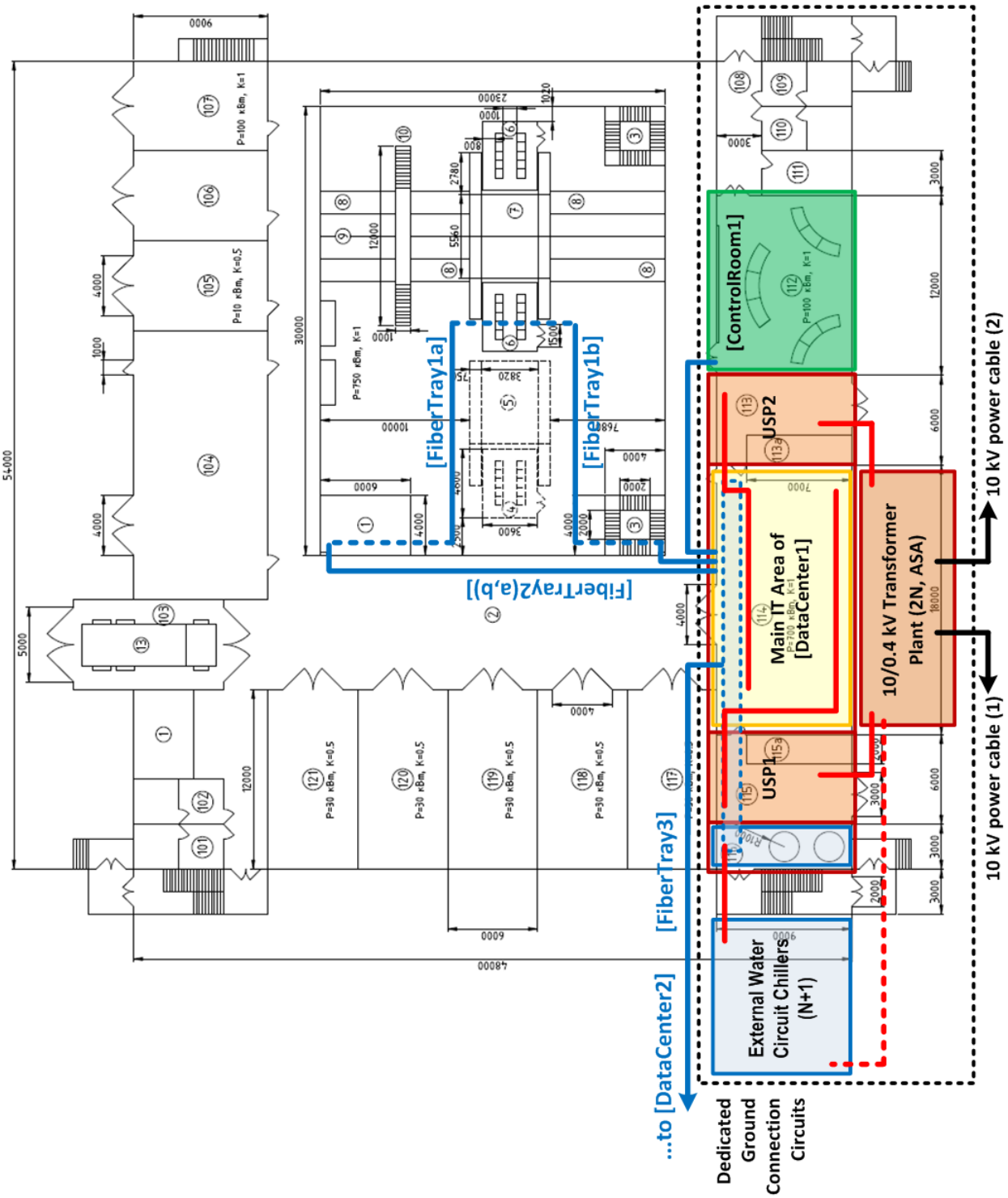

Figure 2.28: *Location of the* **[DataCenter1]** *facility and its engineering infrastructure within the dedicated detector building. The main control room of the experiment* **[ControlRoom1]** *is also shown.*

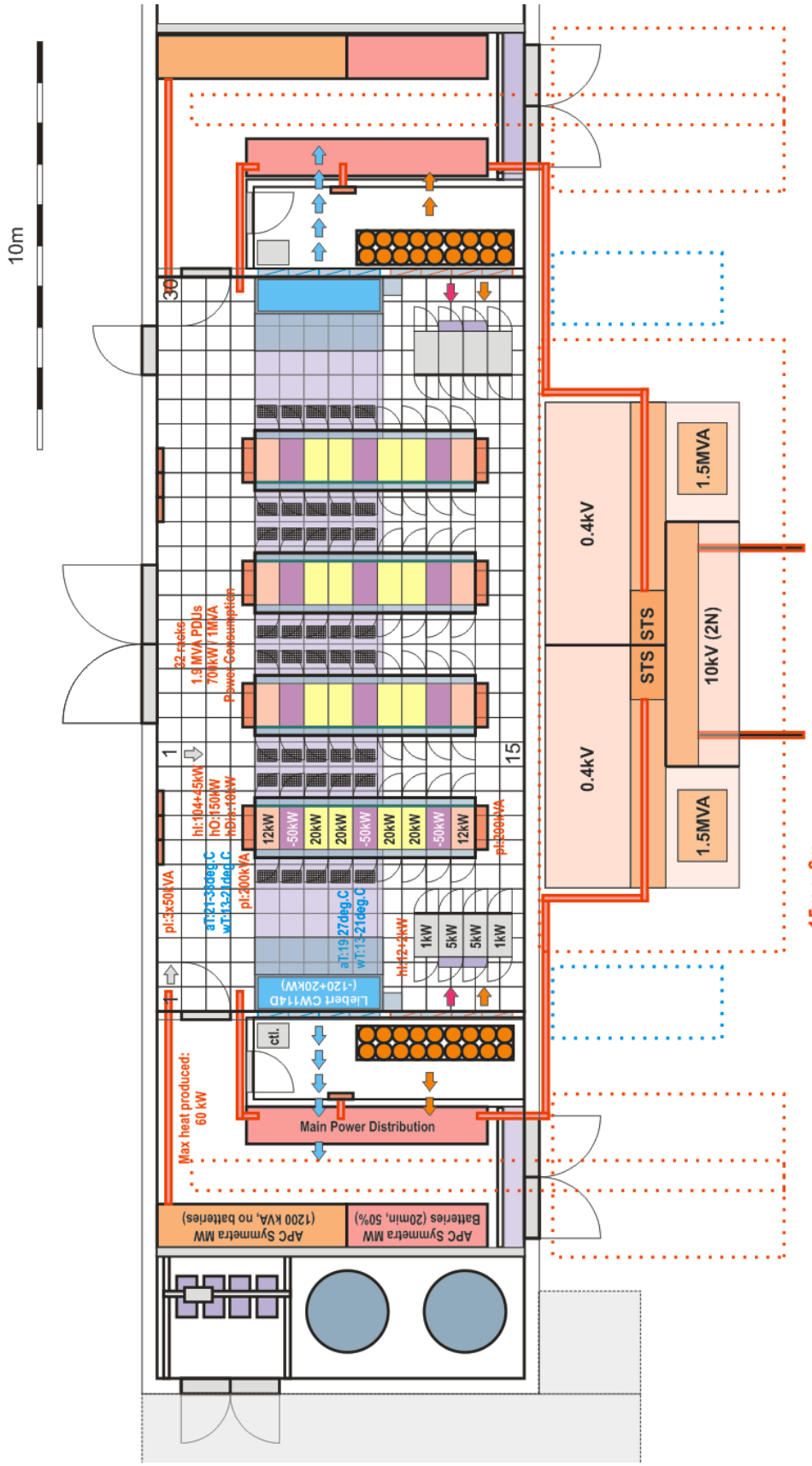

Figure 2.29: *Closer look on the hardware installation layout of the* **[DataCenter1]** *facility (cooling and electrical power capacities indicated).*

Figure 2.30: *Prospected layout of the* **[DataCenter2]** *facility by 2020, assuming the major upgrade of its engineering infrastructure and deployment of all the equipment related to the detector.*

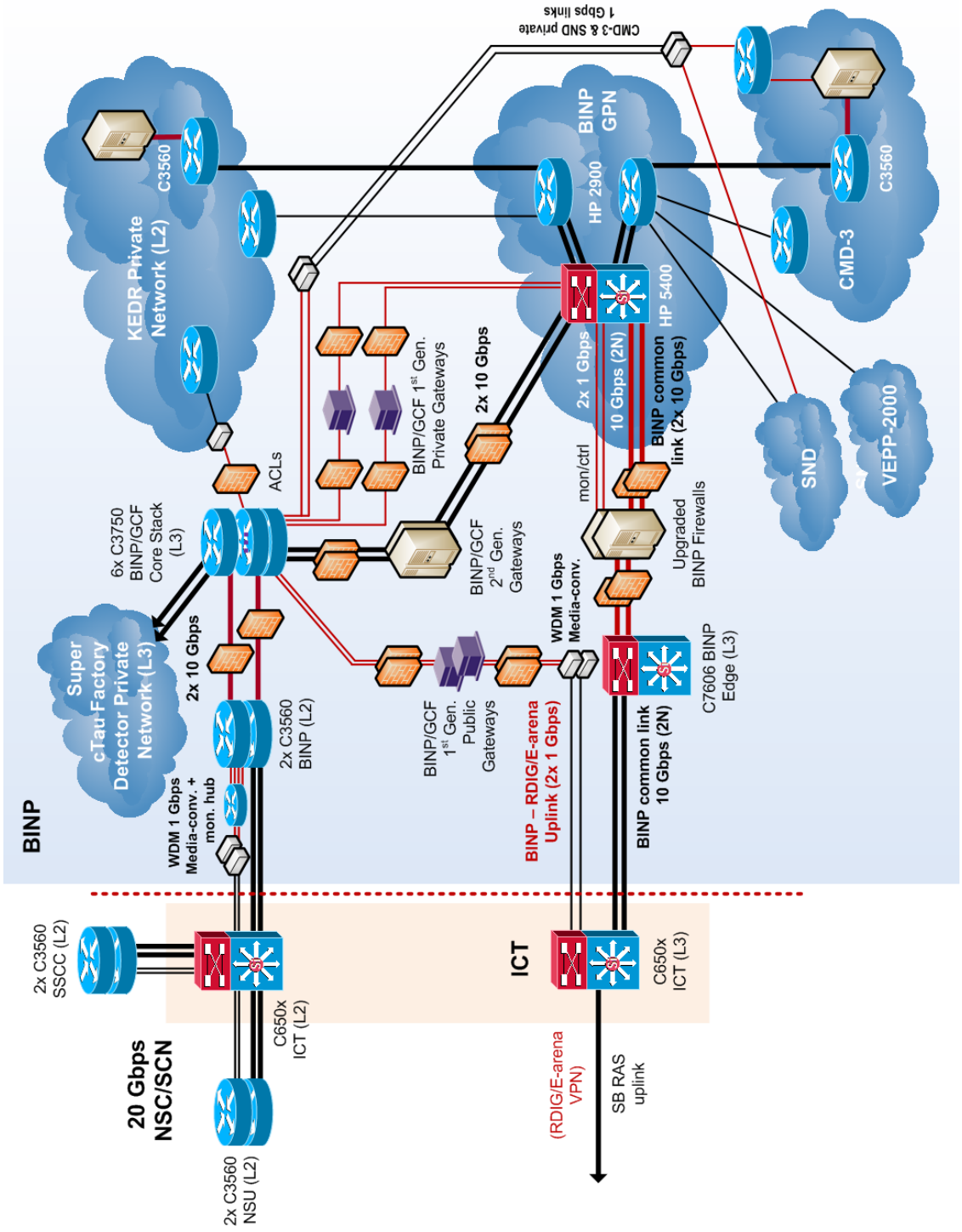

Figure 2.31: *Prospected internal and external networking layout for all the HEP experiments carried out at BINP at early stages of building the networking and computing infrastructure for the CTF experiment.*

Table 2.6: *List of basic specifications for the* **[DataCenter1,2]** *computing facilities.*

Feature	[DataCenter1]	[DataCenter2]
Total area (IT area), m^2	300 (160)	360 (220)
False floor load carrying capacity, ton/m^2	≤ 2	≤ 2
Number of racks (total rackmount capacity, 1U)	32 (1344)	76 (2432)
Maximum heat dissipation within a single rack, kW	20	12
Maximum heat dissipation within the IT area, kW	600	300
Maximum cooling capacity of the internal cooling circuit of the data center, kW (redundancy schema implemented)	800 (N+1)	480 (N+1)
Maximum cooling capacity of the external cooling circuit of the data center, kW (redundancy schema implemented)	1500 (N+1)	600 (N+1)
Time of running on the chilled water stored in the redundant water tanks of the internal cooling circuit of the data center, min	15	Unavailable
Maximum electrical power supported by the external power lines, kVA (redundancy scheme implemented)	1500 (2N)	500 (2N)
Maximum load supported by the centralized UPS system, kVA (redundancy scheme implemented)	1200 (2N)	465 (2N)
Centralized UPS capacity for 100% / 50% / 10% of nominal power consumption by the IT equipment, min	20 / 40 / 150	
Data center external connectivity, Gbps (redundancy scheme implemented for the external uplinks)	Unavailable	40 (2(2N))
Capacity of the internal communication lines between the [DataCenter1,2] facilities, Gbps (redundancy scheme implemented for the internal links)	960 (2N)	
Monitoring and maintenance services by the local personnel	$365 \times 24 \times 7$	

Scientific Linux [141] is proposed to be used as a standard OS for the detector experiment while XEN [142] or KVM [143] (both are non-commercial products) would be the most preferable choice for the standard virtualization platform to be deployed over the offline farm computing resources. The virtualized environment of the offline farm is intended to be supplied with the custom design high level control tools, implemented privately.

In case the offline data processing scheme for the detector is extended in order to include GRID computing technology support and the data processing within the geographically distributed environment, gLite middleware [147] should be considered as a preferable choice of the standard GRID middleware for the experiment.

2.11.4 Roadmap for Building the Offline Computing and Storage Systems

2.11.4.1 Hardware Commissioning Plan

As it was mentioned earlier in Section 2.11.2, the maximum trigger rate of the first level trigger (LLT) of the detector is equal to 0.5 MHz while the average experimental event size is estimated to be around 30 kB. The TDAQ and offline data processing systems of the detector are designed in such a way that the whole flux of data generated by the LLT could be saved on the storage systems of the offline farm for the long-term analysis. Thus the maximum output data rate of the detector TDAQ system is estimated to be 15 GBps = 120 Gbps (which is equivalent of 1.24 PB/day = 470 PB/year), so the maximum amount of data which could be generated by the TDAQ system over the 5 years of constant operation (with 100% efficiency) is equal to 2.4 EB.

If the period of running at maximum luminosity with the CTF experiment is going to be 2018–2023, then the optimal period for hardware deployment for the offline farm is estimated to be 2016–2019, and for the HDD and tape based storage systems — 2017–2022 (assuming linear growth of the amount of data aggregated on the detector storage systems with time). Therefore the detailed specifications for the hardware components needed for implementing networking and computing system of the detector is to be prepared first in 2015 and then reevaluated in 2018.

In order to estimate the amount of financial resources required for building and operating the solutions for the networking and computing systems of the detector experiment over the designated period of time, let us make the following assumptions.

1. The optimal ratio of the total computing powers aggregated within the HLT trigger farm to the capacity of high performance storage system available within the offline data processing farm is equal to 3.0 kHepSPEC/PB (which is equivalent1 to approximately 12.0 MSI2K/PB or 25 TFlops/PB) and fixed over the whole period of 2014–2025.

2. Ratio of capacities of high performance tape storage system to all the HDD based storage systems within the detector TDAQ and offline data processing farm is fixed to 4.0 for the whole period of 2014–2025.

3. Ratio of prices per unit of storage system capacity for high performance tape storage systems and HDD based storage systems is fixed to 0.5 for the whole period of 2014–2025.

4. The assumptions for price evolution and energy efficiency for the general purpose CPU based computing nodes and HDD based storage systems summarized in Tab. 2.7 are valid for the whole period of 2014–2022.

Under these assumptions the total cost of the experiment' computing system (without its engineering infrastructure – computing and networking hardware only) consisting of

Table 2.7: *Cost and energy efficiency estimations for the computing and storage system hardware during the period of 2014–2022 (the averaged values for the subperiods of particular interest are also shown).*

	CPU grad	1.3		Disk grad	1.2		Pwr. grad	1.1	
Year	*2014*	*2015*	*2016*	*2017*	*2018*	*2019*	*2020*	*2021*	*2022*
W/HepSPEC	3.83	3.48	3.16	2.87	2.61	2.37	2.15	1.95	1.77
kW/PB	24	21.8	19.8	18	16.4	14.9	13.5	12.3	11.2
$/HepSPEC	150	115.4	88.8	68.3	52.5	40.4	31.1	23.9	18.4
M$/PB	0.4	0.33	0.28	0.23	0.19	0.16	0.13	0.11	0.09

Average, years	*2016-2019*	*2017-2022*		*kHepSPEC*	60	20	*PB*		
W/HepSPEC	2.75	2.29		kW	165.2				
kW/PB	17.3	14.4		kW		287.7		453 kW	
$/HepSPEC	62.5	39.1		M$	3.75				
M$/PB	0.22	0.15		M$		9.1		12.8 M$	

- computing nodes with 0.5 PFlops of combined performance (to be deployed in 2016–2019),
- high performance HDD based storage system for the offline data processing farm and TDAQ with total capacity of 20 PB (to be deployed in 2017–2022),
- high performance tape storage with total capacity of 80 PB (to be deployed in 2017–2022),

is estimated to be approximately 13 M$ and its combined heat dissipation in its final configuration is to be about 0.5 MW. An ambiguity of these values is assumed to be no better than 15–20%.

Building the offline farm and data storage system in such a configuration would make it possible to store 3% of maximum integral data flow generated by the detector's LLT over the 5 years (2.4 EB) in the average. In this case the average trigger rate is going to be around 20 kHz which delivers approximately $3 \cdot 10^{12}$ experimental events over the 5 years (with 100% efficiency). With such a configuration, the ratio of total computing performance and the maximum number of evens stored on the high performance HDD based storage system for the offline farm would be around 0.8 kFlops by 2020.

Once the high performance tape storage systems is filled up to 70–80% of its capacity (presumably by 2020) the deployment of the second stage (high capacity) tape storage system on the IT area of **[DataCenter2]** facility is to be done, thus increasing the tape storage capacity available for the experiment by 160 PB (by the end of deployment period in 2025). The cost estimation for this particular subsystem is not included in the values mentioned above.

2.11.4.2 Building the Prototypes for the Key Components of Data Processing and Storage Systems

Validation of the solutions proposed above for various components of networking and computing infrastructure of the detector experiment is to be done via building and testing the prototypes for each and every critical part of the infrastructure.

A list of the components which are to be evaluated by building the prototypes is given below.

1. HDD/SSD-based high performance storage systems:
   (a) fault-tolerant data storage systems based on redundant groups of RAID arrays,

(b) distributed and parallel file systems (Lustre [144], PVFS2 [145], Hadoop [146], etc.),

(c) multilevel I/O buffers for the storage system head nodes based on high performance SSD devices [128], [129].

2. Robotic tape libraries and tape media: studying the existing solutions for scalable modular robotic tape libraries [130]–[131].

3. High performance computing modules based on general purpose CPUs [123]–[125].

4. Hybrid computing architectures making use of GPU/FPGA based solutions [117]–[122], [126], [127]:

   (a) finding ways to maximize performance of EB and HLT subsystems (TDAQ),

   (b) studying feasibility of increasing performance of event reconstruction/simulation jobs running on the offline data processing farm.

5. Advanced networks:

   (a) 40/100 Gigabit Ethernet and IPoIB technologies,

   (b) Fiber Channel and FCoE technologies,

   (c) DWDM technology.

6. Radiation resistant optical fiber communication lines (Chapter 2.11.3.2).

7. Environmental control systems for industrial and IT applications, industrial process control systems:

   (a) groups of compact localized sensors similar to the solution [148],

   (b) distributed optical fiber based sensor systems with the readout performed from one of the endpoints, similar to the ones described in [149],

   (c) hybrid optical fiber based sensor systems supporting both distributed and localized information gathering along the path of the fiber, similar to those described in [150], [151].

Bibliography

[1] N. Brambilla *et al.* [Quarkonium Working Group], arXiv:hep-ph/0412158; N. Brambilla *et al.* [Quarkonium Working Group], arXiv:1010.5827; G.V. Pakhlova, P.N. Pakhlov and S.I. Eidelman, Phys. Usp. **53**, 219 (2010).

[2] K. Nakamura *et al.* [Particle Data Group], J. Phys. G **37**, 075021 (2010).

[3] D. Besson *et al.* [CLEO Collaboration], Phys. Rev. Lett. **96**, 092002 (2006) [arXiv:hep-ex/0512038].

[4] M. Ablikim *et al.* [BES Collaboration], Phys. Lett. B **660**, 315 (2008) [arXiv:0705.4500 [hep-ex]].

[5] J. L. Rosner *et al.* [CLEO Collaboration], Phys. Rev. Lett. **95**, 102003 (2005) [arXiv:hep-ex/0505073]; P. Rubin *et al.* [CLEO Collaboration], Phys. Rev. D **72**, 092004 (2005) [arXiv:hep-ex/0508037]; S. Dobbs *et al.* [CLEO Collaboration], Phys. Rev. Lett. **101**, 182003 (2008) [arXiv:0805.4599 [hep-ex]]; G. S.Adams *et al.* [CLEO Collaboration], Phys. Rev. D **80**, 051106 (2009) [arXiv:0906.4470 [hep-ex]].

[6] E. Eichten, S. Godfrey, H. Mahlke and J. L. Rosner, Rev. Mod. Phys. **80**, 1161 (2008) [arXiv:hep-ph/0701208].

[7] E. Klem and A. Zaitsev, Phys. Repts. **454**, 1 (2007) [arXiv:0708.4016 [hep-ph]].

[8] B. Aubert *et al.* [BABAR Collaboration], Phys. Rev. Lett. **98**, 212001 (2007) [arXiv:hep-ex/0610057].

[9] X. L. Wang *et al.* [Belle Collaboration], Phys. Rev. Lett. **99**, 142002 (2007) [arXiv:0707.3699 [hep-ex]].

[10] K. Abe *et al.* [Belle Collaboration], Phys. Rev. Lett. **100**, 142001 (2008) [arXiv:0708.1790 [hep-ex]].

[11] T. Barnes, Int. J. Mod. Phys. A **21**, 5583 (2006) [arXiv:hep-ph/0608103].

[12] M. A. Sanchis-Lozano, Z. Phys. C **62**, 271 (1994).

[13] K. K. Sharma and R. C. Verma, Int. J. Mod. Phys. A **14**, 937 (1999) [arXiv:hep-ph/9801202].

[14] A. Datta, P. J. O'Donnell, S. Pakvasa and X. Zhang, Phys. Rev. D **60**, 014011 (1999) [arXiv:hep-ph/9812325].

[15] G. Goggi and G. Penso, Nucl. Phys. B **165**, 429 (1980).

[16] W. J. Huo, T. F. Feng and C. x. Yue, Phys. Rev. D **67**, 114001 (2003) [arXiv:hep-ph/0212211].

[17] Y. Miyazaki *et al.* [Belle Collaboration], Phys. Lett. B **660**, 154 (2008) [arXiv:0711.2189 [hep-ex]].

[18] J. P. Ma, R. G. Ping and B. S. Zou, Phys. Lett. B **580**, 163 (2004) [arXiv:hep-ph/0311012].

[19] X. G. He, J. P. Ma and B. McKellar, Phys. Rev. D **47**, 1744 (1993) [arXiv:hep-ph/9211276].

[20] C. J. Morningstar and M. J. Peardon, Phys. Rev. D **60**, 034509 (1999) [arXiv:hep-lat/9901004].

[21] A. Hart, C. McNeile, C. Michael and J. Pickavance [UKQCD Collaboration], Phys. Rev. D **74**, 114504 (2006) [arXiv:hep-lat/0608026].

[22] S. Dobbs *et al.* [CLEO Collaboration], Phys. Rev. D **76**, 112001 (2007) [arXiv:0709.3783 [hep-ex]].

[23] R. Poling, *In the Proceedings of 4th Flavor Physics and CP Violation Conference (FPCP 2006), Vancouver, British Columbia, Canada, 9-12 Apr 2006, pp 005* [arXiv:hep-ex/0606016].

[24] E. S. Swanson, Phys. Rept. **429**, 243 (2006) [arXiv:hep-ph/0601110].

[25] G. Pakhlova *et al.* [Belle Collaboration], Phys. Rev. Lett. **100**,062001 (2008) [arXiv:0708.3313 [hep-ex]].

[26] T. J. Burns, F. E. Close and C. E. Thomas, Phys. Rev. D **77**, 034008 (2008) [arXiv:0709.1816 [hep-ph]].

[27] A. V. Evdokimov *et al.* [SELEX Collaboration], Phys. Rev. Lett. **93**, 242001 (2004) [arXiv:hep-ex/0406045].

[28] J. Brodzicka *et al.* [Belle Collaboration], Phys. Rev. Lett. **100**, 092001 (2008) [arXiv:0707.3491 [hep-ex]].

[29] B. Aubert *et al.* [BABAR Collaboration], Phys. Rev. Lett. **97**, 222001 (2006) [arXiv:hep-ex/0607082].

[30] A. Bondar and A. Poluektov, Eur. Phys. J. C **47**, 347 (2006) [arXiv:hep-ph/0510246].

[31] B. I. Eisenstein *et al.* [CLEO Collaboration], Phys. Rev. D **78**, 052003 (2008) [arXiv:0806.2112 [hep-ex]].

[32] J. P. Alexander *et al.* [CLEO Collaboration], Phys. Rev. D **79**, 052001 (2009) [arXiv:0901.1216 [hep-ex]].

[33] CKM Fitter Group Home Page, http://www.slac.stanford.edu/xorg/ckmfitter

[34] E. Follana, C. T. H. Davies, G. P. Lepage and J. Shigemitsu [HPQCD Collaboration], Phys. Rev. Lett. **100**, 062002 (2008) [arXiv:0706.1726 [hep-lat]].

[35] N. E. Adam *et al.* [CLEO Collaboration], Phys. Rev. Lett. **97**, 251801 (2006) [arXiv:hep-ex/0604044].

[36] C. Aubin *et al.* [Fermilab Lattice Collaboration], Phys. Rev. Lett. **94**, 011601 (2005) [arXiv:hep-ph/0408306].

[37] D. Besson [CLEO Collaboration], Phys. Rev. D **80**, 032005 (2009) [arXiv:0906.2983 [hep-ex]].

[38] S. Bianco, F. L. Fabbri, D. Benson and I. Bigi, Riv. Nuovo Cim. **26**, 1 (2003) [arXiv:hep-ex/0309021].

[39] Heavy Flavor Averaging Group Home Page, http://www.slac.stanford.edu/xorg/hfag/

[40] D. M. Asner and W. M. Sun, Phys. Rev. D **73**, 034024 (2006) [arXiv:hep-ph/0507238].

[41] X. D. Cheng, K. L. He, H. B. Li, Y. F. Wang and M. Z. Yang, Phys. Rev. D **75**, 094019 (2007) [arXiv:0704.0120 [hep-ex]].

[42] A. Bondar, A. Poluektov, V. Vorobiev, Phys. Rev. D **82**, 034033 (2010) [arXiv:1004.2350].

[43] M. Bona *et al.*, arXiv:0709.0451 [hep-ex].

[44] H. Mendez *et al.* [CLEO Collaboration], Phys. Rev. D **81**, 052013 (2010) [arXiv:0906.3198 [hep-ex]].

[45] G. Bonvicini *et al.* [CLEO Collaboration], Phys. Rev. D **63**, 071101 (2001).

[46] D. M. Asner *et al.* [CLEO Collaboration], Phys. Rev. D **70**, 091101 (2004).

[47] B. Aubert *et al.* [BABAR Collaboration], Phys. Rev. D **78**, 051102 (2008) [arXiv:0802.4035 [hep-ex]].

[48] E. M. Aitala *et al.* [E791 Collaboration], Phys. Lett. B **403**, 377 (1997).

[49] X. C. Tian *et al.* [BELLE Collaboration], Phys. Rev. Lett. **95**, 231801 (2005).

[50] J. M. Link *et al.* [FOCUS Collaboration], Phys. Lett. B **622**, 239 (2005).

[51] B. Aubert *et al.* [BaBar Collaboration], Phys. Rev. Lett. **100**, 061803 (2008) [arXiv:0709.2715 [hep-ex]].

[52] M. Staric *et al.* [Belle Collaboration], Phys. Lett. B **670**, 190 (2008) [arXiv:0807.0148 [hep-ex]].

[53] Y. Grossman, A. L. Kagan and Y. Nir, Phys. Rev. D **75**, 036008 (2007) [arXiv:hep-ph/0609178].

[54] B. Aubert *et al.* [BABAR Collaboration], Phys. Rev. D **78**, 011105 (2008) [arXiv:0712.2249].

[55] M. Staric *et al.* [Belle Collaboration], Phys. Rev. Lett. **98**, 211803 (2007) [arXiv:hep-ex/0703036].

[56] A. A. Petrov, arXiv:0711.1564 [hep-ph].

[57] D. s. Du, Eur. Phys. J. C **50**, 579 (2007) [arXiv:hep-ph/0608313].

[58] A. A. Petrov, Phys. Rev. D **69**, 111901 (2004) [arXiv:hep-ph/0403030].

[59] D. M. Asner *et al.* [CLEO Collaboration], Phys. Rev. D **70**, 091101 (2004) [arXiv:hep-ex/0311033].

[60] I. I. Bigi, arXiv:0710.2714 [hep-ph].

[61] A. Datta and D. London, Int. J. Mod. Phys. A **19**, 2505 (2004) [arXiv:hep-ph/0303159].

[62] G. Burdman and I. Shipsey, Ann. Rev. Nucl. Part. Sci. **53**, 431 (2003) [arXiv:hep-ph/0310076].

[63] K. Abe *et al.* [Belle Collaboration], Phys. Rev. Lett. **92**, 101803 (2004) [arXiv:hep-ex/0308037].

[64] V. M. Abazov *et al.* [D0 Collaboration], Phys. Rev. Lett. **100**, 101801 (2008) [arXiv:0708.2094 [hep-ex]].

[65] S. Prelovsek and D. Wyler, Phys. Lett. B **500**, 304 (2001) [arXiv:hep-ph/0012116].

[66] G. Burdman, E. Golowich, J. L. Hewett and S. Pakvasa, Phys. Rev. D **66**, 014009 (2002) [arXiv:hep-ph/0112235].

[67] S. Fajfer, N. Kosnik and S. Prelovsek, Phys. Rev. D **76**, 074010 (2007) [arXiv:0706.1133 [hep-ph]].

[68] T. E. Coan *et al.* [CLEO Collaboration], Phys. Rev. Lett. **90**, 101801 (2003) [arXiv:hep-ex/0212045].

[69] B. Aubert *et al.* [BABAR Collaboration], Phys. Rev. Lett. **93**, 191801 (2004) [arXiv:hep-ex/0408023].

[70] A. Freyberger *et al.* [CLEO Collaboration], Phys. Rev. Lett. **76**, 3065 (1996) [Erratum-ibid. **77**, 2147 (1996)].

[71] Q. He *et al.* [CLEO Collaboration], Phys. Rev. Lett. **95**, 221802 (2005) [arXiv:hep-ex/0508031].

[72] B. Aubert *et al.* [BABAR Collaboration], arXiv:hep-ex/0607051.

[73] K. Kodama *et al.* [E653 Collaboration], Phys. Lett. B **345**, 85 (1995).

[74] D. Pirjol and T. M. Yan, Phys. Rev. D **56**, 5483 (1997) [arXiv:hep-ph/9701291].

[75] R. Mizuk, arXiv:0712.0310 [hep-ex].

[76] G. Pakhlova *et al.* [Belle Collaboration], Phys. Rev. Lett. **101**, 172001 (2008) [arXiv:0807.4458 [hep-ex]].

[77] E. Braaten, S. Narison and A. Pich, Nucl. Phys. B **373**, 581 (1992).

[78] S. Bethke, arXiv:0908.1135 [hep-ph].

[79] E. Gamiz, M. Jamin, A. Pich, J. Prades and F. Schwab, JHEP **0301**, 060 (2003) [arXiv:hep-ph/0212230]; Phys. Rev. Lett. **94**, 011803 (2005) [arXiv:hep-ph/0408044].

[80] L. Michel, Proc. Phys. Soc. A **63**, 514 (1950); C. Bouchiat and L. Michel, Phys. Rev. **106**, 170 (1957).

[81] J. R. Ellis, J. Hisano, M. Raidal and Y. Shimizu, Phys. Rev. D **66**, 115013 (2002) [arXiv:hep-ph/0206110]; T. Fukuyama, T. Kikuchi and N. Okada, Phys. Rev. D **68**, 033012 (2003) [arXiv:hep-ph/0304190]; A. Brignole and A. Rossi, Phys. Lett. B **566**, 217 (2003) [arXiv:hep-ph/0304081].

[82] I. I. Bigi and A. I. Sanda, Phys. Lett. B **625**, 47 (2005) [arXiv:hep-ph/0506037].

[83] Y. S. Tsai, SLAC-PUB-5003

[84] Y. S. Tsai, Phys. Rev. D **51**, 3172 (1995) [arXiv:hep-ph/9410265].

[85] J. H. Kuhn and E. Mirkes, Phys. Lett. B **398**, 407 (1997) [arXiv:hep-ph/9609502].

[86] A. Datta, K. Kiers, D. London, P. J. O'Donnell and A. Szynkman, Phys. Rev. D **75**, 074007 (2007) [Erratum-ibid. D **76**, 079902 (2007)] [arXiv:hep-ph/0610162].

[87] D. Delepine, G. Faisl, S. Khalil and G. L. Castro, Phys. Rev. D **74**, 056004 (2006) [arXiv:hep-ph/0608008].

[88] K. Kiers, K. Little, A. Datta, D. London, M. Nagashima and A. Szynkman, Phys. Rev. D **78**, 113008 (2008) [arXiv:0808.1707 [hep-ph]].

[89] P. Avery *et al.* [CLEO Collaboration], Phys. Rev. D **64**, 092005 (2001) [arXiv:hep-ex/0104009].

[90] G. Bonvicini *et al.* [CLEO Collaboration], Phys. Rev. Lett. **88**, 111803 (2002) [arXiv:hep-ex/0111095].

[91] V. P. Druzhinin, arXiv:0710.3455 [hep-ex].

[92] W.Lepeltier, Review on TPC's, J. Phys.: Conf. Ser. 65 012001, 2007.

[93] W.Erni, I.Keshelashvili, B.Krusche et all, Physics Performance Report for PANDA, http://arxiv.org/abs/0903.3905v1, 2009.

[94] F.Sauli, Nucl. Instrum. Methods 386, 531, 1997.

[95] M.Dixit et all, Micromegas TPC studies at high magnetic fields using the charge dispersion signal, Nucl. Instrum. Methods A 581, 254-257, 2007.

[96] Klaus Dehmelt for LP TPC Collaboration, A large prototype of a time projection chamber for a linear collider detector, Nucl. Instrum. Methods A, in press, 2010.

[97] N. Akopov et al., "The HERMES dual-radiator ring imaging Cerenkov detector," Nucl. Instr. and Meth. A 479 (2002) 511 [arXiv:physics/0104033].

[98] [LHC-B Collaboration], "LHCb: RICH technical design report," CERN-LHCC-2000-037, LHCb TDR 3, 7 September 2000.

[99] M. Buenerd [AMS RICH Collaboration], "The RICH counter of the AMS experiment," Nucl. Instr. and Meth. A 502 (2003) 158 [arXiv:astro-ph/0211645].

[100] A.Yu. Barnyakov et.al., "Focusing aerogel RICH (FARICH)," Nucl. Instr. and Meth. A553 (2005) 70.

[101] В.М.Аульченко и др. Мюонная система детектора КЕДР. Препринт ИЯФ 2000-48.

[102] B. Aubert *et al.* [BABAR Collaboration], Nucl. Instr. Meth. A **479**, 1 (2002).

[103] C.O. Vuosalo, A.V. Telnov, K.T. Flood, BABAR Analysis Document #1853, 2010.

[104] A. Abashian *et al.*, Nucl. Instr. Meth. A **491**, 69 (2002).

[105] N. Akopov *et al.*, Nucl. Instr. Meth. A **479**, 511 (2002) [arXiv:physics/0104033].

[106] [LHC-b Collaboration], CERN-LHCC-2000-037, LHCb TDR 3, 7 September 2000.

[107] M. Buenerd [AMS RICH Collaboration], Nucl. Instr. Meth. A **502**, 158 (2003) [arXiv:astro-ph/0211645].

[108] T. Iijima *et al.*, Nucl. Instr. Meth. A **548**, 383 (2005),
S. Korpar *et al.*, Nucl. Instr. Meth. A **553**, 64 (2005),
P. Krizan, S. Korpar, T. Iijima, Nucl. Instr. Meth. A **565**, 457 (2006).

[109] A.Yu. Barnyakov *et al.*, Nucl. Instr. Meth. A **595**, 100 (2008).

[110] G. Bondarenko, B. Dolgoshein, V. Golovin, A. Ilyin, R. Klanner, E. Popova, Proc. of the 5th Int. Conf. on Advanced Technology and Particle Physics, Nucl. Phys. B — Proc.Suppl. **61** (1998) 3 pp. 347.
G. Bondarenko *et al.*, Nucl. Instr. Meth. A **442**, 187 (2000).
Z. Sadygov *et al.*, Nucl. Instr. Meth. A **504**, 301 (2003).

[111] J. Benitez *et al.*, Nucl. Instr. Meth. A **595**, 104 (2008).

[112] A. Abashian *et al.* [Belle Collaboration], Nucl. Instr. Meth. A **479**, 117 (2002).

[113] Y. Yusa, Nucl. Instr. Meth. A **598**, 183 (2009).

[114] V. Smakhtin *et al.*, Nucl. Instr. Meth. A **598**, 196 (2009).

[115] MINIOS collaboration, TDR on scintillator, ch.5, http://www-numi.fnal.gov/minwork/info/tdr/mintdr_5.pdf

[116] V.M.Aulchenko *et al.*, Nucl. Inst. Meth. A **265**, 137 (1988).

[117] NVidia Fermi Architecture: http://www.nvidia.ru/object/fermi_architecture_ru.html

[118] Xilinx 7th series FPGA Products: http://www.xilinx.com/technology/roadmap/7-series-fpgas.htm

[119] Convey Hybrid Computing Platform:
http://www.conveycomputer.com/products.html

[120] Convey HC-1 Family Products:
http://www.conveycomputer.com/Resources/Convey_HC1_Family.pdf

[121] Nallatech PCI Express Cards: http://www.nallatech.com/pci-express-cards.html

[122] AMD Fusion Family of APUs: http://sites.amd.com/us/fusion/APU/Pages/fusion.aspx

[123] Intel Product Roadmap: http://download.intel.com/products/roadmap/roadmap.pdf

[124] List of Intel Microprocessors: http://en.wikipedia.org/wiki/List_of_Intel_microprocessors

[125] List of AMD Microprocessors: http://en.wikipedia.org/wiki/List_of_AMD_microprocessors

[126] SKIF-4 Supercomputer Platform: http://skif.pereslavl.ru/psi-info/rcms-skif/index.en.html

[127] SKIF-4 Architecture: http://skif.pereslavl.ru/psi-info/rcms-skif/skif-ppt.rus/2009/2009-04-01-pavt2009.ppt

[128] FusionIO ioDRIVE DUO Products: http://www.fusionio.com/products/iodriveduo/

[129] FusionIO ioXTREME Products: http://www.fusionio.com/products/ioxtreme/

[130] HP StorageWorks ESL E-series Products: http://h10010.www1.hp.com/wwpc/ru/ru/sm/WF25a/12169-304612-304631-304631-304631-392031.html

[131] Fujitsu Scalar 10K Series Modular Tape Libraries: http://ts.fujitsu.com/products/storage/tape/scalar/scalar_10k.html https://globalsp.ts.fujitsu.com/dmsp/docs/ds_scalar10k.pdf

[132] http://www.optolink.ru/ru/catalog/p5/

[133] http://www.optolink.ru/pdf/fiber_ru.pdf

[134] http://www.optolink.ru/pdf/RSF.pdf

[135] http://fotonexpress.ru/pdf/st/004-010.pdf

[136] http://fotonexpress.ru/pdf/st/011-019.pdf

[137] A. Zaytsev et al., "Building a High Performance Computing Infrastructure for Novosibirsk Scientific Center" (contribution presented at CHEP2010 conference: 18-22/10/2010, Taipei, Taiwan): http://indico2.twgrid.org/MaKaC/materialDisplay.py?contribId=29&sessionId=110&materialId=slides&confId=3

[138] Geant3 Network (GN3): http://www.geant.net

[139] WLCG Project: http://cern.ch/lcg

[140] Amazon Elastic Compute Cloud (EC2): http://amazon.com/ec2/

[141] https://www.scientificlinux.org

[142] http://www.xen.org

[143] http://www.linux-kvm.org

[144] http://www.lustre.org

[145] http://www.pvfs.org

[146] http://hadoop.apache.org

[147] gLite Middleware: http://cern.ch/glite

[148] APC NetBotz Sensors: http://www.apc.com/products/family/index.cfm?id=400

[149] "Optical Fibre based Distributed Sensor for Temperature Measurement" http://www.igcar.ernet.in/benchmark/Tech/19-tech.pdf

[150] F. Rodríguez-Barrios et al., "Distributed Brillouin Fiber Sensor Assisted by First-Order Raman Amplification": http://infoscience.epfl.ch/record/150155/files/JLT_28_2162_2010_1st

[151] L. Zou et al., "Distributed fiber Brillouin strain and temperature sensor with centimeter spatial resolution by coherent probe-pump technique": http://net04.isis.umanitoba.ca/activeshm/ReferencePage/Reference/Bao/spie5855_zou_a.pdf

[152] S. Kolos et al., "Online Remote Monitoring Facilities for the ATLAS Experiment" (contribution presented at CHEP2010 conference: 18-22/10/2010, Taipei, Taiwan): http://indico2.twgrid.org/MaKaC/materialDisplay.py?contribId=174&sessionId=51&materialId=slides&confId=3